On the role of alpha oscillations in structuring neural information processing

Eelke Spaak

The work described in this thesis was carried out at the Donders Institute for Brain, Cognition, and Behaviour, Radboud University Nijmegen, with financial support from the Netherlands Organization for Scientific Research (NWO VICI-grant 453-09-002) awarded to prof. dr. Ole Jensen.

ISBN/EAN 978-94-6284-019-5

Design & layout
Wouter Spaak (cover and chapter pages), Eelke Spaak (inside)

Print
Gildeprint, Enschede, The Netherlands.

On the role of alpha oscillations in structuring neural information processing

Proefschrift

ter verkrijging van de graad van doctor aan de Radboud Universiteit Nijmegen, op gezag van de rector magnificus prof. dr. Th.L.M. Engelen, volgens besluit van het college van decanen in het openbaar te verdedigen op donderdag 9 juli 2015 om 14:30 uur precies,

door

Eelke Spaak
geboren op 2 december 1985
te Nijmegen.

Promotor
Prof. dr. O. Jensen

Copromotor
Dr. F.P. de Lange

Manuscriptcommissie

Prof. dr. P. Fries

Prof. dr. C.M.A. Pennartz
Universiteit van Amsterdam

Dr. T.H. Donner
Universiteit van Amsterdam

To my parents

Contents

Chapter 1

Introduction

> Everyone knows what attention is. It is the taking possession by the mind, in clear and vivid form, of one out of what seem several simultaneously possible objects or trains of thought. Focalization, concentration, of consciousness are of its essence. It implies withdrawal from some things in order to deal effectively with others, and is a condition which has a real opposite in the confused, dazed, scatterbrained state which in French is called distraction, and Zerstreutheit in German.
>
> — William James (1890)

> More than a century of research behind us, and still most cognitive neuroscientists cannot venture beyond a vague William James quote when prompted to give a definition of attention.
>
> — Unattributed

1.1 Overview

In this introduction, I will first take the perspective of the philosophy of (cognitive) science, in order to provide some background to the empirical work presented in this thesis. Next, I indicate the main questions that have guided my research, and outline how the empirical chapters come together to answer these. The rationale for the specific experiments described in this thesis, and their methodological background, will be presented in each of the individual chapters themselves.

1.2 The (non-) reality of everyday cognitive concepts

In everyday life, human beings are remarkably adept at explaining, interpreting, and predicting other people's behaviour. For instance, consider observing someone whom you know to be thirsty, and who knows that there is a practically limitless supply of fresh water to be collected from the kitchen tap. If you then observe that person heading to the kitchen and pouring herself a glass of water, you will have no trouble whatsoever in explaining that behaviour. Indeed, you might well have predicted this course of events before it happened. Implicitly or explicitly, you have employed the concepts of belief ("that person believes there is water to be had from the tap, and that water quenches her thirst") and desire ("that person is thirsty, so desires a liquid refreshment") to understand another person’s behaviour. The constellation of ‘commonsense cognitive concepts’, or CCCs (an acronym following Francken & Slors, 2014), such as belief and desire, is often labelled folk psychology.

Folk psychology can be described as the intuitive, commonsense, pseudo-theoretical framework by which people attempt to make sense of the other human beings they share their everyday world with. Of course, folk psychological concepts can also be applied to oneself: why did I do X? Because I wanted Y and I believed that X would bring about Y. Why did I fail to finish my manuscript on time? Because my attention had a tendency to drift. The ubiquity of folk psychological concepts in the commonsense explanation of what goes in ‘inside the mind’ has led to a long-standing (and as yet unresolved) philosophical debate about the nature of those concepts. Are CCCs ‘real’ (and, if so, in what sense?) or are they simply ‘useful fictions’?[1]

With typically little interest in such metaphysical matters, cognitive neuroscientists in the twentieth century have attempted to empirically scrutinize the plethora of CCCs employed in folk psychology. Using carefully designed experiments, and recording diverse outcome measures such as reaction times, skin conductance, neural blood flow, scalp electrical potential, verbal reports, etc., cognitive neuroscience has produced papers on the “neural correlates of” nearly anything, ranging from “maternal and romantic love” (Bartels & Zeki, 2004) to the “behavioral preference for culturally familiar drinks” (McClure et al., 2004).

Although many neuroscientific studies purport to study the neural basis of some mental concept seemingly well-understood in everyday life, often a direct mapping between a CCC and a neural mechanism is not possible. Recently, it has convincingly been argued that the naïvely realistic appeal to CCCs in many neuroscientific studies forms an important obstacle to both the theoretical integration of the neuroscientific findings, and the communication of these findings with the general public (Francken & Slors, 2014). Although, for example, the concept of attention is very fruitful in the commonsense understanding of human beings, this does not necessarily entail that there is one mental or neural phenomenon corresponding to this concept. Similarly, neural mechanisms often found to correlate with attentional phenomena might be associated with other cognitive phenomena as well. In other words, the mapping from CCCs to neural

---

[1] The latter view can be traced back at least as far as Berkeley, who urged us to “think with the learned and speak with the vulgar” (Berkeley, 1710, §51).

circuitry is likely a many-to-many mapping.

1.3 Eliminative materialism in systems neuroscience

In the case of attention, the presence of this many-to-many mapping would explain why, to date, there has not yet been one scientifically agreed upon definition of attention (see the quotes at the beginning of this chapter): the concept itself, as well as the neural mechanisms associated with it, are simply too diverse to allow such a definition. Perhaps the neuroscientific study of attention would do best to embrace what in the philosophy of mind is known as eliminative materialism (Churchland, 1981): the concept of attention is useful in everyday practice, but its usefulness is exhausted when we want to explain the full richness of human cognitive behaviour. To achieve this latter goal, the concept of attention needs to be replaced with something more refined, presumably based on insights from cognitive neuroscience.

Eliminative materialism is not a commonly held theoretical position. Although it has been argued that cognitive neuroscience implicitly adheres to a realistic view of CCCs (Francken & Slors, 2014), I believe, in contrast, that the subfield of systems neuroscience typically (implicitly) embraces the eliminativist starting point. To illustrate this point, consider the case of the hippocampal theta rhythm (neural oscillations around 3-8 Hz).

In 1971, it was discovered that the rat hippocampal formation, a neural structure in the medial temporal lobe, contains cells that only fire when the animal is at specific places in a maze (the so-called place cells; O'Keefe & Dostrovsky, 1971). This seminal discovery led to many further studies and discoveries on the involvement of the hippocampus in spatial navigation, amongst which the now famous discovery of the neural 'code' underlying the representation of space, the grid cells (Hafting et al., 2005).[2] In 1993, it was discovered that the firing of hippocampal place cells is locked in a specific manner to the phase of the ongoing hippocampal theta rhythm, and that this phase locking was dependent on the spatial location of the animal (O'Keefe & Recce, 1993).

In a separate strand of investigation, it had long been known that the human hippocampus is crucial for the formation of new declarative memories,

---

[2] On October 6th, 2014, the Nobel prize in Physiology or Medicine was jointly awarded to John O'Keefe and May-Britt and Edvard Moser, for their discovery of the place and grid cells, respectively.

a discovery based mainly on the famous patient H.M., who had undergone a bilateral hippocampectomy in an attempt to control the epilepsy from which he suffered (Scoville & Milner, 1957). It was later found that the hippocampus plays a similar role in memory formation in rats and monkeys, too (Squire, 1992), and that the hippocampal theta rhythm is involved in this process (e.g. Tesche & Karhu, 2000b).

These two strands of evidence suggested that the hippocampus and its theta rhythm are crucially involved in two cognitive phenomena that everyday commonsense would hold to be separate: spatial navigation, and remembering facts. In recent years, various authors have attempted to integrate these findings. It has convincingly been argued (Eichenbaum & Cohen, 2014; Buzsáki & Moser, 2013) that both spatial navigation and the formation and retrieval of memories depend on the sequence-driven activation of particular cell assemblies, backed by the theta rhythm. I will not go into the details of this hypothesis, but will note here that the proposal is one of unification: two distinct CCCs (memory and navigation) are being linked to one underlying neural mechanism, which can be equated with neither. A hypothetical, ideal, scientific, understanding of behaviour and cognition will thus require an appeal to this underlying mechanism (either in neural or algorithmic terms), rather than to the CCCs, or any individual neural process underlying them, themselves. In this way, the example of the hippocampus and the computations it performs illustrates that, in systems neuroscience, "the principled displacement of folk psychology is not only richly possible, it represents one of the most intriguing theoretical displacements we can currently imagine" (Churchland, 1981).

1.4 Neuronal oscillatory dynamics underlying visuospatial attention

The work in this thesis (with the exception of Chapter 4) is only cursorily related to the hippocampal theta rhythm. The brief historical sketch given above only served as an illustration of the potential that systems neuroscience has for furthering our understanding of cognition, and for finally taking it firmly beyond the cognitive concepts that stem from commonsense. The rest of this thesis is primarily concerned with the neuronal oscillations involved in the direction and maintenance of visuospatial attention, in particular those oscillations in the alpha (7-13 Hz) frequency band. I will now outline some of the general findings in the literature concerning alpha activity.

Human subjects can be instructed to fixate the center of a screen, and direct their attention to either left or the right visual hemifield (without moving their eyes). Such a condition is known as the direction of covert spatial attention (as opposed to overt attention, which involves moving the eyes). It is well-established that neural oscillations in the alpha band (7-13 Hz) increase in power over the visual cortex ipsilateral to the locus of attention (i.e. left alpha power increases when attention is directed leftward, and vice versa), while alpha power decreases over the contralateral visual cortex (Worden et al., 2000; Kelly et al., 2006; Thut et al., 2006; Rihs et al., 2007). To interpret these findings, one needs to take into account the optic chiasm, i.e. the fact that visual information is processed in the contralateral hemisphere. The lateralization of alpha power with attention has led to the interpretation of alpha activity as reflecting the functional inhibition of brain regions irrelevant to the task at hand (Jensen & Mazaheri, 2010; Mathewson et al., 2011). It has been shown that the attentional modulations of alpha activity are not restricted to the visual system, but extend to the somatosensory (Haegens, Händel, & Jensen, 2011; van Ede et al., 2011) and auditory (Müller & Weisz, 2012) domain. Alpha activity and its hemispheric lateralization are correlated with behaviour (Thut et al., 2006; Händel et al., 2011): stronger alpha power means a better ability to suppress distracting information. This also holds when subjects are engaged in a working memory task: the higher the memory load, the stronger the alpha power (thus preventing interference from visual information) (Jensen et al., 2002).

Importantly, alpha activity is not a 'tonic' signal, it is, of course, an oscillation. This raises the question what role the phase of alpha might play, in addition to the modulation of alpha power. It has been found that the phase of alpha is adjusted to optimally protect working memory from distracting information (Bonnefond & Jensen, 2012), and that the detection of near-threshold stimuli depends on the phase of ongoing alpha (N. A. Busch et al., 2009; Mathewson et al., 2009). Furthermore, alpha phase has been shown to modulate spiking activity (Haegens, Nácher, et al., 2011) and the fMRI BOLD response (Scheeringa et al., 2011).

On the basis of these findings concerning alpha power and phase, it has been proposed that alpha activity serves as a temporal code in the visual system; a rhythmic modulation of neuronal gain, that prioritizes visual processing (Jensen et al., 2012, 2014). This prioritization might occur through an interaction of alpha with gamma activity. Gamma activity is high-frequency neuronal activity thought to reflect active cortical processing of information (Fries, 2009).

It is interesting to note the development in the theories concerning alpha activity here. The first studies relating alpha to visual information processing reported alpha modulation as a neural correlate of spatial attention, a commonsense cognitive concept. Now, many empirical studies and theoretical reflections later, alpha is thought to reflect a more general mechanism for organizing visual processing (or, indeed, neural processing in general), and is known to be involved in visual awareness and working memory maintenance, two CCCs only indirectly related to spatial attention in the commonsense vernacular.

1.5 Outline of this thesis

Before moving on to describing the empirical work presented in this thesis, first a more general point on the study of neuronal oscillations. In a similar vein to the point concerning systems neuroscience and its eliminativist perspective I made in section 1.3, more specifically, I believe that neuronal oscillations are ideally suited for bridging the gap between neural circuitry on the one hand, and cognitive phenomena on the other. Neural oscillations can be measured on a large scale, using electro- or magnetoencephalography (EEG/MEG), on a medium-large scale, using electrocorticography (ECoG), on a medium-small scale, using laminar or micro-electrode arrays, all the way to the very small scale, using single-cell or intracellular recordings and manipulations. This allows us to understand the same neural mechanism (e.g., alpha or gamma oscillations) from the viewpoint of the cognitive phenomena associated with it, its emergent brain-wide network, and the cellular or even molecular processes responsible for generating the rhythm.

In this thesis, I have attempted to build upon this highly fruitful middle ground that neural oscillations occupy. I worked from the hypothesis that alpha activity serves to organize and prioritize neural processing in the visual system, and have attempted to shed light on various aspects of this hypothesis. Specifically, I aimed to answer the following three questions: First, to what extent is the involvement of alpha oscillations in the structuring of visual perception causal, as opposed to merely correlational? Second, by what neuronal network mechanisms do alpha oscillations modulate the neural processing of visual information? And third, does the modulation of alpha activity constitute a general cognitive mechanism, or is it limited to a specific experimental setting?

In Chapter 2, I present results obtained using MEG in humans, that demonstrate that alpha activity can be externally induced (i.e., entrained). This entrainment follows a similar pattern to endogenous alpha oscillations, and the externally entrained alpha oscillations have consequences for visual perception. This demonstrates that alpha activity is causally involved in processing visual information, and not an epiphenomenon.

In Chapter 3, I shift my perspective to a much smaller spatial scale. I analyzed data obtained using a laminar electrode in the monkey primary visual cortex, which allowed me to characterize neural processing across the different layers of a single cortical column. I show that one way in which alpha might modulate processing in visual regions is through an interaction with the cortical gamma rhythm. This interaction is present on both a slow timescale (amplitude correlation) and a much faster one (phase-amplitude coupling).

Moving on to Chapter 4, I take a slight detour from alpha activity in the visual system. Having shown in Chapter 3 that phase-amplitude coupling between alpha and gamma activity is present within the cortical microcircuit, I next asked what cellular network mechanisms might be responsible for such a coupling. To answer this question, I studied a neural phenomenon for which we know much more about the underlying physiology than about alpha/gamma coupling, namely the coupling between the hippocampal theta rhythm and gamma activity. For this phenomenon, I derived a computational biophysical model, and show that fast-spiking interneurons are likely responsible for the observed cross-frequency interaction. This finding generalizes to frequency bands other than theta, and thus is likely applicable to neocortical alpha/gamma coupling as well.

In the final two empirical chapters, I return to human MEG and demonstrate that spatially specific alpha modulation is not limited to explicitly cued covert spatial attention, but is also present in more ecologically valid conditions. In Chapter 5, I present results concerning human subjects engaged in a repeated visual search task. I show that the modulation of visual alpha activity is one of the mechanisms by which the brain prepares itself for upcoming stimuli in such a task. Finally, in Chapter 6, I show that spatially specific alpha activity is associated with the saccadic eye movements that occur during free visual exploration of natural scenes. Thus, modulation of alpha activity structures information processing in everyday cognition as well.

Chapter 2

Local entrainment of alpha oscillations by visual stimuli causes cyclic modulation of perception

2.1 Abstract

Prestimulus oscillatory neural activity in the visual cortex has large consequences for perception, and can be influenced by top-down control from higher-order brain regions. Making a causal claim about the mechanistic role of oscillatory activity requires that oscillations are directly manipulated independently of cognitive instructions. There are indications that a direct manipulation, or entrainment, of visual alpha activity is possible through visual stimulation. However, three important questions remain: (1) can the entrained alpha activity be endogenously maintained, in the absence of continuous stimulation; (2) does entrainment of alpha activity reflect a global or a local process; and (3) does the entrained alpha activity influence perception? To address these questions, we presented human subjects with rhythmic stimuli in one visual hemifield, and arhythmic stimuli in the other. After rhythmic entrainment, we found a periodic pattern in detection performance of near-threshold targets specific to the entrained hemifield. Using magnetoencephalograhy (MEG) to measure ongoing brain activity, we observed strong alpha activity contralateral to the rhythmic stimulation outlasting the stimulation by several cycles. This entrained alpha activity was produced locally in early visual cortex, as revealed by source analysis. Importantly, stronger alpha entrainment predicted a stronger phasic modulation of detection performance in the entrained hemifield. These findings argue for a cortically focal entrainment of ongoing alpha oscillations by visual stimulation, with concomitant consequences for perception. Our results support the notion that oscillatory brain activity in the alpha band provides a causal mechanism for the temporal organization of visual perception.[1]

---

[1] The work in this chapter was previously published as Spaak., E., De Lange, F.P., & Jensen, O. (2014). Local entrainment of alpha oscillations by visual stimuli causes cyclic modulation of perception. The Journal of Neuroscience. 34(10), 3536–3544, doi:10.1523/jneurosci.4385-13.2014

2.2 Introduction

It has been well-established that prestimulus neural activity correlates with visual perception. In particular, both the power and the phase of prestimulus occipital alpha oscillations (8-12 Hz) can determine whether or not a near-threshold target is detected or not (Hanslmayr et al., 2007; van Dijk et al., 2008; N. A. Busch et al., 2009; Mathewson et al., 2009; Thut et al., 2012). These oscillatory processes are likely under top-down control from higher-order brain regions (Capotosto et al., 2009, 2012). Typically when an effect of oscillatory activity on perception is shown, the analysis is correlative. However, it is desirable to go beyond such correlative analyses, and ask: is there a causal relationship between oscillatory neural activity and perception?

One potentially fruitful avenue of research is the manipulation of endogenous oscillations by external stimuli by entrainment. For instance, transcranial magnetic stimulation (TMS) at alpha frequencies has been shown to affect oscillatory activity as measured by electro-encephalography (EEG) (Thut et al., 2011) and perceptual performance (Romei et al., 2010). The entrainment of endogenous oscillations by visual stimulation has also been investigated. It has been shown that the human visual cortex shows the strongest resonance to 10 Hz visual flicker (Herrmann, 2001). Furthermore, a perceptual after-effect in the form of a rhythmic modulation of hit rate after 10 Hz visual stimulation has been reported (de Graaf et al., 2013), as well as phase-locking of neural oscillatory activity during such stimulation (Mathewson et al., 2012). Finally, although there are indications in the literature that neural activity following rhythmic stimulation is similar to neural activity observed during stimulation (Halbleib et al., 2012), persistent post-stimulus entrainment effects in terms of increased phase-locking or power modulation has not yet been demonstrated.

Summarizing, three important open questions remain concerning the entrainment of endogenous alpha oscillations using visual stimulation. First, can the entrained alpha activity be endogenously maintained, in the absence of continuous stimulation? Second, does entrainment of alpha activity reflect a global or a local process? And third, does the entrained alpha activity influence perception? The present study addresses these three questions, using a paradigm involving bilateral visual flicker stimulation and difficult-to-detect visual targets, and continuous recording of neural activity using magnetoencephalography (MEG), enabling us to investigate the effect of visual flicker on both behavioral performance and brain oscillations simultaneously.

2.3 Methods

2.3.1 Participants

22 subjects (7 female; age range 18-51) with no history of neurological or psychiatric disorders (based on self-report) participated in this experiment. All subjects gave written informed consent according to the Declaration of Helsinki. The study was approved by the local ethics committee (CMO region Arnhem-/Nijmegen). Data for two subjects had to be excluded because of excessive eye movements, and a further subject was excluded because detection performance was at chance level. This leaves a total of 19 subjects on which all analyses are based.

2.3.2 Experimental design

During the entire experiment a fixation cross was presented against a gray background. During the inter-trial interval (1.5 s), the fixation cross was dimmed, indicating to the participant that blinking or making saccades was allowed. At the beginning of each trial, a bright fixation cross was presented for 1 s, instructing the participant to refrain from blinking or making saccades. After this baseline interval, a 1.5 s train of visual flashes were presented (Figure 2.1) in the form of white squares. Each flash lasted 17 ms (one frame refresh of our projector), the sides of each square measured 6 °(visual degrees), and the squares were placed at 3 °excentricity. At each trial, either the left or the right visual field was presented with a 10 Hz periodic stimulus train (inter-flash interval 83 ms, total number of flashes per hemifield per trial = 16) while the other hemifield was presented with a jittered stimulus train. The timings of the jittered stimulus train was generated randomly, subject to the constraint that no two flashes could occur in subsequent frame refreshes (i.e., there always was at least one blank frame between two flashes). The number of flashes in both hemifields was kept the same, as was the timing of the first and last flashes. This controls for possible non-entrainment-specific effects of the final entrainment flash, such as forward visual masking or a transient evoked response in the MEG data. After a variable delay of 17 to 340 ms (in steps of 17 ms, uniform probability across different possible delays), a circular aperture near-threshold sine-wave grating target (duration 17 ms, diameter 1 °) was presented in either of the two hemifields at the location of the flashing stimulus trains. The subjects' task was to identify,

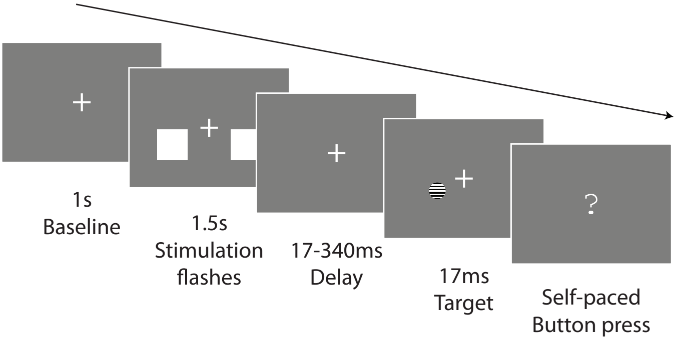

Figure 2.1: Experimental design. Subjects were presented with 1.5 s stimulation trains composed of bilateral flashing white squares against a dark gray background. One of the squares flashed periodically at 10 Hz, the other had a jittered inter-flash interval. The hemifield of random versus jittered stimuli was randomized over trials. After the offset of the stimulus trains, a near-threshold target appeared in either of the two hemifields after a brief random delay. Subjects were instructed to indicate whether they saw the target left or right (forced-choice).

by a right-hand index or middle finger button press, in which hemifield they detected this target (forced choice). After the left/right response, subjects had to indicate whether they were sure or unsure about their response. We do not report any results related to the confidence rating here, as this rating did not correlate with the alpha entrainment phenomenon under investigation.

Each experimental session started with 40 practice trials with easy to detect targets, to make the subject acquainted with the task. Next followed 60 trials in which we estimated the subjects' perceptual threshold in order to achieve an overall performance of 80% correct. To this end we used the Bayesian QUEST procedure (Watson & Pelli, 1983) to adjust the contrast of the target such that the desired performance level was achieved. Next followed four blocks of 90 trials each. All analyses are based on the trials from these 4 blocks. The target grating contrast was kept constant throughout each block, but was updated between blocks (by updating the QUEST distribution estimated after each trial) in order to accommodate effects of fatigue, habituation, or sensitization; keeping the subjects' performance at the desired 80%.

2.3.3 Experimental equipment

Stimuli were presented by back-projection onto a semi-translucent screen by an EIKI LC-XL100L projector. The projection measured 46 cm in width, and had a resolution of 1024x768 pixels. Subjects were seated in a magnetically shielded room, at 80 cm distance from the projection screen. Throughout the experiment, the magnetoencephalogram (MEG) was recorded at a sampling rate of 1.2 kHz using a 275-channel axial gradiometer CTF MEG system. In addition, we continually recorded subjects' gaze position using an SR Research Eyelink 1 000 eye tracking device. Whenever the fixation cross was white, subjects could not blink or saccade further than 1.7 °from the fixation center. If they failed to maintain fixation, the trial was aborted and subjects were informed of their eye movement by a bright red cross on the screen. After the MEG experimental session, structural magnetic resonance imaging (MRI) images were obtained from all subjects using a 1.5 T Siemens Magnetom Avanto system.

2.3.4 Behavioral analysis

Statistical significance of the sinusoidal fit to the hit rate data (Figure 2.2B) was assessed by using a Wald test (Fox, 1997). This test controls for the increase in degrees of freedom of the complex model (line plus sinusoid) when compared to the simpler model (line only). In addition, we performed a permutation test: the amplitude of the sinusoidal fit to the observed hit rate data was compared to the amplitudes of sinusoidal fits to randomized data. Randomized data was generated by randomly permuting the hit rate time course 1 000 times. Finally, to rule out that the periodicity was driven by a single subject, we performed a bootstrap procedure: we sampled randomly, with replacement, from our subjects, 5 000 times to obtain a 95% confidence interval on the circular-to-linear correlation between delay and hit rate.

To quantify the rhythmic entrainment effect observed in the hit rate profile in a single quantity, we defined an 'entrainment index (EI)'. Trials could have the target either in-phase or anti-phase with the entraining stimuli. Also, the targets could be either ipsilateral (entrained, E) or contralateral (non-entrained, NE) to the rhythmic stimuli. The ratio between hit rate (HR) for anti- and in-phase entrained trials was defined as the variable of interest. We normalized this variable by the corresponding ratio in the non-entrained trials, to account for the non-phase-specific hit rate increase with delay. This yielded the following expression for the entrainment index:

The EI thereby reflects the amount to which the rhythmic stimulus train caused a rhythmic effect in the hit rate.

2.3.5 MEG data preprocessing

All MEG data were analyzed using MATLAB R2012a, either using custom-written scripts or using the FieldTrip toolbox (Oostenveld et al., 2011). As judged by visual inspection, excessively noisy sensors were removed from the data (on average 0.8 sensors were removed per session), as were trials containing strong muscle or movement artifacts (on average 5.8 trials were removed per session). All trials were demeaned and a linear trend was fitted and removed. Data was downsampled to 300 Hz to speed up processing. An independent component analysis was performed, in order to identify and remove activity caused by cardiac activity. For each session, 2 components reflecting the QRS complex were removed, and the decomposed data was backprojected to sensor space.

We computed an approximation of the MEG planar gradient, using FieldTrip's ft_megplanar function. Considering planar, rather than axial, gradient data facilitates the interpretation of MEG results, as planar gradient maxima are located above neural sources (Hari & Salmelin, 1997; Bastiaansen & Knsche, 2000). For the event-related fields, we combined the resulting horizontal and vertical planar gradients by singular-value decomposition per channel, projecting the data along the strongest direction. For the spectral analyses, we computed metrics separately for the horizontal and vertical planar gradients, and combined the two by computing the sum.

Before the event-related averaging (Figure 2.4), the data was band-pass filtered in the range of 2 to 30 Hz using a finite impulse response filter. The filter order was set to three cycles of the lower bound of the passband.

Whenever plots and results of sensor-space analyses refer to a particular selection of sensors (left/right, ipsi-/contralateral) we always refer to the posterior sensors overlying the left and right hemispheres, as defined by the CTF MEG manufacturer.

2.3.6 Spectral analysis

To get a time-frequency representation (TFR) of power and inter-trial coherence (ITC), we used a sliding time window fast Fourier transform (FFT) approach.

Frequencies of interest ranged from 2 to 30 Hz in steps of 1 Hz. The time window was always such that it fit exactly 4 cycles of the frequency of interest, and it slid over the time axis in steps of 50 ms. Each instance of the sliding time window was multiplied by a Hanning taper and Fourier-transformed, thus yielding a time-resolved complex Fourier spectrum. Power values $\text{pow}_n(f,t)$ for trial n, frequency f, and time point t were computed by squaring the absolute value of the Fourier coefficients $c_n(f,t)$, i.e. $\text{pow}_n(f,t) = |c_n(f,t)|^2$, and were averaged over trials. Inter-trial coherence was defined as the absolute value of the complex mean of the Fourier values, after normalizing them by unit length:

$$\text{ITC}(f,t) = \left| \frac{1}{N} \sum_{n=1}^{N} \frac{c_n(f,t)}{|c_n(f,t)|} \right|$$

2.3.7 Source analysis

To obtain an estimate of the sources of the observed 10 Hz activity, we applied a beamforming spatial filtering technique known as dynamic imaging of coherent sources (DICS) (Gross et al., 2001) to our 10 Hz power data. This step used the data recorded from the axial gradiometers. The DICS algorithm computes a spatial filter from the cross-spectral density matrix (CSD) of the data and a lead field matrix. To compute the CSD, we used a multitaper FFT approach. Data was subselected between 0.9 and 1.5 s after entrainment stimuli onset, separately for data with entrainment in the right and left hemifield. Slepian tapers were applied to obtain a ± 2 Hz spectral smoothing, thus yielding an estimate of activity in the 8-12 Hz band. The CSD was estimated using the combined data of the left- and right-entrained trials. To obtain the lead fields for each subject, we constructed a realistically shaped single-shell head model based on the individual anatomical MRI (Nolte, 2003), after spatially co-registering the MRI to sensor space MEG data by identifying fiducials in the nasion and the two ears. Each brain volume was divided into a grid of points spaced 8 mm apart, and warped to the template Montreal Neurological Institute (MNI) brain. The lead field was calculated for each grid point (Nolte, 2003). The estimated power in source space was averaged over trials. For visualization purposes, the grand-average grid was interpolated onto the single-subject MNI template brain (Figure 2.6).

The above approach yielded an estimate for the neural sources responsible for the alpha band power increase during the entraining stimuli. To get an estimate of the post-entrainment active neural sources (Figure 2.6B), we applied the filter computed based on the 0.9-1.5 s time window to the CSD estimated during the time window 1.5 to 2 s, i.e. after the entraining stimuli offset.

2.3.8 Cluster-based permutation statistics

To statistically quantify the time-frequency results of power and ITC, and the source analysis results, we performed cluster-based permutation tests (Maris & Oostenveld, 2007) across subjects. Specifically, for each voxel (either time/frequency/channel voxels for sensor space TFR analyses or x/y/z voxels for source space analysis) we computed the normalized difference between conditions; diff $= \frac{A-B}{A+B}$. This metric was computed both for the observed data and for 1 000 (in the case of sensor space analysis) or 1 500 (in the case of source space analysis) permutations of the conditions. Based on the per-voxel permutation distribution of descriptives thus obtained, we thresholded the observed values with the 95th percentile of this distribution to obtain cluster candidates. For each permutation, the cluster candidate with the highest sum of voxel-level descriptives was added to the permutation distribution of cluster statistics. The sum of descriptives for each observed cluster candidate was compared to this permutation distribution to assess significance for each cluster. For the source-level analysis, we used the maximum value of voxel-level descriptives per cluster (rather than the sum of all descriptives) as the cluster statistic to test, since spatial extent of clusters in beamforming typically is not closely related to the reliability of the source reconstruction (i.e., beamforming tries to make sources as small as possible; in the ideal case neighbouring voxels are independent). For the sensor-level analysis, using the sum of descriptives makes more sense, as cluster extent is informative as to the reliability of the finding (i.e., neighbouring time/frequency/channel points are likely highly correlated).

2.4 Results

Subjects were presented with trains of 16 flashes that were temporally spaced over a 1.5 s period against a gray background (Figure 2.1). Each flash lasted 17 ms. Either the left or the right visual field was stimulated by 10 Hz periodic flashing, while the other hemifield was stimulated by a jittered flash train. After a variable delay (17-340 ms), a near-threshold target (duration 17 ms) was presented in one of the two hemifields. The subjects' task was to detect in which hemifield the target was presented (two-alternative forced choice).

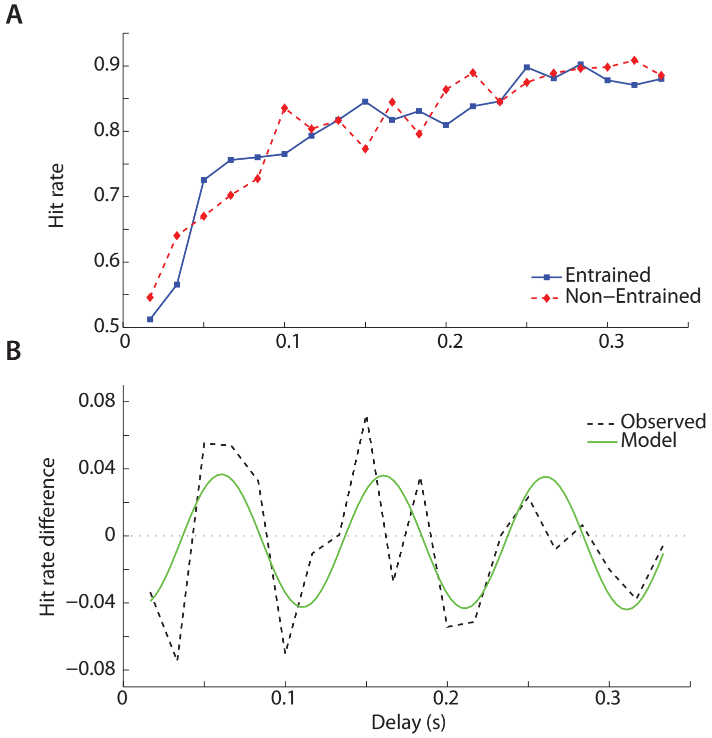

Figure 2.2: Behavioral results. **(A)** Hit rate as a function of the delay between entrainment stimuli and target. A clear improvement in performance was observed with increasing delay, both for the entrained and non-entrained trials. **(B)** The difference in hit rate between entrained and non-entrained trials, as a function of delay. Dashes lines indicate grand average observed values, the green curve indicates the best fit 10 Hz sinusoid.

2.4.1 Rhythmic visual stimulation results in hemifield-specific periodic modulation of perception

The target stimulus could appear either at the side of the periodic stimulation (an 'entrained' trial), or at side of the arhythmic stimulation (a 'non-entrained' trial). Our main question was whether the delay between the last flash of the stimulation train and the target modulated perception rhythmically. First, we observed similar hit rates and reaction times for the entrained (E) and non-entrained (NE) trials across subjects ($HR_E = 80.5 \pm 1.0\%$; $HR_{NE} = 80.0 \pm 0.9\%$

(mean ± SEM); paired-samples $t_{18} = 0.54, p = 0.60$; $\mathrm{R}_E = 362 \pm 55ms$; $\mathrm{RT}_{NE} = 356 \pm 55ms$; $t_{18} = 0.96, p = 0.35$), indicating that there was no difference in attention to an entrained versus a non-entrained hemifield. Hit rate strongly increased with longer delays (Figure 2.2a), both for the entrained and non-entrained trials ($r_E = 0.84, r_{NE} = 0.89$, both $p < 10^{-5}$). This is expected because of the forward masking effect of the stimulus trains.

The hit rate difference between entrained trials and non-entrained trials revealed a clearly periodic pattern (Figure 2.2b), indicating that the periodic stimulation resulted in a rhythmic modulation of detection performance matching the stimulation in frequency. We tested this periodicity by fitting a 10 Hz-sinusoid to the hit rate data (Figure 2.2b, green curve). The sinusoid plus a linear trend fitted the data significantly better than a linear trend only. This was assessed using a Wald F-test ($F_{2,15} = 6.73, p = 0.008$), which controls for the increase in degrees of freedom. To alleviate possible concerns regarding a bias of the Wald test, we verified this observation by performing a permutation test, obtaining similar results ($p = 0.01$). Finally, to rule out that this result was driven by a small amount of subjects, we performed a bootstrap procedure, obtaining a 95% confidence interval on the circular-to-linear correlation between delay (expressed as 10 Hz phase) and hit rate of $r = 0.46 - 0.91$, thus confirming a robust periodicity in the hit rate profile. Interestingly, we observed this periodicity after the offset of the rhythmic stimulation, indicating that the rhythmicity is maintained by an endogenous mechanism. Also note that the hit rate profile went both above and below the zero-line (Figure 2.2b). This means that perception was impaired at certain phases relative to the entraining stimuli, while it is enhanced at others.

Since the above analysis was based on the difference between the entrained and non-entrained trials, we cannot yet be certain that the periodicity in hit rate is exclusively explained by the rhythmic entrainment. To address this issue, we conducted a 2 × 2 repeated-measures analysis of variance, with entrained vs. non-entrained and in-phase vs. anti-phase as factors (Figure 2.3). In-phase trials are here defined as those trials in which the target appeared precisely 100 or 200 ms after the entrainment; while anti-phase trials are those with a delay of 150 or 250 ms. We found a significant interaction between entrainment and phase ($F_{1,18} = 6.28, p = 0.02$). Post-hoc t-tests revealed that there was a significant difference between in- and anti-phase hit rate for the entrained trials ($t_{18} = 2.75, p = 0.01$), but this difference was not significantly present for the non-entrained trials ($t_{18} = 0.65, p = 0.53$). These results demonstrate that the periodic modulation of detection performance is present only in the visual

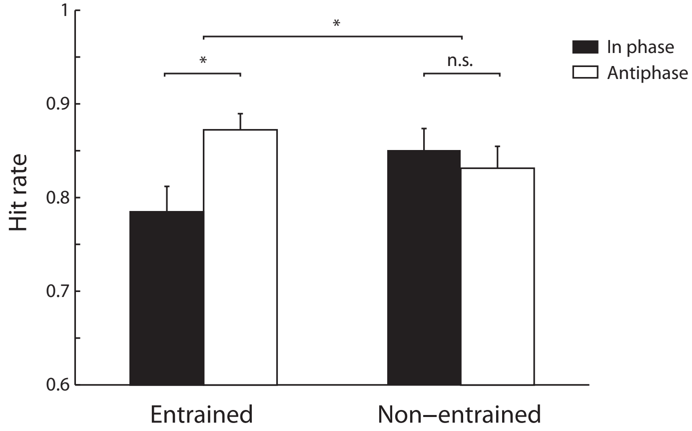

Figure 2.3: Hit rates computed for only in-phase (100, 200 ms) or anti-phase (150, 250 ms) delays, separately for the entrained and non-entrained trials. Repeated-measures ANOVA revealed a significant interaction between the two factors, and post-hoc t-tests reveal that there is an effect of delay (i.e. phase) only when the target was presented at the entrained hemifield. Error bars reflect unbiased within-subjects corrected SEM (Cousineau, 2005; Morey, 2008). * indicates $p < 0.05$.

hemifield that received rhythmic visual stimulation.

2.4.2 Rhythmic visual stimulation causes persistent alpha activity in early visual cortex

We next asked if the rhythmic stimulation entrained the alpha activity as detected in the MEG signal. We first report the event-related fields (ERFs) time-locked to the onset of the stimulation trains (Figure 2.4). All ERFs are presented as planar gradient (two planar gradient orientations were combined using a singular-value decomposition approach, which preserves phase information). The periodic stimulus trains were accompanied by clear rhythmic temporal dynamics in the ERFs (Figure 2.4). As expected, the ERFs with the highest amplitude occurred in the sensors contralateral to the rhythmic stimulation (occipital/posterior channels, as defined by the CTF MEG manufacturer; mean rectified ERF between 1.55 and 2 s, contralateral vs. ipsilateral sensors: $t_{18} = 3.39, p = 0.003$). Some rhythmic activity was also observed contralateral to the jittered stimulation

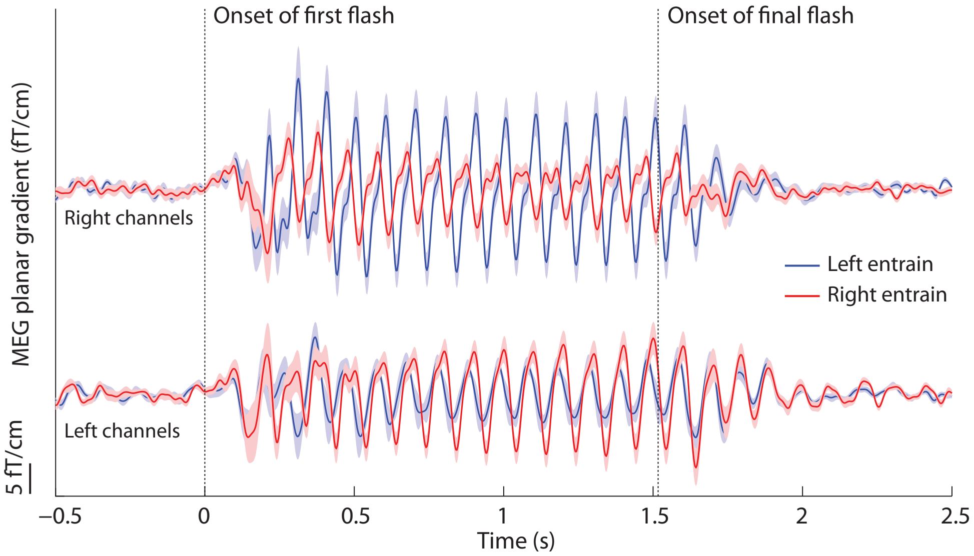

FIGURE 2.4: Event-related fields (ERFs) during rhythmic stimulation. The MEG planar gradient shown separately for the sensors overlying the left (bottom) and right (top) occipito-posterior hemispheres (as defined by the CTF MEG manufacturer). Red and blue curves correspond to rhythmic stimulation in the right and left visual fields, respectively. A periodic pattern is clearly visible as a consequence of the stimulation. Amplitude was higher over the contralateral sensors. Importantly, the rhythmicity in the ERFs persisted for several cycles after the end of the rhythmic stimulation (second vertical dotted line). The MEG planar gradient in the direction of most power was used, as computed by singular value decomposition. Error bounds reflect unbiased within-subjects corrected SEM (Cousineau, 2005; Morey, 2008).

trains. This effect is best explained by field spread from the other hemisphere (see (Lütkenhöner, 2003)). Importantly, we found that the phase-locked rhythmic brain activity persisted after the offset of the rhythmic visual stimulation (Figure 2.4, second vertical dotted line). These results do not change qualitatively when we compute the ERF only for trials where the target appeared ≥ 200 ms after the rhythmic stimuli offset (not shown). We therefore conclude that the effects are not driven by target processing in the post-stimulation interval. Statistical assessment of the phase-locking evident in the ERFs is more straightforward when based on the time-frequency representation of inter-trial coherence; this is described below.

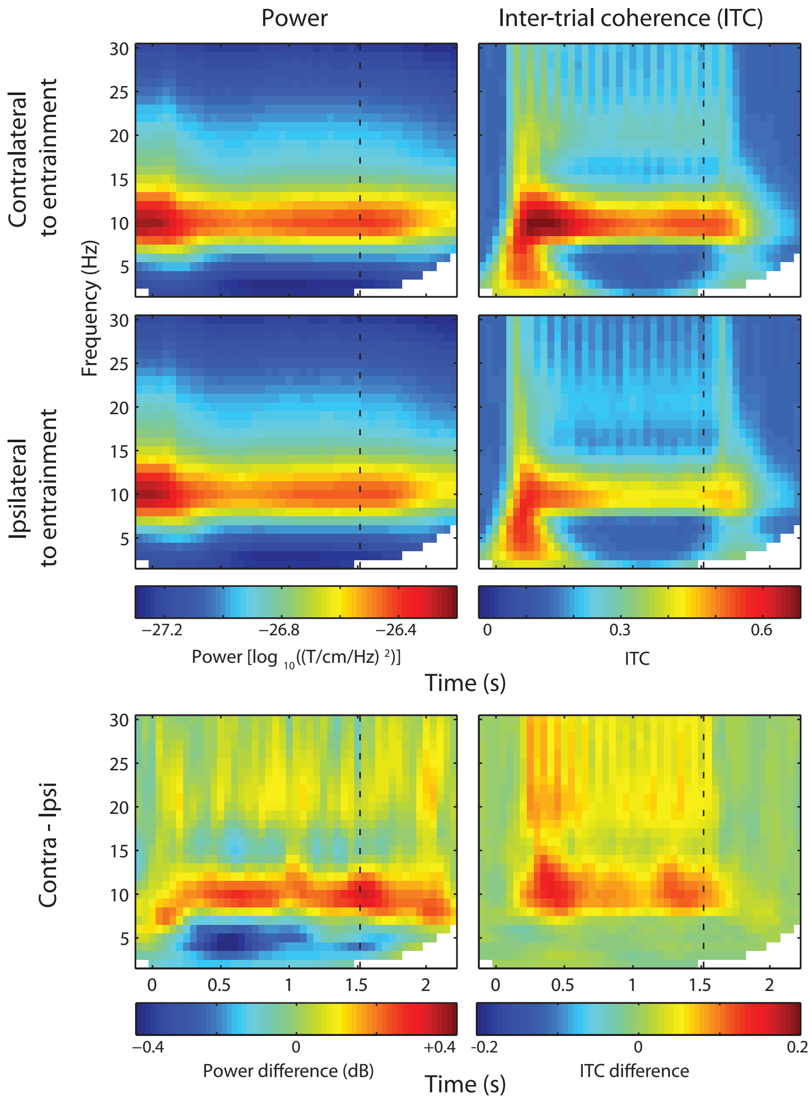

Figure 2.5: Frequency-domain analysis results. Time-frequency representations of power (left) and inter-trial coherence (ITC; right), shown for sensors contralateral (top) and ipsilateral (middle) to the rhythmic stimulation. The bottom plots show the difference between contra- and ipsilateral sensors. A persistent alpha power and ITC increase was visible for contralateral sensors, which outlasted the rhythmic stimulation.

Next we identified the effects of the rhythmic stimulation in the frequency domain. The time-frequency representations of power averaged over trials showed a clear effect in the alpha band (Figure 2.5). Considering the power difference between sensors contra- and ipsilateral to the entrained hemifield, we found that the alpha activity was strongest in the contralateral sensors (cluster-based permutation test (Maris & Oostenveld, 2007), $p = 0.004$), confirming the entrainment of alpha activity. We also found a clear reduction in low-frequency activity in the contralateral sensors (cluster-based permutation test, $p = 0.001$). The 10 Hz power in ipsilateral sensors is best explained by magnetic field spread of activity from the other hemisphere (as confirmed by source analysis below, also see (Lütkenhöner, 2003)). A similar pattern was observed when considering the inter-trial coherence (ITC; Figure 2.5, right panel): alpha band ITC is significantly higher for the contralateral sensors ($p = 0.001$). From Figure 2.5 (bottom left panel) it seems clear that the entrained activity persists after the stimulus train. To exclude effects from the temporal smoothing introduced by the spectral analysis, we also computed the alpha power and ITC for the MEG in the post-entrainment interval only (1.5-2 s). We found a significantly greater 10 Hz power ($t_{18} = 3.32, p = 0.004$) and ITC ($t_{18} = 5.01, p = 9.1 \cdot 10^{-5}$) post-entrainment for the sensors contralateral to the entrainment hemifield than for the ipsilateral sensors. Similar results are obtained when we test alpha power and ITC in a narrow time window starting 200 ms after the stimulation (1.7-1.8 s; power: $t_{18} = 2.06, p = 0.054$; ITC: $t_{18} = 2.88, p = 0.01$). Finally, we also calculated ITC from Hilbert-transformed, bandpass filtered data. This analysis confirmed a sustained elevation of ITC after the stimulus train. The ITC increase was sustained for approximately 200 ms longer in the hemisphere contralateral to the entraining stimuli than in the ipsilateral hemisphere (data not shown). We conclude that the rhythmic stimulation resulted in increased endogenous phase-locked alpha activity persisting after the stimulation.

To identify the neural sources corresponding to the alpha entrainment, we performed a beamformer analysis (dynamic imaging of coherent sources, DICS (Gross et al., 2001)) on the MEG data at 10 Hz in the interval 0.9 to 1.5 s. Figure 2.6a shows the contrast between left and right entrainment in the left panel, and the reverse contrast in the right panel. We show only the significant clusters ($p < 0.05$) arising from a cluster-based permutation test (Maris & Oostenveld, 2007), controlling for multiple comparisons. For both the left and the right entrainment, there were clear peaks in the occipital cortices contralateral to the entrained hemifield, around the calcarine sulci. When we apply the spatial

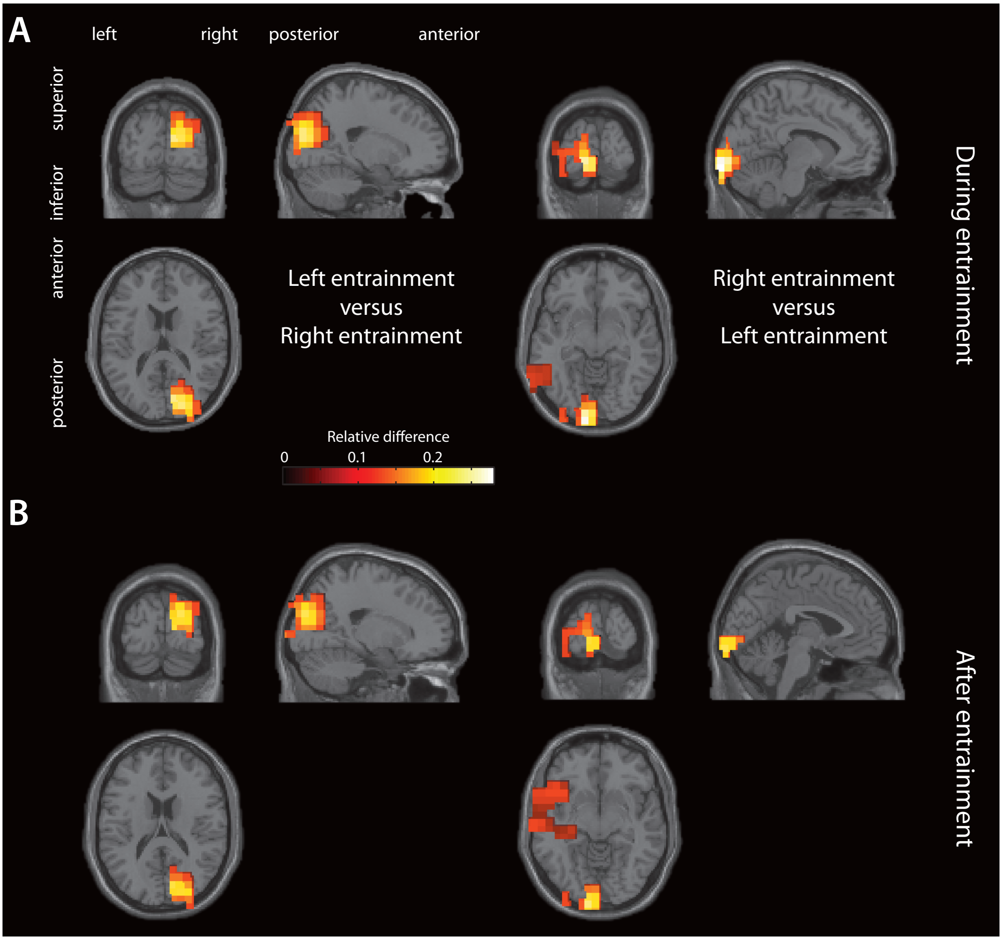

Figure 2.6: Source analysis results. **(A)** Grand-average results for dynamic imaging of coherent sources (DICS) beamformer source analysis of entrained 10 Hz activity during stimulation, interpolated onto a single-subject MNI template brain. Values are masked with cluster-based permutation test $p < 0.05$, controlling for multiple comparisons. The left and right panels show the sources for the 10 Hz activity during left and right rhythmic stimulation, respectively. **(B)** Same, but with activity estimated during the post-entrainment window.

filter computed during the stimulation to the activity in the time window after stimulation, 1.5-2 s, the same neural sources are significantly activated (Figure 2.6B; masked with cluster-permutation $p < 0.05$). These results indicate that early visual regions are responsible for the alpha power increase observed both during and after the rhythmic 10 Hz stimulation.

2.4.3 Periodic modulation of perception is mediated by entrained alpha activity

We next asked if variability in alpha entrainment over trials as observed in the recorded MEG signal predicted the periodicity found in the detection performance. We quantify this periodicity by an 'entrainment index (EI)', which reflects the amount to which the rhythmic stimulus train caused a rhythmic effect in the hit rate (see Methods for details). We separated the trials for each subject into four bins corresponding to quartiles of alpha power during the periodic stimulus trains, and computed the EI separately for trials belonging to each of those bins (Figure 2.7). The alpha power used to sort the trials was estimated either from the sensors contralateral to the entrainment stimuli (where, as shown, the strongest alpha effect was observed), or from the ipsilateral sensors. We found a significant interaction between the alpha-providing hemisphere and alpha quartile ($F_{3,18} = 2.86, p = 0.045$). Subsequent t-tests revealed that higher alpha quartiles corresponded to a higher EI, but only when alpha power was estimated from the sensors contralateral to rhythmic stimulation (Q4 vs. Q1: $t_{18} = 2.29, p = 0.03$). This was not the case when alpha power was estimated from the sensors ipsilateral to rhythmic stimulation (Q4 vs. Q1: $t_{18} = 0.71, p = 0.49$). We conclude that higher locally entrained alpha power predicts a stronger phasic effect in detection performance.

To rule out that this correlation between perceptual rhythmicity and alpha power entrainment is trivially explained by effects of vigilance (which could be reflected in a general alpha power increase or decrease), we also computed the ITC separately for the different alpha power quartiles. We find a significant effect of alpha power quartile on ITC ($F_{3,18} = 7.22, p = 4 \cdot 10^{-4}$), with higher alpha power quartiles corresponding to higher ITC (Q4 vs. Q1: $t_{18} = 3.11, p = 0.006$). We can therefore conclude that the rhythmic modulation of hit rate is due to entrainment of endogenous oscillations in the alpha band.

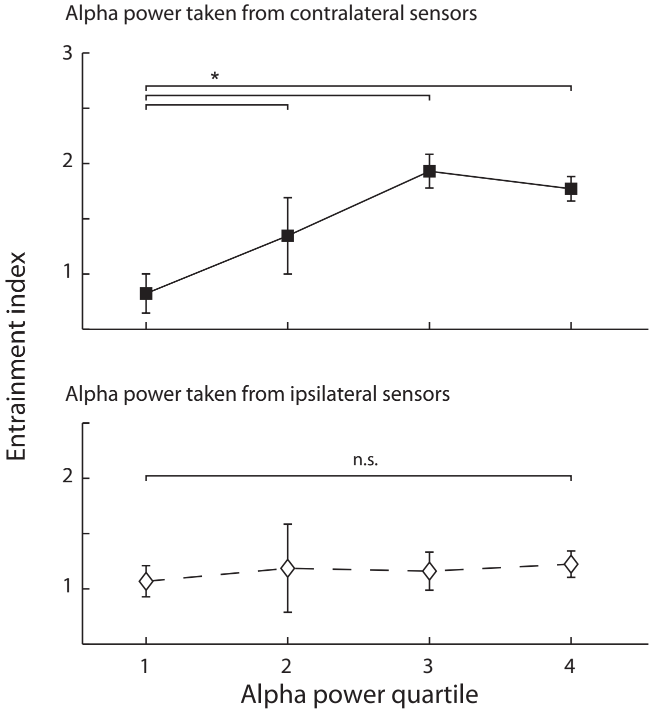

Figure 2.7: Relation between entrained alpha activity and perception. The 'phasic entrainment effect', i.e. the amount to which the rhythmic stimuli resulted in a rhythmic hit rate modulation, shown separately for four quartiles of alpha power. Alpha power was estimated either from the sensors ipsi- (bottom) or contralateral (top) to the rhythmic stimulation. Importantly, the hit rate was strongly phasically modulated for trials during which contralateral entrained alpha power was high, but not for trials with low power. No such effect was observed for the ipsilateral alpha. Error bars reflect unbiased within-subjects corrected SEM (Cousineau, 2005; Morey, 2008). * indicates $p < 0.05$.

2.5 Discussion

We have demonstrated that 10 Hz rhythmic visual stimulation induces alpha-band rhythmicity in ongoing neuronal activity. The entrained rhythm was intrinsic to the brain, since it outlasted the stimulation train by several cycles. Furthermore, the stimulation caused a subsequent rhythmicity in subjects' perceptual ability. Importantly, the degree of rhythmic entrainment of the MEG signal predicted the rhythmicity in perceptual performance. The rhythmic modulation of both the brain activity and the detection performance was limited to the hemisphere contralateral to the stimulated hemifield, suggesting local neuronal entrainment. This was confirmed by source localization demonstrating the involvement of early visual cortical areas.

Previous work has convincingly demonstrated that trains of TMS pulses and visual stimuli can entrain brain activity detected in the EEG (Thut et al., 2012). It has been shown that 10 Hz visual stimulation results in the strongest neural entrainment compared to other frequency bands (Herrmann, 2001). Furthermore it has been shown that 10 Hz entrainment can produce a cyclic modulation of perceptual performance; however, the brain dynamics underlying this phenomenon are still unclear (Mathewson et al., 2012; de Graaf et al., 2013). We now directly link the measured entrainment to behavior: the entrained brain activity is correlated over trials with the rhythmicity in the periodic hit rate profile. Another important insight from our findings is that the entrainment is local; i.e. it reflects the rhythmic engagement of spatially specific visual regions rather than a more global signal. This claim is based on the fact that the effect on target perception was only seen in the rhythmically stimulated hemifield. The MEG data corroborated this finding: the sources reflecting the entrained activity were localized in the hemisphere contralateral to the rhythmic stimulation. This result is consistent with studies using TMS to entrain respectively the left or right hemispheres (Romei et al., 2010); we now provide evidence that local entrainment of brain activity in the visual cortex can be obtained using visual stimulus trains. (Similar results seem to hold for frequency modulation of sound entraining the auditory cortex (Henry & Obleser, 2012).) An interesting hypothesis is that the alpha entrainment by visual stimulation we report here is responsible for the phenomenon known as the 'attentional blink'; recently, evidence for this hypothesis has been reported (Zauner et al., 2012).

A recent study (Jaegle & Ro, 2014) also reported entrainment of alpha activity (as measured by EEG), using TMS to either occipital or parietal cortex. Interestingly, however, they report a behavioral effect of their entrainment only when TMS was applied to the parietal cortex. This is in line with another TMS study reporting alpha entrainment after parietal stimulation (Thut et al., 2011). We report strong, behaviorally relevant, occipital alpha entrainment. Although the studies cited above (and others, e.g. (Hanslmayr et al., 2013)) show convincing evidence for the existence of a parietal alpha source, there is ample evidence that early visual cortex also contains alpha generators (Chapter 3, F. Lopes da Silva & Storm van Leeuwen, 1977; Bollimunta et al., 2008; Spaak et al., 2012) that are modulated with attention (Yamagishi et al., 2003; Bollimunta et al., 2011). It is conceivable that intrinsically occurring alpha modulations, such as those occurring in response to attentional cues, are top-down controlled by parietal cortex, while the consequences of this modulation are expressed in occipital areas. Given the medial and deep location of the primary visual cortex, it might not be easily entrainable by TMS, while the dorsal and lateral location of the parietal areas associated with alpha generation (surrounding the intra-parietal sulcus) is ideally located for transcranial stimulation. Entrainment using visual flashes as reported here is of course not subject to such anatomical constraints, as the stimulation is relayed directly by existing endogenous pathways.

The hit rate profile we observed was clearly periodic. It might be argued that these behavioral effects are not due to low-level entrainment of endogenous oscillators, but instead reflect temporal expectation. However, temporal expectation cannot explain our results, because it would predict the opposite pattern: subjects performed worse at in-phase delays (100/200/300 ms; see Figure 2.2A,B) than at anti-phase delays. Since the entraining stimuli were presented at 0, -100, -200,... ms, the temporal expectation hypothesis would predict an increased performance at in-phase delays (Cravo et al., 2013; Rohenkohl et al., 2012; Rohenkohl & Nobre, 2011). Presumably temporal expectation is associated with different neural mechanisms than those reflecting the entrainment we observed.

This brings us to an important point: it seems that (at least) two connotations of 'entrainment' are used in the literature. Temporal predictions and expectations are typically associated with entrainment of low-frequency neural oscillations (Lakatos et al., 2008; Schroeder & Lakatos, 2009; Cravo et al., 2013). This sense of 'entrainment' likely reflects an active mechanism by which the brain extracts temporal regularities from the environment. In contrast, the entrainment of alpha activity that the current chapter (and the cited papers on visual and TMS entrainment) is concerned with, is believed not to reflect such an active mechanism. Instead, this form of entrainment is likely a lower-level process which taps into kinetics of the neural system not specifically evolved to extract temporal information; this latter form of entrainment is more akin to resonance of endogenous neural oscillators.

Is the entrainment specific to 1̃0 Hz stimulation, or would stimulation at other frequencies have worked equally well? Importantly, since the entrained 10 Hz activity was sustained after the stimulus train for at least 300 ms, it is clear that the induced rhythm is maintained by endogenous mechanisms. Given the large amplitude of spontaneous alpha oscillations, we argue that the sustained entrained oscillations rely on the same mechanisms as the natural alpha oscillators. In support of this notion, previous entrainment studies targeting the visual system have shown that perceptual entrainment is maximal at 10 Hz (Romei et al., 2010; de Graaf et al., 2013), and that even non-rhythmic input can result in cortical 10 Hz resonance (VanRullen & Macdonald, 2012). Also, rhythmic stimulation at other frequencies than 10 Hz was shown to induce a 10 Hz-rhythmicity in perceptual performance (experiment 2 in (de Graaf et al., 2013)). Furthermore, an exhaustive test of many different visual stimulation frequencies has revealed that 10 Hz activity in the visual system shows by far the strongest resonance (Herrmann, 2001). Finally, although it has convincingly been argued that steady-state responses during stimulation are largely explained by a superposition of transient responses (Capilla et al., 2011), we note that our arguments in favor of entrainment are based primarily on effects observed after stimulation offset, when the superposition of transients would have already disappeared. We conclude that the 10 Hz visual stimulation used in the present study most likely entrains the neuronal generators responsible for creating the spontaneous alpha activity.

Our results provide evidence for the hypothesis that perception unfolds not in a fully continuous manner, but is instead at least partly discrete (VanRullen & Koch, 2003; Schroeder & Lakatos, 2009; Schroeder et al., 2010). The discrete sampling of visual stimuli has been proposed to be clocked by an internal oscillatory rhythm (N. A. Busch et al., 2009; Landau & Fries, 2012; Romei et al., 2010; Fiebelkorn et al., 2013), and we here add evidence indicating that alpha oscillations are involved in this clocking of perception. Previous work has found that oscillatory EEG activity with a fronto-central topography is most predictive of perception (N. A. Busch et al., 2009), yet here we report occipital alpha to be the critical factor. The frontal versus posterior components might reflect complementary mechanisms of temporal sampling, or they might interact to result in the observed perceptual modulation. Alternatively, since the study by

Busch et al. (2009) did not perform source analysis, it could also be the case that the observed EEG topography does not reflect the engagement of frontal sources. Further research is needed to shed light on the relation between a possible global rhythmicity in perception or attention, and the strongly localized oscillatory sampling we report here.

Most studies concerning the role of brain oscillations in perceptual and cognitive processes have relied on external cognitive cues to modulate the oscillations under scrutiny; e.g. a cue to covertly shift attention to one visual hemifield reliably induces a hemispheric lateralization in alpha band activity (Worden et al., 2000; Kelly et al., 2006; Rihs et al., 2007). Typical research questions have investigated how changes in neural oscillations affect cognitive performance. While these studies have provided important insights, claims made in this manner about the functional relevance of oscillations are correlative: the observed oscillations could be a consequence of some unobserved factor (which was the result of the cognitive cue), while this unobserved factor was also the cause of the cognitive change. A direct manipulation of endogenous brain oscillations allows researchers to make causal claims. We have here demonstrated that such a manipulation in the visual system is feasible by using visual stimulation.

Through employing the technique of visual alpha entrainment, our findings show that cortically highly localized alpha activity modulates visual perception in a phase-specific manner. It has been demonstrated that alpha oscillations are under strong top-down control when attention is allocated (Händel et al., 2011; Haegens, Händel, & Jensen, 2011; Bonnefond & Jensen, 2012). They may therefore function as a mechanism for rhythmic gain control of neuronal processing (Arnal & Giraud, 2012; Jensen et al., 2012), possibly through interaction with gamma activity (Chapter 3, Spaak et al., 2012; Lisman & Jensen, 2013). We show here that local alpha oscillations indeed are doing causal work; they are not an epiphenomenal consequence of some other attentional process. In future work it would be of great interest to investigate how the allocation of attention interacts with the entrained alpha oscillations.

CHAPTER 3

Layer-specific entrainment of gamma-band neural activity by the alpha rhythm in monkey visual cortex

3.1 Abstract

While the mammalian neocortex has a clear laminar organization, layer-specific neuronal computations remain to be uncovered. Several studies suggest that gamma band activity in primary visual cortex (V1) is produced in granular and superficial layers and is associated with the processing of visual input (Maier et al., 2010; Jensen et al., 2007; Fries et al., 2007). Oscillatory alpha band activity in deeper layers has been proposed to modulate neuronal excitability associated with changes in arousal and cognitive factors (Thut & Miniussi, 2009; Sauseng et al., 2009; Klimesch et al., 2007; Jensen et al., 2012). To investigate the layer-specific interplay between these two phenomena, we characterized the coupling between alpha and gamma band activity of the local field potential (LFP) in V1 of the awake macaque. Using multicontact laminar electrodes to measure spontaneous signals simultaneously from all layers of V1, we found a robust coupling between alpha phase in the deeper layers and gamma amplitude in granular and superficial layers. Moreover, the power in the two frequency bands was anticorrelated. Taken together, these findings demonstrate robust interlaminar cross-frequency coupling in the visual cortex, supporting the view that neuronal activity in the alpha frequency range phasically modulates processing in the cortical microcircuit in a top-down manner (Jensen et al., 2012).[1]

---

[1] The work in this chapter was previously published as Spaak, E., Bonnefond, M., Maier, A., Leopold, D.A., & Jensen, O. (2012). Layer-specific entrainment of gamma-band neural activity by the alpha rhythm in monkey visual cortex. Current Biology, 22(24), 2313–2318. doi: 10.1016/j.cub.2012.10.020.

3.2 Results

The laminar organization of the mammalian neocortex has been the subject of many anatomical studies (Callaway, 2004; Thomson & Bannister, 2003). This work has revealed a layer-specific organization both within cortical columns, as well as between brain areas including thalamic regions. To comprehend the functional role of this laminar organization it is essential to uncover the dynamical interactions between layers. Neuronal oscillatory activity dominated in V1 by the alpha (7-14 Hz) and gamma frequency bands (30 -200 Hz) has been demonstrated to be modulated during various types of processing and cognitive manipulations (Jensen et al., 2007; Fries et al., 2007; Thut & Miniussi, 2009; Sauseng et al., 2009; Klimesch et al., 2007; Jensen et al., 2012; Tallon-Baudry & Bertrand, 1999); however, the interactions between these frequency bands, and their laminar profile, remain poorly understood.

To better understand these interactions, we recorded spontaneous cortical activity from V1 of two awake, healthy adult monkeys (Macaca mulatta) at rest using a 24-contact laminar electrode, which allowed us to simultaneously sample from all cortical layers (Figure 3.1A). Visual inspection of the local field potential (LFP) data revealed segments of high ongoing alpha activity amidst segments with much less pronounced alpha (see Figure 3.1B for an example), and parts of the analyses described here were restricted to such high-alpha segments (see Methods for details on the selection procedure). To minimize the contribution of volume conduction, we used locally bipolar LFP signals. The resulting mean power spectrum over all bipolar measurements during the high alpha epochs is shown in Figure 3.1C. A peak in the alpha band (most strongly at 8 Hz) embedded in the 1/f power spectrum that characterizes electrophysiological measures of brain activity (Bédard et al., 2006) is clearly visible.

3.2.1 Layer-specific entrainment of gamma power by the phase of the alpha rhythm

We found that LFP power in the gamma band (30-200 Hz) was coupled to the phase of the alpha rhythm measured from electrodes in the infragranular layers. This was observed by aligning time-varying power in the LFP spectrum to peaks of the alpha rhythm in infragranular layers. Averaging a total of 3000 peak-aligned traces resulted in a characteristic wavelet shape (Figure 3.2D). The mean time-frequency representations (TFRs) of power aligned to the infragran-

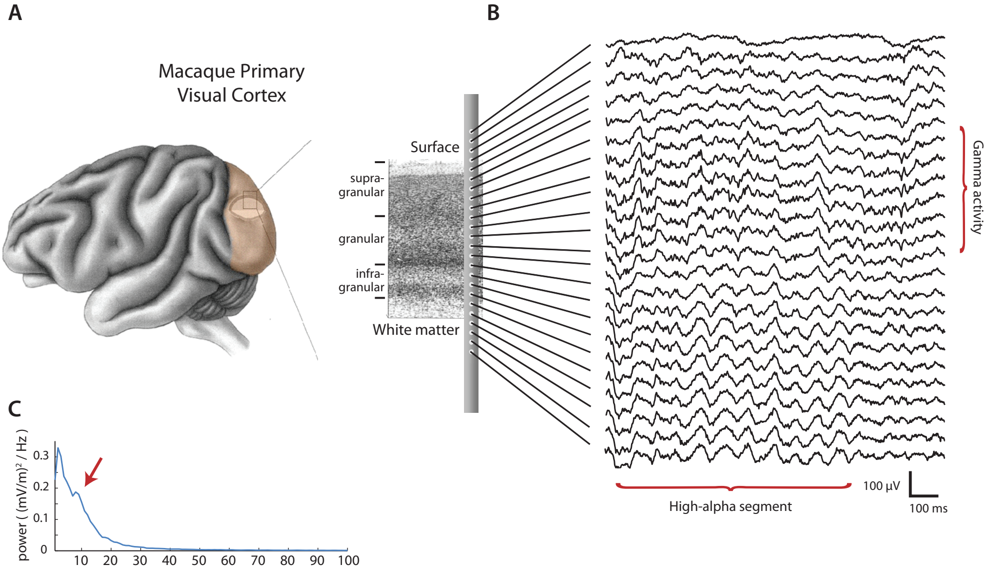

FIGURE 3.1: Overview of the type of data we acquired **(A)** Continuous electrophysiological activity was simultaneously recorded from all layers of primary visual cortex using a 24-contact laminar probe in two monkeys. **(B)** Example of the recorded voltage traces. The example traces shows more prominent gamma activity in the superficial layers, and a transient segment of alpha activity in the deep layers (about 9 cycles). **(C)** The power spectrum of bipolar data in infragranular layers. Note the local peak at in the alpha band, indicated by the arrow.

ular alpha peaks for the different layers demonstrated a clear coupling between the power in the 50-200 Hz range and the phase of the alpha rhythm (Figure 3.2). This modulation was most pronounced in the supragranular and granular layers, reaching nearly 20% (Figure 3.2A,B). The modulation was smallest in the infragranular layers (Figure 3.2C; sign test of mean rectified TFR; supragranular versus infragranular: $p < 10^{-8}$; granular versus infragranular: $p < 10^{-9}$; supragranular versus granular: n.s.), demonstrating that the coupling is not just within-layer but involves interaction between different laminar compartments. This result cannot be attributed to the high-alpha selection procedure, since qualitatively similar results were obtained when using the entire dataset (not shown in figure).

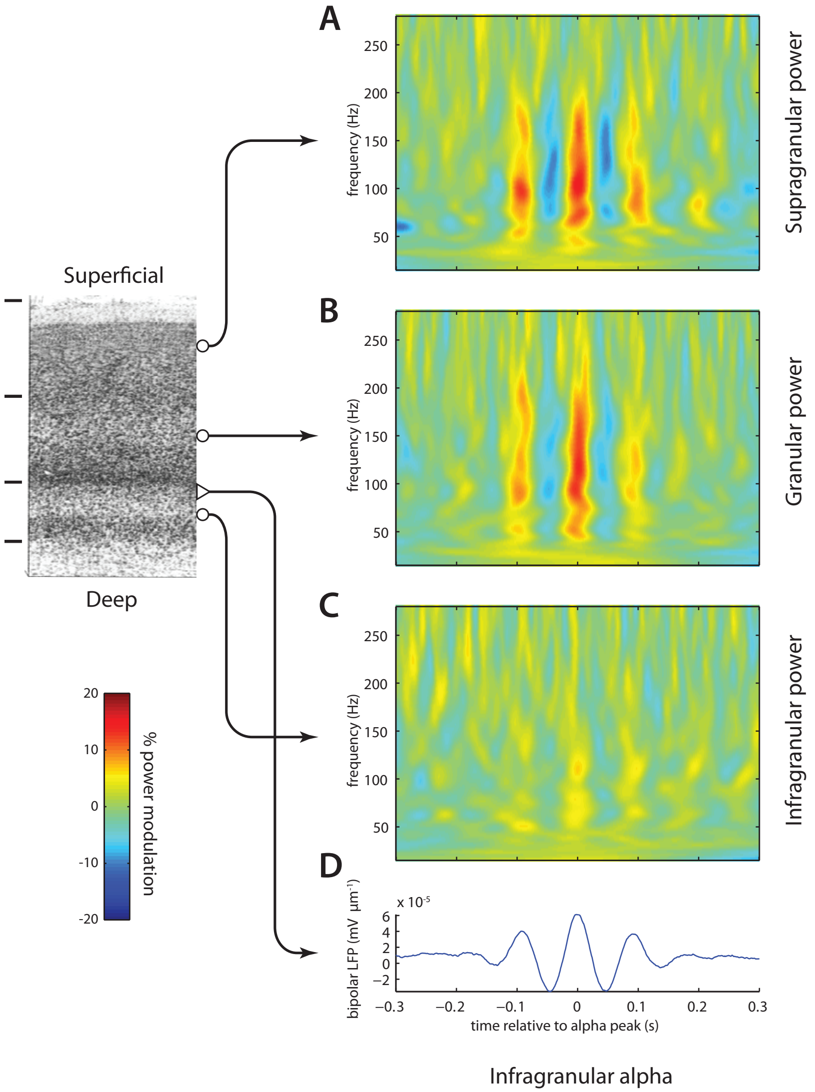

FIGURE 3.2: Time-frequency representations (TFRs) of power for epochs time-locked to the peaks of the alpha rhythm. The TFRs were calculated per epoch and then averaged. The TFRs for the supragranular **(A)** and granular **(B)** layers reveal a robust modulation in the gamma activity (50-200 Hz) phase-locked to the alpha oscillations. The modulation was virtually absent in the infragranular layers **(C)**. The TFRs were normalized relatively to the average power per frequency. The averaged unfiltered traces reveal alpha activity in the bipolar LFP **(D)**. The averaged TFRs and LFPs were calculated from 3000 epochs.

3.2.2 Phase-amplitude coupling across frequencies and layers

In contrast to the analysis in the previous section, where the selection of a given frequency and electrode position might affect the observed coupling pattern, we next applied a data-driven approach in which all positions and frequencies were analyzed for phase-amplitude coupling. Figure 3.3A shows cross-frequency coupling of phase and amplitude (Tort et al., 2010), with the phase derived from the LFP signal in the infragranular layers and the amplitude measured from either the supragranular layers (upper panels) or granular layer (lower panels). Coupling was specific to gamma band amplitude locked to the phase in the alpha band ($p < 0.001$ to $p < 0.05$; cluster-based permutation test). In both monkeys, significant coupling was found in two separate gamma bands (Colgin et al., 2009) (30-70 Hz and 100-200 Hz). This division was most evident when considering infragranular phase and granular amplitude. It has been proposed that some of the power in the high gamma band (> 100 Hz) can be explained by broadband contributions from spiking activity (Belluscio et al., 2012), whereas 30-70 Hz power is a consequence of oscillatory neuronal synchronization. In future work it would be of interest to quantify the contribution from spiking to the high gamma band. This would require an independent measure of neuronal spiking, which the present data does not contain.

Figure 3.3B presents gamma amplitude binned as a function of alpha phase. Across the two monkeys, the gamma amplitude showed a phase modulation exceeding 10%, with somewhat stronger coupling in the granular than supragranular compartments. Note that this percent modulation is robust, but somewhat smaller than that reported in Figure 3.2. The smaller modulation may be due to a lack of phase stationarity in the alpha band signal, leading to an effective decrease in the coupling magnitude.

To determine the laminar profile of the observed phase-amplitude coupling, we computed the alpha-to-gamma modulation index between all possible electrode combinations. Results for this analysis are shown in Figure 3.4, where 0 is defined as the center of the granular layer (Maier et al., 2010, 2011). This plot revealed a well-circumscribed region of increased coupling between the infragranular alpha phase at around -300 μm and the supragranular gamma amplitude around 700 μm (yellow arrow). The coupling between alpha phase in deeper layers to gamma amplitude in supragranular layers was highly consistent across both animals. The coupling between signals from different locations alleviates concerns that the phase-to-power coupling is trivially explained by

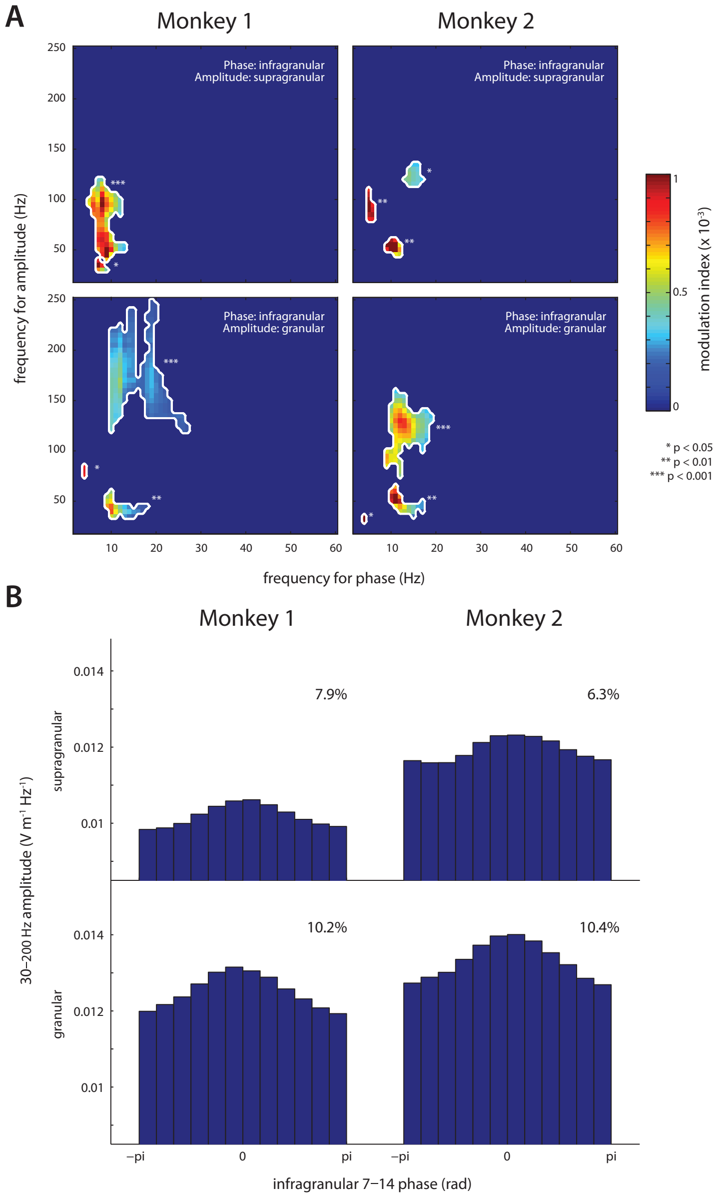

Figure 3.3: Modulation Index (MI) analysis for phase-amplitude coupling. **(A)** MI values as shown for four representative bipolar channel pairs (each from a single recording session). Only significant MI values are shown. The significance values are corrected for multiple comparisons by a shift-predictor cluster permutation approach. **(B)** Granular/supragranular gamma amplitude as a function of binned infragranular alpha phase, averaged over all recording sessions. The effect size of the modulation is shown in the inserts.

non-sinuodial properties of the alpha rhythm (e.g. a saw-tooth shape producing broadband power at given phases) . In addition, we found a region of increased coupling between the alpha phase at around -300 μm and the gamma amplitude at the same laminar position (white arrow).

3.2.3 Gamma amplitude and burst duration are inversely related to alpha amplitude

Consistent with the notion that alpha activity serves to inhibit neuronal processing (Klimesch et al., 2007; Jensen et al., 2012), we here report that alpha and gamma amplitude are inversely correlated. We investigated the correlation between the alpha and gamma amplitude on a 2 s, segment-by-segment basis. To control for non-physiological signals producing spurious correlations we used a partial correlation analysis controlling for the contribution from broadband (7-200 Hz) activity. We found significant negative correlations between the alpha amplitude around -300 μm and the gamma amplitude either at that same location (monkey 1: $r_{\alpha\gamma\circ\text{broad}} = -0.38$; monkey 2: $r_{\alpha\gamma\circ\text{broad}} = -0.50$), or at 700 μm (monkey 1: $r_{\alpha\gamma\circ\text{broad}} = -0.22$; monkey 2: $r_{\alpha\gamma\circ\text{broad}} = -0.29$; all $p < 0.001$). (See Figure 3.5 for a similar analysis in which we estimated gamma amplitude separately for different alpha phases: we find a more negative correlation when gamma amplitude is estimated at the alpha troughs versus at the alpha peaks.)

Next we found that long gamma bursts were predominantly observed during periods of low alpha amplitude (Figure 3.6). We detected gamma bursts (defined as 5-50ms segments exceeding the 60^{th} percentile of gamma amplitude) and computed the infragranular alpha amplitude in a 100 ms window around the bursts. The alpha and gamma amplitude time series were normalized by dividing both by the broadband (7-200 Hz) amplitude time series. In both monkeys, we found a weak, but highly significant, negative correlation between the length of a gamma burst and the alpha amplitude in a window around it (monkey 1: $r = -0.070$, $p < 10^{-5}$, monkey 2: $r = -0.067$, $p < 10^{-3}$).

3.2.4 Current sources of gamma-coupled alpha rhythm suggest an infragranular generator

To identify the generators of the alpha currents associated with the modulated gamma activity, we performed a current-source density (CSD) analysis (Mitzdorf, 1985). We detected troughs in the alpha band in a supragranular unipolar elec-

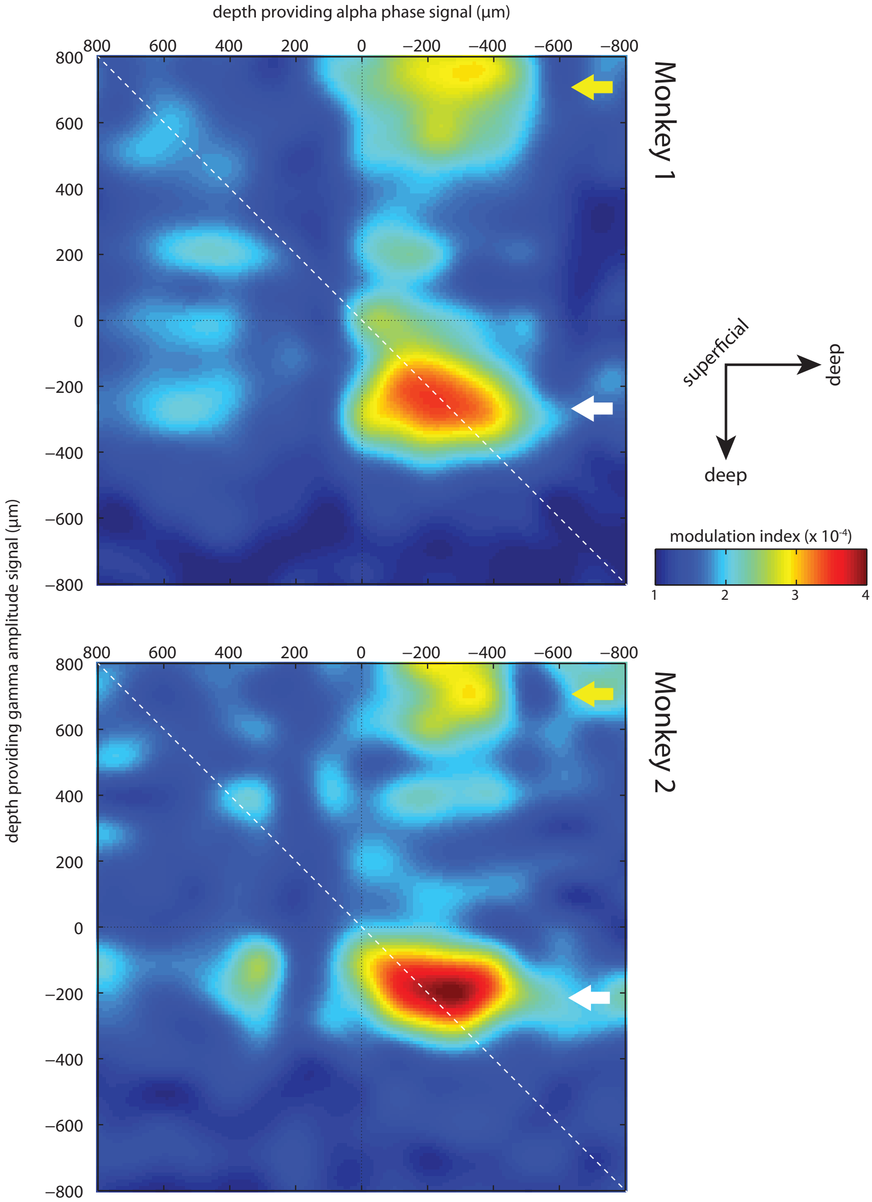

FIGURE 3.4: Topographical representations of the alpha (7-14 hz) to gamma (30-200 Hz) MI when considering all electrode combinations. The arrows indicate the deep layer alpha phase modulation of the granular (white arrow) and supragranular (yellow arrow) gamma amplitude.

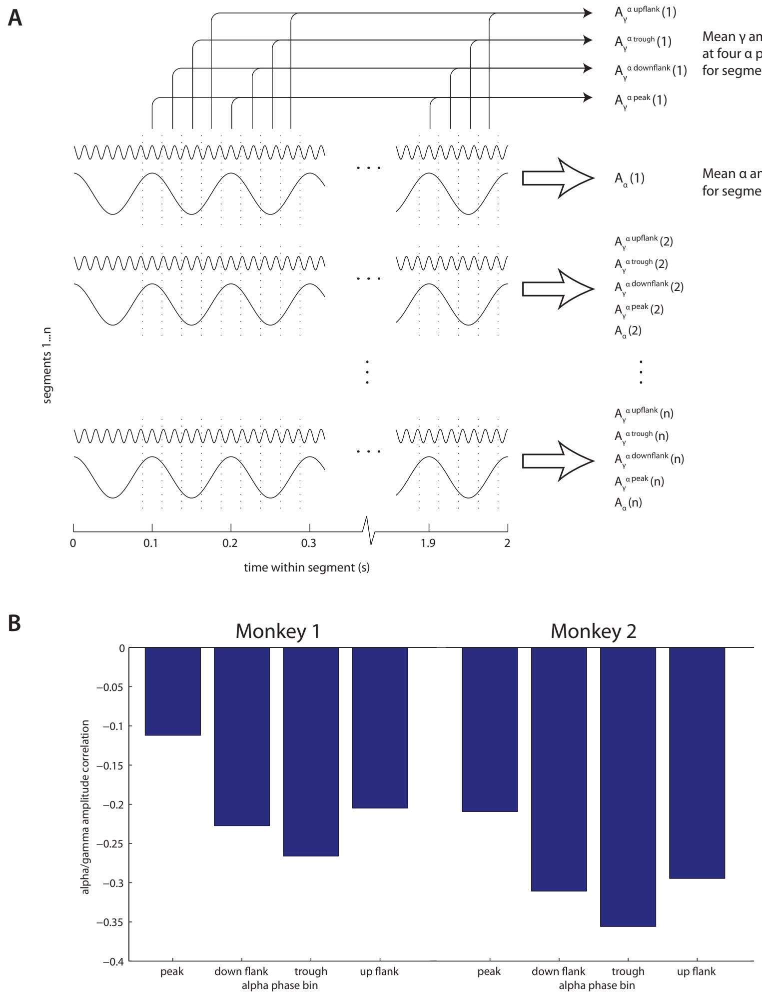

FIGURE 3.5: Correlations between alpha and gamma amplitude, on a 2s-long segment-by-segment basis, as a function of alpha phase. **(A)** A graphical depiction of the analysis protocol. The alpha cycles were partitioned in four phase bins (peak, down-flank, trough, up-flank). For each phase bin, the mean gamma amplitude was estimated per segment and correlated with alpha amplitude for the same set of segments. **(B)** Correlation values for both monkeys. Note that the anti-correlations were strongest at the trough of the alpha cycle (significantly different from peak in both monkeys; Meng's z-test for dependent correlations, $p < 10^{-15}$). All correlations were found to be significantly different from zero at $p < 0.01$.

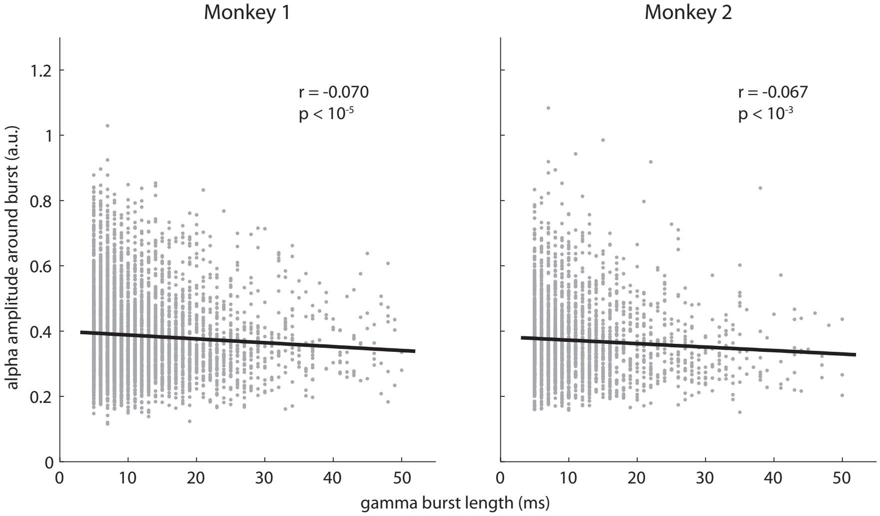

FIGURE 3.6: Relationship between gamma (30-200 Hz) burst length (i.e., the consecutive time during which gamma amplitude was above a certain threshold), or "duty cycle", and the alpha (7-14 Hz) power surrounding those bursts.

trode located at 700 µm. Around the alpha troughs, we averaged segments of LFP activity (Figure 3.7A), and estimated the CSD (Figure 3.7B). A clear alternating sink/source pattern can be observed straddling the granular/infragranular boundary.

Next, we aimed to find the generators associated with the modulation of the superficial gamma activity by aligning the LFP traces to the incidences of gamma bursts. We first detected peaks in the gamma activity at the superficial unipolar electrode located at 700 µm (Figure 3.8A; black arrow). We then averaged epochs around these peaks. This analysis revealed a clear nesting of gamma bursts in the lower frequency oscillation of the LFP (Figure 3.8A; superimposed blue lines indicate 7-14 Hz band-pass filtered signals) (Chrobak & Buzski, 1998).

The CSD of these traces revealed a prominent low-frequency sink in the granular layer coinciding with the gamma burst, accompanied by a source directly below (Figure 3.8B). Approximately 70 ms before and after the gamma burst, sinks were apparent in the infragranular layers (probably layer 5), and were accompanied by sources in the granular layer. Calculating the CSD aligned

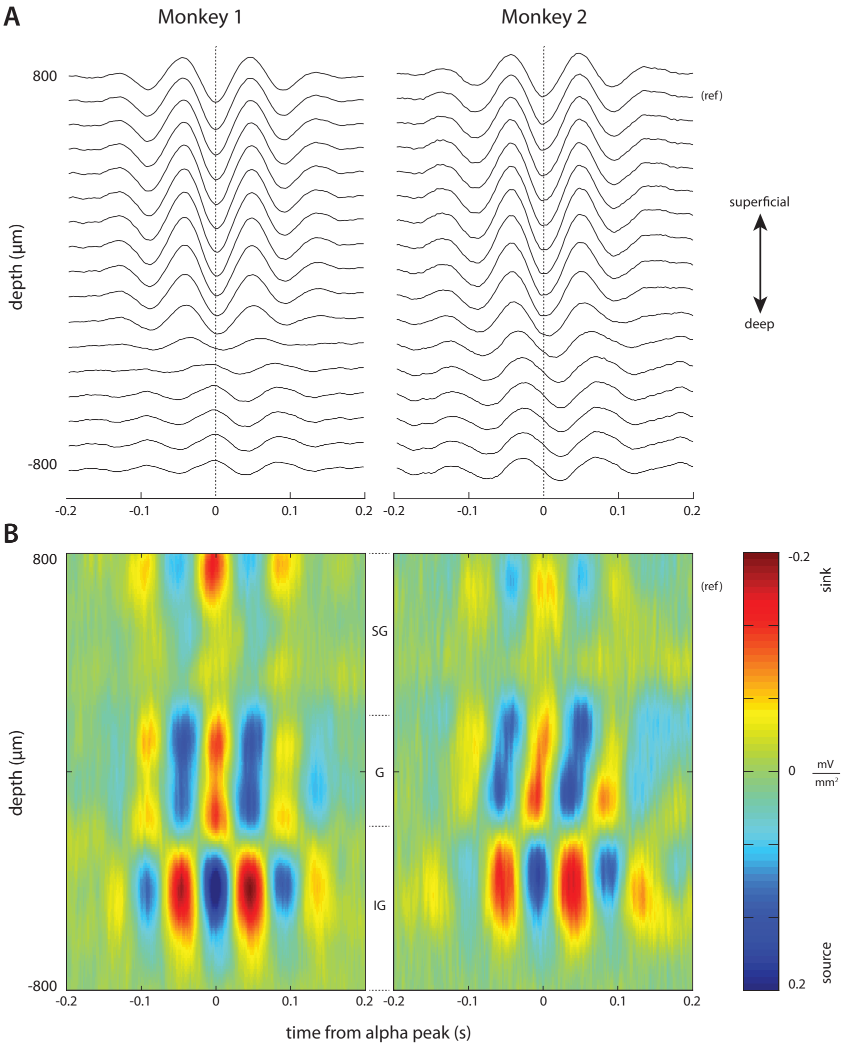

Figure 3.7: Laminar activity time-locked to alpha troughs. **(A)** Average voltage traces phase-locked to alpha troughs. The troughs were identified in the superficial layers (reference electrode indicated with "(ref)"). **(B)** Current-source densities for the traces shown in A.

to gamma bursts measured from the granular layers yielded comparable results (data not shown). The spatial distribution for the alpha-aligned current sources and sinks is highly similar to the sinks and sources we find when aligning to gamma bursts (compare Figures 3.7B and 3.8B). However, note that the frequency for the alpha-aligned CSD is around 10 Hz, while the gamma-burst-aligned CSD frequency is slightly lower. Overall, the laminar pattern of sinks and sources associated with the alpha rhythm and gamma bursts are highly consistent across both monkeys.

3.3 Discussion

Using laminar neurophysiological recordings, we have demonstrated that the amplitude of gamma activity (30-200 Hz) is coupled to the phase of alpha oscillations (7-14 Hz) within the V1 cortical microcircuit. This coupling is spatially specific: gamma activity in the granular and supragranular layers is coupled to the phase of alpha oscillations with generators extending to infragranular layers. Furthermore, fluctuations in the alpha amplitude are inversely related to both the amplitude and burst length of the gamma activity.

In humans it has been demonstrated that the phase of the alpha rhythm is predictive of perception (Mathewson et al., 2009; N. A. Busch et al., 2009; Dugué et al., 2011), BOLD responses (Scheeringa et al., 2011), and gamma band activity (Osipova et al., 2008; Voytek et al., 2010a). Laminar recordings in monkey have identified gamma generators in granular and supragranular layers (Maier et al., 2010) and alpha generators in deeper layers (Maier et al., 2011; F. Lopes da Silva & Storm van Leeuwen, 1977; Bollimunta et al., 2011; van Kerkoerle et al., 2011) (albeit there is also evidence for supragranular alpha generators (Bollimunta et al., 2011)) . We now add to this body of work by revealing an intimate relationship between the neuronal dynamics in the alpha and gamma band: the alpha activity in deeper layers modulates the gamma band activity in granular and supragranular layers in a suppressive, phase-specific manner.

It bears emphasis that most analyses were restricted to data segments exhibiting pronounced alpha activity, with 'high-alpha' periods amounting to a small proportion of our extensive dataset (approximately 3% using a conservative threshold, see Methods for details). In humans, the fraction of alpha-rhythm in V1 during rest is considerably greater. We cannot rule out that the low fraction of alpha rhythm in both monkeys stemmed from active exploration of the room,

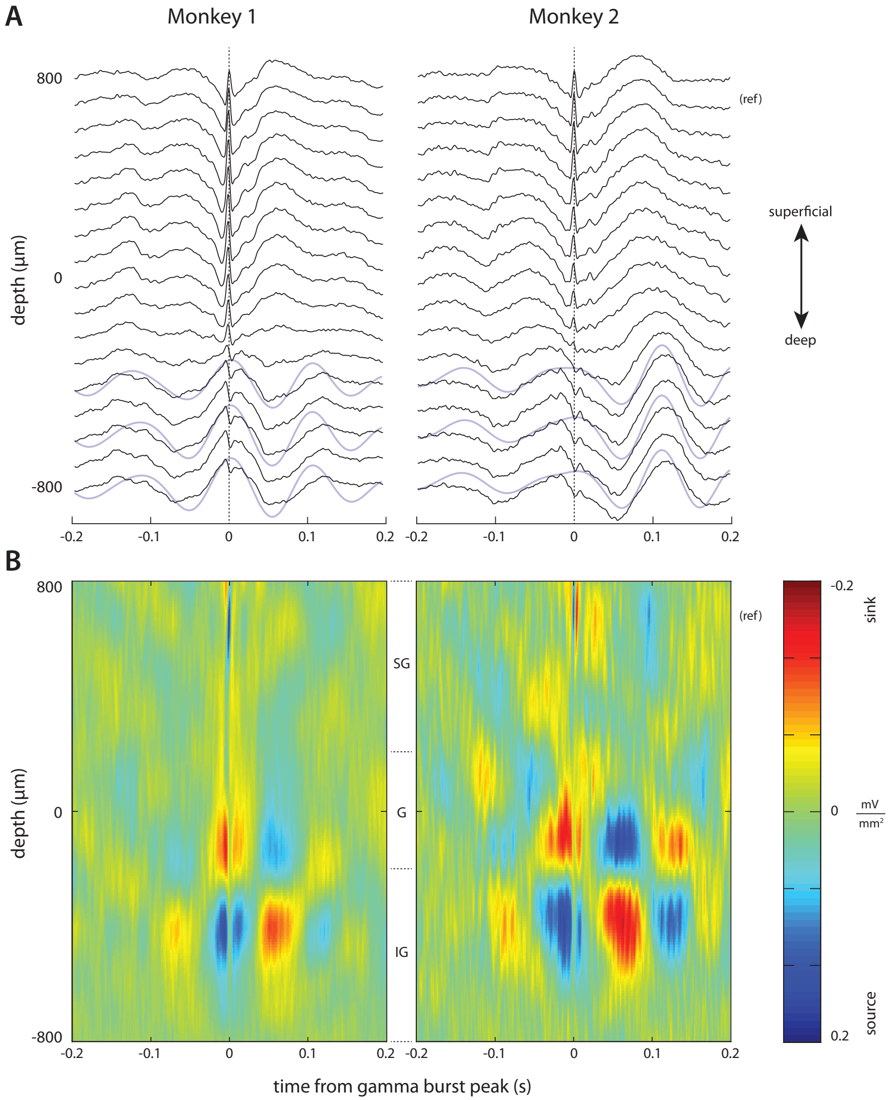

Figure 3.8: Laminar activity time-locked to gamma bursts. **(A)** Average voltage traces phase-locked to gamma bursts. The arrow on the right indicates the electrode used for identifying the gamma activity in superficial layers. In the raw averaged traces, a low-frequency profile emerges in the deep layers. Superimposed blue lines indicate 7-14 Hz band-pass filtered signals for three infragranularly located electrodes. **(B)** Current-source densities, computed on the traces shown in C. The high-frequency source-sink string at +700 μm is due to the gamma alignment. Alpha-frequency sink/source alternations are apparent around -100 μm and -400 μm.

though this seems unlikely given the absence of novel or interesting events. Comparing the prevalence of high amplitude alpha rhythm in the macaque to that in humans would require a controlled, comparative study between the two species. In the present study, our results were qualitatively similar when we applied the analysis to the entire data set, demonstrating that the coupling between frequencies is not only present during periods of high-amplitude alpha. It should be noted that some of the effects we assign to the alpha band at 7-10 Hz overlaps with the theta frequency range. However, given that we study the visual system, the generators were in the deeper layers of V1, and the 7-10 Hz activity correlated negatively with gamma amplitude, we deemed the term alpha to be appropriate. Nonetheless, for some of our analyses, coupling did extend well into the theta range and below (i.e. < 8 Hz; see Figure 3.3A).

It has been proposed that neuronal synchronization in the gamma band, as observed for instance during visual processing (Maier et al., 2010; Jensen et al., 2007; Fries et al., 2007), results in a stronger drive to downstream regions. Thus, modulating the degree of this synchronization might serve as a mechanism for feed-forward gain control (Salinas & Sejnowski, 2001). Indeed, when attention is allocated to a specific spatial location, visual stimuli elicit stronger gamma spike-field coherence in V4 neurons whose receptive fields correspond to that location (Fries et al., 2001). Furthermore, in V1, V2 and V4, alpha synchrony in deep layers decreases with attention, while gamma synchrony in superficial layers increases (Buffalo et al., 2011). Since alpha band activity is strongly modulated by spatial attention tasks, independently of whether there is visual stimulation present, and suppressed by visual input, this rhythm has been proposed to reflect top- down modulation of neuronal processing; specifically, it is thought to functionally inhibit sensory brain regions (Thut & Miniussi, 2009; Klimesch et al., 2007; Jensen et al., 2012; Haegens, Nácher, et al., 2011).

Our results do not conclusively demonstrate the directionality of the coupling between alpha and gamma band activity: while alpha activity could phasically modulate gamma activity, it is also conceivable that gamma activity has a causal impact on alpha phase instead. However, alpha is strongly modulated in a top-down manner even in the absence of visual input, in contrast to gamma activity, whose modulation is directly linked to the processing of visual stimuli. Therefore, we hypothesize a mechanism in which alpha activity modulates neuronal processing reflected in the gamma band, and thus implements a mechanism for gain control. Such gain control might be implemented by regulating the duty cycle of processing within an alpha cycle. Strong alpha activity allows for only short bouts of processing to occur, while low alpha activity allows for longer bouts of processing (see Figure 3.5, and (Jensen et al., 2012)).

Our CSD analysis of the ongoing alpha rhythm revealed sinks in the granular layer, co-occurring with sources in the infragranular layers (Figure 3.7B, Figure 3.8B). While it is difficult to pinpoint the precise basis for this pattern, one possibility would be that the zero-lag source is an active source corresponding to after-hyperpolarization currents in layer 5 (L5) cells (Wu & Okada, 1999). However, a more conventional interpretation would be that the zero-lag sink is active. While this sink might represent synchronized synaptic input to layer 4 neurons themselves, it could also arise from synapses on the proximal segment of L5 pyramidal cell apical dendrites (Mitzdorf, 1985), consistent with the involvement of infragranular neurons in the generation of the alpha rhythm (F. Lopes da Silva & Storm van Leeuwen, 1977). Such synchronized input to L5 cells would likely be effective in bringing these cells above firing threshold (Fries et al., 2007; Bernander et al., 1994). L5 pyramidal cells project to interneurons in the same layer (Kapfer et al., 2007; Silberberg & Markram, 2007), which in turn project to the superficial layers (Dantzker & Callaway, 2000; Xu & Callaway, 2009; Iurilli et al., 2012). This micro-anatomical pathway could explain how alpha oscillations exercise phasic inhibitory control over the gamma activity. Furthermore, this idea would be in line with recent findings demonstrating that cholinergic agonists concurrently enhance both attention and alpha activity (Bauer et al., 2012): L5 interneurons are specifically targeted by cholinergic afferents (Xiang et al., 1998). An alternative explanation to this intra-columnar route is that the deeper layers modulate gamma activity through a thalamic route. Electrophysiological studies have shown phase-coherence between alpha activity in the lateral geniculate nucleus of the thalamus (LGN) and early visual cortices (F. H. Lopes da Silva et al., 1980; Lorincz et al., 2009). Furthermore, infragranular layers are known to project to the LGN (Thomson & Bannister, 2003; Saalmann & Kastner, 2011). Since the LGN projects to the granular layer in V1, which in turn projects to superficial layers, such a cortico-thalamo-cortical interaction might also explain the present findings. Future research combining anatomy with electrophysiological stimulation and measurements is required to determine whether the intra-columnar alpha-gamma coupling we observe is due to purely cortical anatomical connections, or whether the thalamus is involved.

In conclusion, our findings are consistent with the notion that processing in the gamma band is clocked by slower rhythms (Lakatos et al., 2005; Buzsáki, 2006). In future work it would be of great interest to investigate how the interaction between alpha and gamma activity changes with attentional demands. Furthermore, it would be important to elucidate the physiological mechanisms implementing the cross-frequency interactions, as they are currently not well understood.

3.4 Methods

3.4.1 Experimental procedures

Two healthy adult male monkeys (Macaca mulatta), 98X009 (monkey 1) and CB35 (monkey 2) were implanted with a 24-contact (100 µm inter-contact spacing) electrode spanning all six layers of gray matter in primary visual cortex (V1). Laminar local field potential (LFP) was collected during 13 recording sessions (6 in monkey 98X009), filtered between 1 and 200 Hz and digitized at 1 kHz.

During each recording session, about 20 minutes of spontaneous, awake, activity was recorded. All analyses reported here were based on the data collected in this spontaneous condition. In addition, the monkeys spent some time each session viewing an occasionally flashing screen. Data from this condition were used to determine the center of layer 4C in each session with respect to the electrode, as it is known that the first short-latency current sink (as revealed by current -source density (CSD) analysis) in response to visual stimulation corresponds to this layer (Mitzdorf & Singer, 1979; Schroeder et al., 1991). The center of the initial sink was defined as depth 0 µm, with more positive values corresponding to more superficial, and more negative corresponding to deeper.

All relevant aspects of the experimental procedure were approved by the United States Institutional Animal Care and Use Committee (IACUC). Surgery, recording, and cross-session alignment are described in more detail in (Maier et al., 2010).

3.4.2 Offline data preprocessing

Analyses for Figures 3.2And 3.3were performed on a next-neighbour locally bipolar derivation of the data, where each electrode was referenced to the electrode located +200 µm superficially. We used this, rather than the raw LFP, because we were specifically interested in coupling between different layers of the cortex. Since volume-conducted potentials are quite prominent in laminar data, using raw LFP could yield positive between-channel coupling results, even for relatively distant channels, while the actual coupling was within-layer. Alternatively, the second-order spatial gradient, or CSD, could have been used, but unfortunately CSD estimates of unaveraged data are very noisy and could thus yield spurious results.

Our data contained segments of high ongoing alpha activity amidst segments with much lower alpha. We restricted the modulation index analysis to using only segments in which alpha power was above the 60th percentile of the alpha power distribution for a minimum time of 800ms. For both monkeys, this led to about 3% of the data being classified as high-alpha. For monkey 1, this meant that 186 segments were classified as such; for monkey 2, this value was 94. High-alpha epochs were constrained to be 1s long; i.e. exactly 1s of data centered on the occurrence of a (minimally 800ms long) high-alpha epoch was selected for further analysis. The average inter-epoch interval was 26s for monkey 1 and 33s for monkey 2.

Data analyses were performed using MATLAB R2011a (MathWorks Inc.), either with custom scripts or with the FieldTrip toolbox (Oostenveld et al., 2011).

3.4.3 Alpha-aligned time-frequency representations

For the results presented in Figure 3.2, we band-pass filtered the infragranular alpha signal using a two-pass least-square finite impulse response (FIR-LS) filter between 7 and 14 Hz, with a filter order of 426. After detecting peaks in this filtered signal (1960 peaks for monkey 1 and 1004 for monkey 2), we averaged the raw traces in segments around these peaks, resulting in the bottom panel of Figure 3.2. We also averaged the time-frequency representations (TFRs) of the infragranular, granular, and supragranular signals. To obtain these TFRs, we used a variable- length sliding time window, applied a single Hanning taper to each time segment, and computed spectral power for each such window. The size of the time window was determined by the frequency that was estimated (frequencies between 20 and 300 Hz were estimated, in steps of 2 Hz) and was always such that exactly 7 cycles of the estimated frequency fit the window.

3.4.4 Modulation Index analysis

In order to quantify phase-amplitude coupling in a single scalar, as a function of frequency for phase and frequency for amplitude, we used a technique known as the Modulation Index (MI) (Tort et al., 2010). To estimate instantaneous phase in a given channel at a given frequency fphase, we band-pass filtered the data from that channel in a band 2 Hz wide, centered around fphase, and used the angle of the Hilbert-transformed band-pass filtered data as our phase estimate. To estimate instantaneous amplitude at fampl, we band-pass filtered the data in a band 10 Hz wide, centered around fampl, and used the magnitude of the Hilbert-transformed band-pass filtered data as our amplitude estimate. Filters were FIR-LS, and filter orders were frequency-determined; specifically, the filter order was always set to three cycles of the lower bound of the frequency bandwidth.

To compute the MI (for a given channel pair, and a given frequency pair), we divided the phase signal into 12 bins, and then, for each bin, computed the mean amplitude for that bin. This yields a distribution of amplitude as a function of phase. The MI is defined as the Kullback- Leibler distance between that distribution and the uniform distribution (over the same number of bins). Low MI values correspond to a more uniform distribution, thus to low phase-amplitude coupling, while high MI values correspond to high phase-amplitude coupling. Shown in Figure 3.3A are example frequency X frequency-plots of MI values, each corresponding to a single channel pair.

To assess the statistical significance of the MI values (as a function of frequency for phase and frequency for amplitude), we performed a cluster permutation test. Specifically, we randomly shifted the phase time series, and computed the MI using this shifted signal. We repeated this procedure 1 000 times, resulting in a distribution of MI values (the "MI-level reference distribution"), still as a function of frequency for phase and frequency for amplitude. We thresholded both the observed MI data and all 1 000 randomizations to the 90th percentile of the MI -level reference distribution; this thresholding provided us with our initial cluster candidates. Neighbouring MI tiles were assigned to the same cluster. For all randomizations, we computed the score of the maximally observed cluster, where a cluster score is the sum of all MI values within that cluster. The resulting 1 000 maximum cluster scores formed the cluster-level reference distribution. For our observed clusters, significance levels were determined by comparing the observed cluster scores to the reference distribution; clusters with a score higher than the 950th element in the reference distribution are considered statistically significant.

For Figure 3.4, the topographical representation of alpha/gamma MI values, we averaged the MI values over the alpha (7-14 Hz) and gamma (30-200 Hz) bands. This yielded a 23 × 23 matrix of averaged MI values, with rows and columns each corresponding to our 23 bipolar channels. We interpolated these values tenfold across space using a cubic spline interpolation. Interpolation was needed because the 0-point was located at a particular channel in some sessions, and between channels in others. We then aligned all sessions to their 0-point and averaged. Channels more than 800 μm away from the 0-point were ignored, since they were possibly located in either white matter or above the pia mater. This analysis yields a spatial map of MI (Figure 3.4).

3.4.5 Current-Source Density analysis

For Figure Figure 3.7, we estimated alpha band activity from the unipolar electrode located at $+700\mu m$, by band-pass filtering the signal between 7 and 14 Hz using a FIR-LS filter. We detected troughs in this signal, and averaged 400ms of unipolar activity, in all electrodes, around these troughs. These raw traces are shown in Figure 3.7A. We computed an estimate of the corresponding current-source density (CSD) by calculating the discrete second spatial derivative, setting the inter- contact distance to a unit spacing:

$$CSD(t,k) = x(t,k-1) + x(t,k+1) - 2x(t,k)$$

where x(t,k) is the voltage measured at timepoint t at electrode contact k. Using this formula, sinks are indicated by positive values (hot colors), and sources are indicated by negative values (cool colors).

For Figure 3.8, we filtered the raw unipolar LFP signal from the electrode located at +700 μm between 30 and 200 Hz, again using a FIR-LS filter with frequency-dependent filter order. From this filtered signal, we estimated the amplitude distribution of gamma by using a Hilbert transform. We detected peaks in the gamma signal, where a peak was defined as a point in time where (1) the filtered gamma activity had a phasic peak, and (2) the mean gamma amplitude around the peak (30 ms on either side) had to be above the 90th percentile of the total gamma amplitude distribution. This led to 943 gamma peaks being identified for monkey 1, and 266 for monkey 2. Around these peaks, we averaged 400 ms windows of activity for all channels. The results of this averaging are shown in in Figure 3.8A. Traces were high-pass filtered at 4Hz, to remove any very- low frequency drifts in the data. The superimposed blue lines in Figure 3.8A were generated by band- pass filtering the data between 7 and 14

Hz. We computed the CSD of these averages as described above; the results of which are shown in Figure 3.8B.

For the averaging of the raw traces and CSDs across sessions, we interpolated the data tenfold across space using a cubic spline interpolation, just as for the MI topoplots. This ensured an accurate alignment of the different recording sessions, necessary for a valid average.

Chapter 4

Mechanisms of phase-amplitude coupling between hippocampus and prefrontal cortex

4.1 Abstract

The hippocampal theta and neocortical gamma rhythms are two prominent examples of oscillatory neuronal activity. The hippocampus has often been hypothesized to influence neocortical networks by its theta rhythm, and, recently, evidence for such a direct influence has been found. We examined a possible mechanism for this influence by means of a biophysical model using conductance-based model neurons. We found, in agreement with previous studies, that networks of fast-spiking GABA-ergic interneurons, coupled with shunting inhibition, synchronize their spike activity at a gamma frequency and are able to impose this rhythm on a network of pyramidal cells to which they are coupled. When our model was supplied with hippocampal theta-modulated input fibres, the theta rhythm biased the spike timings of both the fast-spiking and pyramidal cells. Furthermore, both the amplitude and frequency of local field potential gamma oscillations were influenced by the phase of the theta rhythm. We show that the fast-spiking cells, not pyramidal cells, are essential for this latter phenomenon, thus highlighting their crucial role in the interplay between hippocampus and neocortex.[1]

---

[1] The work presented in this chapter was adapted from Spaak, E., Zeitler, M., & Gielen, C.C.A.M. (2012). Hippocampal theta modulation of neocortical spike times and gamma rhythm: A biophysical model study. PLoS ONE, 7(10): e45688. doi:10.1371/journal.pone.0045688

4.2 Introduction

The hippocampal theta rhythm (3–8 Hz) and the neocortical gamma rhythm (30–100 Hz) are two prominent examples of oscillatory neuronal activity (Buzsáki, 2002; Buzsáki & Draguhn, 2004). The hippocampal theta rhythm is thought to reflect the "activation state" of the hippocampus (Buzsáki, 2002) and is important for the temporal coordination of a variety of functions (O'Keefe & Recce, 1993; O'Keefe & Burgess, 2005; Harris et al., 2002). In the neocortex, cell assembly formation, a crucial prerequisite for cognitive processing, is strongly associated with gamma oscillations (Fries, 2005; Gray et al., 1989; Gray & Singer, 1989).

Both the hippocampus and the neocortex, in particular the prefrontal cortex, seem to play complementary, yet highly interdependent, roles in the formation and retrieval of memories (Lavenex & Amaral, 2000; O'Reilly & Norman, 2002; Dolan & Fletcher, 1997; Eichenbaum, 2000). When we take this finding into account, along with the functional importance of the theta and gamma rhythms, it is not too far-fetched to hypothesize a direct influence of the hippocampal theta rhythm on neocortical networks.

Indeed, evidence for such a direct influence has recently been found. In both awake and sleeping rats, the hippocampal theta rhythm was found to bias both the spike times of individual neurons in prefrontal cortex and the occurrence of localized neocortical gamma oscillations ((Sirota et al., 2008; Siapas et al., 2005; Sirota et al., 2003); see also (Jones & Wilson, 2005)). Furthermore, in the human neocortex, the power of the "high gamma" rhythm (80–150 Hz) was found to be phase-locked to theta oscillations (Canolty et al., 2006). Importantly, this coupling between oscillations of different frequencies seems to have behavioral relevance: so far, evidence has been found to support cross-frequency coupling being involved in e.g. visual processing (Voytek et al., 2010b) and working memory (Axmacher et al., 2010).

The mechanisms by which the hippocampus is able to influence neocortical networks through its theta rhythm are not well-understood. The neuronal networks responsible for the generation of the gamma rhythm are better understood: there is quite some physiological and biophysical work available on this phenomenon (Bartos et al., 2007; Börgers & Kopell, 2003).

Interconnected networks of fast-spiking (FS) GABA-ergic interneurons with strong inhibitory chemical synapses as well as electrical synapses (gap junctions) tend to synchronize their spiking activity at a gamma frequency. Hence, they are thought to be responsible for the generation of the gamma rhythm in the neocortex (Tamás et al., 2000; Galarreta & Hestrin, 1999; Gibson et al., 1999; Wang & Buzsáki, 1996; Sohal & Huguenard, 2005). Importantly, this hypothesis has been confirmed by using a direct manipulation of the activity of fast-spiking interneurons, so the involvement of these cells goes beyond mere correlation (Cardin et al., 2009). Most likely, the inhibition involved in the synchronization of such fast-spiking interneurons is of the *shunting* type (Vida et al., 2006; Bartos et al., 2007). Shunting inhibition is a type of synaptic inhibition in which the reversal potential of the inhibitory synapse is above the postsynaptic cell's resting potential. This is different from *hyperpolarizing* inhibition, in which the reversal potential is below the resting potential. Thus, a shunting GABA-ergic synaptic event can actually be excitatory when the post-synaptic membrane potential is at or near the resting potential (Vida et al., 2006; Bartos et al., 2007).

Hippocampal efferent fibres project directly onto neurons of the prefrontal cortex (Dégenètais et al., 2003; Rosene & Van Hoesen, 1977). Both pyramidal cells and interneurons are the targets of these projections. The projections to the interneurons, however, are stronger than those to the pyramidal cells (Tierney et al., 2004; Gabbott et al., 2002).

Taken together, (1) the empirically observed interaction between the hippocampal theta and neocortical gamma rhythms, (2) the crucial role played by prefrontal cortex interneurons in the generation of the gamma rhythm, and (3) the preferential projection of hippocampal fibres onto these interneurons, led us to hypothesize that the fast-spiking interneurons of the neocortex are the key players in the mechanism by which the hippocampal theta rhythm influences neocortical networks. In this chapter, we analyze this possibility using a biophysical model of a network of conductance-based neurons.

We briefly summarize and preview our results as follows. First, we find that networks of coupled fast-spiking interneurons are robust gamma oscillators, in agreement with previous work (Wang & Buzsáki, 1996; Vida et al., 2006; Bartos et al., 2007; Sohal & Huguenard, 2005). Second, these interneurons impose their rhythm on pyramidal cells synaptically innervated by them. Third, hippocampal theta input to a coupled pyramidal cell/interneuron network results in theta-phase biased spike timings. Fourth, and most importantly, the frequency and amplitude of neocortical gamma oscillations are modulated by the phase of the hippocampal theta rhythm if and only if the neocortical fast-spiking interneurons receive hippocampal theta input; no such modulation is observed if only the neocortical pyramidal cells receive hippocampal theta input. Thus, we show that, indeed, neocortical fast-spiking interneurons are crucial for the

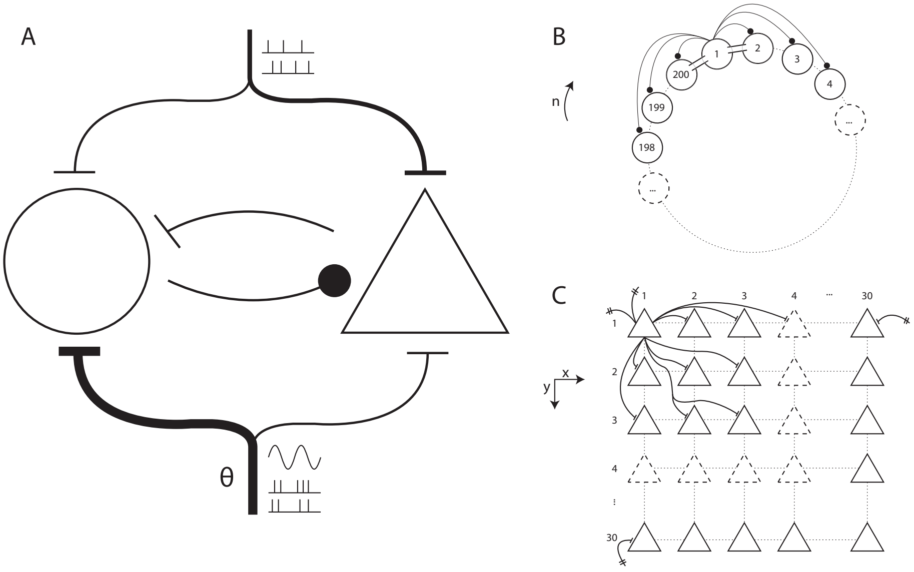

Figure 4.1: A patch of neocortex modelled by a network of interneurons coupled with a network of pyramidal cells. **(A)** The macroarchitecture of the model. Shown are the fast-spiking inhibitory interneuron network (circle, left), the pyramidal cell network (triangle, right), the cortical long-range afferent spike trains (top), and the theta-modulated subcortical afferent spike trains (bottom). **(B)** The ring-like structure of the interneuron model. Shown are some of the inhibitory synaptic connections (solid circles) and gap junctions ('conduits' between adjacent cells) for cell 1. **(C)** The two-dimensional structure of the pyramidal cell network. Shown are some of the excitatory synaptic projections from cell $(1, 1)$ to its neighbours. Note the projections to $(30, 1)$ and $(1, 30)$ are possible because the effective distance from $(1, 1)$ to those cells equals 1 (see Methods for details).

coupling between hippocampal theta and neocortical gamma rhythms that is observed in experimental physiology.

4.3 Results

To study the influence of hippocampal theta oscillations on neocortical spike times and gamma oscillations, we modelled a patch of neocortex by two interconnected subnetworks: one comprised of 200 fast-spiking inhibitory interneurons (FS cells), another comprised of 900 pyramidal cells (P cells). See Figure 4.1 for an overview of the architecture of the model.

The FS cells' membrane potential was governed according to Wang-Buzsáki equations (Wang & Buzsáki, 1996). They were arranged in a one-dimensional ring-like structure, and each cell was synaptically coupled to a subset of its neighbours, with a Gaussian probability, up to a maximum connection distance of 50 cells. Synapses within the FS cell subnetwork were GABA-ergic and shunting. Additionally, gap junctions were present between cells and their nearest neighbours. The first results reported in the present section concern only this FS cell subnetwork. Later on (as will become evident from the text), the P cell subnetwork was also involved.

The P cells were implemented as Hodgkin-Huxley model neurons (standard NEURON implementation) (Hodgkin & Huxley, 1952; Hines & Carnevale, 1997). They were arranged in a two-dimensional lattice-like structure, and each cell was synaptically coupled to a subset of its neighbours, with a Gaussian probability, up to a maximum (two-dimensional) connection distance of 8 cells. Synapses within the P cell subnetwork were glutamatergic and excitatory.

The two subnetworks were coupled to each other with synapses of the same type as the ones within each subnetwork. So, each P cell received shunting GABA-ergic innervation from a subset of FS cells, and each FS cell received glutamatergic innervation from a subset of P cells.

4.3.1 Gamma generation by a ring of fast-spiking cells

Networks of fast-spiking inhibitory interneurons with fast, strong, and shunting inhibitory synapses and gap junctions are hypothesized to be the main generators for the cortical gamma rhythm, and there is ample empirical evidence available that supports this hypothesis (Wang & Buzsáki, 1996; Bartos et al., 2007). In an attempt to replicate the results in the literature, we simulated the dynamics of a ring-like network of FS cells provided with a direct current input. The amplitude of the input current to the FS cells was determined by drawing a specific amplitude I from a Gaussian distribution with mean I_μ and a standard deviation determined by a coefficient of variation over cells $CV_{\text{cells}} = \frac{\sigma}{I_\mu}$. A high CV_{cells} results in different cells in the network having a highly heterogeneous input. This way of determining input current amplitude allowed us to study the effects of both net input drive and drive hetereogeneity on the synchronization properties of our network.

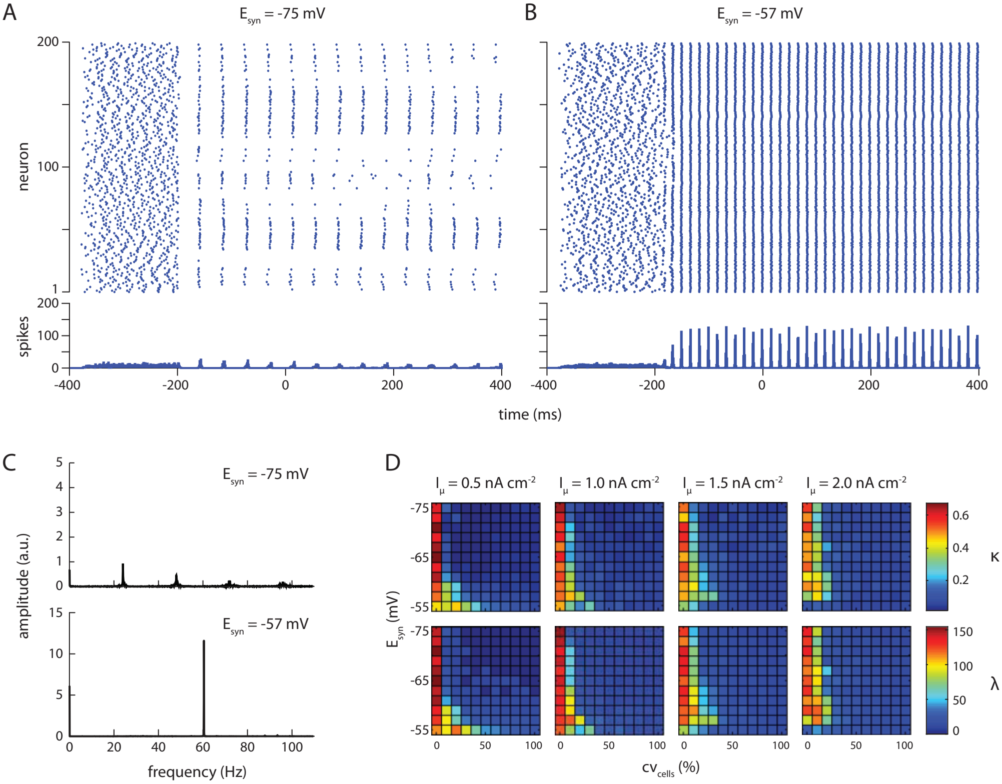

FIGURE 4.2: Shunting inhibition increases robustness in a network of fast-spiking inhibitory interneurons. **(A-B)** Rasterplots (top) and spike histograms (bottom) for simulations GABA-synaptic reversal potentials of -75 mV (A) and -57 mV (B). For these plots, mean drive $I_\mu = 0.5\,\text{nA cm}^{-2}$, drive variation $CV_{\text{cells}} = 10\,\%$. Synapses were activated at $t = -200$ ms; plots are truncated at $t = 400$ ms. **(C)** Amplitude spectra for spike histograms. Spectral analyses were performed on complete histograms, ending at $t = t_{\text{stop}} = 2\,047$ ms. **(D)** Two measures of network synchronization, network coherence κ (top row) and average spike volley peak height λ (bottom row), as a function of drive variation over cells CV_{cells} (x-axis), synaptic reversal potential E_{syn} (y-axis), and mean drive I_μ (separate columns). Shunting values of E_{syn} result in stronger synchronization with increasing drive heterogeneity.

When the amplitude of the direct current input is small (I_μ = 0.5 nA cm^{-2}) and for a moderate amount of variation over cells (CV_cells = 10 %), networks in which the GABA-synaptic reversal potential was hyperpolarizing (E_syn = −75 mV) show only weak synchronization (Figure 4.2A). Shunting GABA-synapses (E_syn = −57 mV), on the other hand, result in a strongly synchronized network (Figure 4.2B). Additionally, for shunting inhibition, nearly all cells in the network fire exactly once per gamma cycle, while the hyperpolarizing reversal potential of E_syn = −75 mV causes the strongly excited cells to silence out the more weakly excited ones (Kopell & Ermentrout, 2004). Fast-spiking interneurons firing once per gamma cycle, as we observe in our shunting inhibition condition, is in agreement with observations *in vitro* (Gloveli et al., 2005), *in vivo* (Fries et al., 2007; Csicsvari et al., 2003; Hasenstaub et al., 2005) and previous modelling work (Wang & Buzsáki, 1996; Bartos et al., 2002).

Spectral analyses of spike histograms revealed only a moderate peak near 23 Hz (and higher harmonics) for a synaptic reversal potential of E_syn = −75 mV (Figure 4.2C, top panel), while a strong peak at the gamma frequency of 60 Hz appears for a synaptic reversal potential of E_syn = −57 mV (Figure 4.2C, bottom panel).

To assess the effect of the synaptic reversal potential on network synchronization in a more general sense, we employed two different measures of network synchrony: network coherence κ (Wang & Buzsáki, 1996; see equation 4.8) and average volley peak height λ (see equation 4.10). As expected, these yield highly similar results, as revealed by correlation analysis ($r = 0.99$; $p < 0.0001$). κ and λ were consistently high with homogeneous drive (CV_cells = 0 %; Figure 4.2D, first column within each plot), and decreased with increasing heterogeneity (Figure 4.2D, x-axis of plots).

As reported previously (Vida et al., 2006), the rate of decrease with heterogeneity was dependent upon the reversal potential of the GABA-ergic synapses. Specifically, with a small drive of I_μ = 0.5 nA cm^{-2}, coherent oscillations ($\kappa \geq 0.15$) only occurred at heterogeneity levels of $CV_\text{cells} \leq 10$ % when synapses were hyperpolarizing (E_syn = −75 mV), while shunting inhibition (E_syn = −55 mV) resulted in coherent oscillations up to $CV_\text{cells} \leq 60$ % of heterogeneity (Figure 4.2D, left).

Interestingly, and to our knowledge not previously reported, the most robust synaptic reversal potential (i.e., the value of E_syn that results in coherent network synchronization up to the highest level of drive heterogeneity) changed when the amplitude of the input current was varied: for a drive of I_μ = 1.0 nA cm^{-2}, robust oscillations (up to $CV_{\text{cells}} \leq 30\,\%$) still occurred at $E_{\text{syn}} = -55\,\text{mV}$. When the drive was increased further to $I_\mu = 1.5\,\text{nA cm}^{-2}$, network synchronization was most robust at $E_{\text{syn}} = -57\,\text{mV}$ (up to $CV_{\text{cells}} \leq 30\,\%$; Figure 4.2D, third column of plots). At $I_\mu = 2.0\,\text{nA cm}^{-2}$, the optimal reversal potential for synchronization was $E_{\text{syn}} = -59\,\text{mV}$ (synchronization up to $CV_{\text{cells}} \leq 20\,\%$; Figure 4.2D, rightmost column of plots).

The optimal reversal potential seemed to continue to shift for even higher values of $I_\mu > 2.0\,\text{nA cm}^{-2}$, but, starting at $I_\mu = 2.5\,\text{nA cm}^{-2}$, the fraction of active cells in the network and dependence of network coherence on drive variation started to decrease markedly (data not shown).

4.3.2 Pyramidal cell network gamma oscillations by interneuron shunt

The previous section showed that gamma synchronization does indeed occur in the ring of coupled fast-spiking inhibitory interneurons in our model. The next step is to show that this mechanism is sufficient to drive gamma oscillations in a network of pyramidal cells.

To address this question, we investigated the behavior of a network of $30 \times 30 = 900$ pyramidal cells. Each P cell was synaptically coupled to, on average, 62 pyramidal cells. Additionally, the P cells received incoming synapses from simulated fibres carrying Poisson spike trains, modelling cortical background input. P cells projected to the fast-spiking cells with glutamatergic synapses. Each pyramidal cell received a variable number of incoming GABA-ergic synapses from the fast-spiking cells. These GABA-ergic synapses were of the shunting type.

First, we analyzed the spike times of the pyramidal cells. When the pyramidal cell subnetwork only received constant-rate Poisson spike train input and did not receive shunting inhibition from the fast-spiking cells, a non-synchronized activity pattern was observed (Figure 4.3A, top spike histogram). When the fast-spiking cells projected to the pyramidal cells, however, the latter tended to synchronize in a gamma rhythm (Figure 4.3A, bottom spike histogram). The gamma synchronization of the pyramidal cells involved a much smaller portion of cells than that of the fast-spiking cells: for the simulation shown, the maximum proportion of cells active in a single 1 ms time window was 1 % for the pyramidal cells and 63 % for the fast-spiking cells (compare Figures 4.2B, bottom spike histogram, and 4.3A, bottom spike histogram).

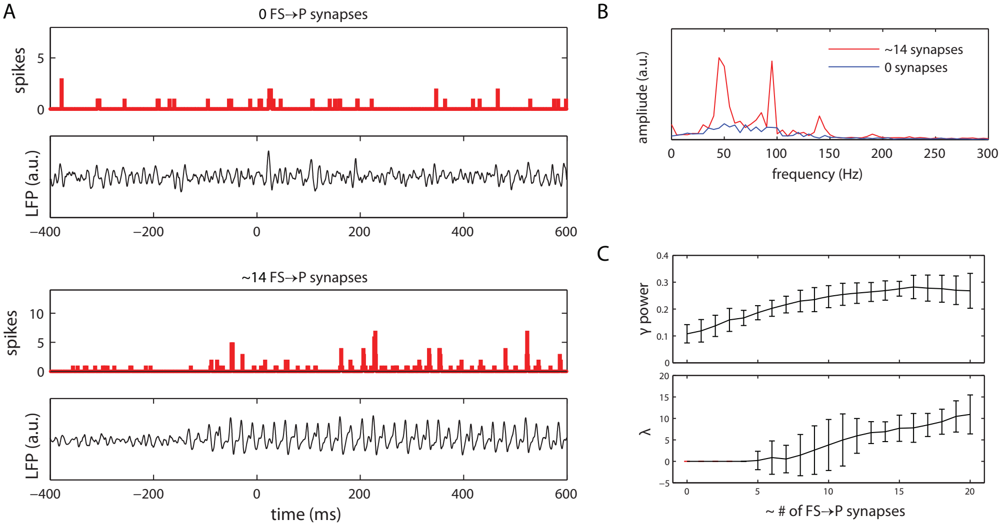

Figure 4.3: Pyramidal cells show gamma-synchronized activity when cells receive shunting inhibition. **(A)** Spike histograms and simulated LFP traces for the unconnected (0 FS to P synapses per P-cell) and connected (14 FS to P synapses per P-cell) conditions. Other input to the P-cells consisted of constant-rate Poisson spike trains. **(B)** Amplitude spectra for the simulated LFP in the connected (red) and unconnected (blue) conditions. The LFP spectrum for the connected condition shows a clear increase in power in the gamma band (30–80 Hz). **(C)** Relative gamma band power (top) and pyramidal cell network synchronization (bottom) as a function of the average number of GABA-ergic projections from the FS cells to a single P-cell. Relative gamma power increases steadily with the number of synapses, reaching a maximum at ≥ 15 synapses per P-cell. Network synchronization starts to occur at ≥ 5 synapses per P-cell. Shown are the mean values for 30 simulation runs; error bars represent 95 % confidence interval.

Apart from the spike times, shown in the histograms, we also analyzed the electrical activity of the pyramidal cells, as measured by the simulated local field potential (LFP; see equation 4.11). The simulated LFP traces are shown in Figure 4.3A (panels below the spike histograms). The simulated LFP shows irregular oscillations for the condition in which the pyramidal cells do not receive shunting inhibition from the fast-spiking cells (Figure 4.3A, top panel). However, when the GABA-ergic projections from the FS-cells to the P-cells are active, the simulated LFP shows a regular oscillatory pattern (Figure 4.3A, bottom panel).

This effect is evident even more clearly from the LFP amplitude spectra (Figure 4.3B): the spectrum for the connected condition (red) shows a marked increase in gamma-band power over the unconnected condition (blue). In particular, a peak near 49 Hz can be observed. Note that this frequency is somewhat different from that reported for the interneuron-only simulations (previous section). This is because the net total input to the interneuron subnetwork was somewhat different for the present analyses (i.e., Poisson spike train input) than it was for the interneuron-only simulations (i.e., direct current input). The results presented in the previous section were based on a direct current input because that allowed a better comparison with the work of Vida et al. (2006).

To determine the amount of GABA-ergic shunting needed for the pyramidal cells to synchronize in a gamma rhythm, we systematically varied the average number of projections from the fast-spiking interneuron subnetwork to each pyramidal cell. The relative power in the gamma band (30–80Hz) of the simulated LFP steadily increased with the number of synapses, and reached a plateau at about ≥ 15 synapses per cell (Figure 4.3C, top panel). The network remained in an unsynchronized state for up to ≤ 7 synapses per cell, and network synchronization increased steadily above this threshold (Figure 4.3C, bottom panel).

The continuity in rise of the relative gamma power with respect to the number of synapses, when contrasted with the initial zero-valued plateau that was observed for the synchronization, is explained by the fact that the LFP is primarily a measure of post-synaptic potentials (PSPs). For a small, but non-zero connection strength between a network with synchronized firing at a gamma frequency (i.e., the FS cells) that projects to another network of cells (i.e., the P-cells), the PSPs will also oscillate, albeit with a small amplitude, in the gamma frequency range. If the oscillatory PSP activity is small and subthreshold, the oscillatory input may not be reflected in the spiking activity and, consequently, not be observed as network synchronization, unless the synchronized PSPs are sufficiently strong relative to the cells' firing threshold.

4.3.3 Theta modulation of spike times

To investigate the influence of ascending hippocampal fibres, carrying a theta rhythm, on the spike times of neocortical fast-spiking and pyramidal cells, we supplied our model network with variable-rate Poisson spike trains, in addition to the constant-rate background input already present. These 'theta fibres' varied their firing frequency according to a sinusoid oscillating at a theta frequency of $f_\theta = 4\,\text{Hz}$ (see equation 4.7; this particular frequency was chosen to correspond to observed theta frequencies in anaesthetized rats (Sirota et al., 2008). Note that we will use the term 'theta fibres' to refer to the projections from the theta-modulated Poisson spike trains to the cells of our model network. We do not wish to imply that there are anatomically identifiable fibres running from the hippocampus to the neocortex that are dedicated exclusively to the propagation of the theta rhythm.). Each fast-spiking cell received, on average, 20 incoming synapses from these variable-rate fibres, while each pyramidal cell received, on average, 10.

An analysis of the spike times of the fast-spiking and pyramidal cells revealed that the number of spikes (in 25 ms bins) occurring at the peak of the theta rhythm is larger than the number of spikes occurring at the theta trough (Figure 4.4A). This finding holds for both cell populations, and is easily explained by noting that the total net excitation experienced by a cell is higher during a theta peak than during a theta trough. (The role of 'coincidence detection'-like phenomena in the increased number of spikes during theta peaks is probably negligible; the P cell membrane time constant is around $6 - 7\,\text{ms}$.) Furthermore, theta modulation of spike times increases with increasing theta input amplitudes (Figure 4.4B).

Differential modulation of pyramidal and fast-spiking cells The theta modulation of pyramidal cells was much stronger than that of the fast-spiking cells (Figure 4.4A and B). This finding is remarkable, since the fast-spiking cells receive, on average, twice as many incoming theta-modulated synapses as the pyramidal cells (20 vs. 10), and even four times as many when the ratio of theta-modulated to constant-rate fibres is taken into account (FS: 20/50; P: 10/100). The resulting differential theta-modulation is in accordance with physiological findings: Sirota et al. (2008) found that, in rats, the spike times of neocortical

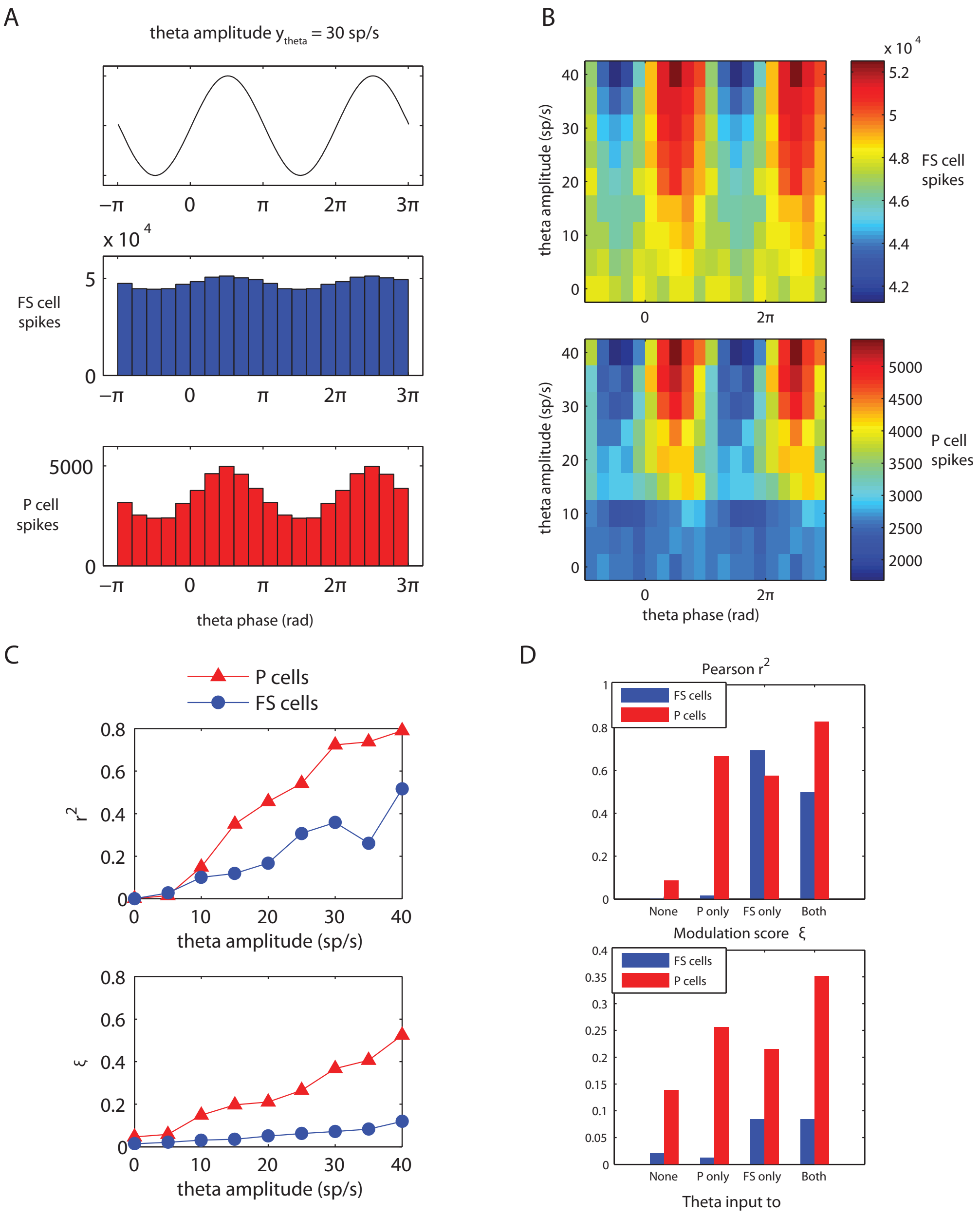

FIGURE 4.4: Theta modulation of fast-spiking and pyramidal cell spike times. Fast-spiking cells received, on average, twice as many theta-modulated input synapses as the pyramidal cells, which, relative to the total input, is four times as many (see main text for details). (Figure legend continued on next page.)

/hlpyramidal cells are more strongly biased by the hippocampal theta rhythm than the spike times of neocortical fast-spiking interneurons.

In order to quantify this difference, we computed two measures of theta modulation: Pearson's correlation coefficient r^2, computed between the raw theta signal and the aggregated spike histograms; and our modulation score ξ, as described by equation 4.14. Indeed, plots of these measures confirm that the theta modulation of the pyramidal cells is consistently larger than that of the fast-spiking cells (Figure 4.4C). For a theta modulation amplitude of y_θ = 30 sp/s, the parameter setting used for Figure 4.4A, the relevant values were $r^2_{\mathrm{FS}} = 0.358$; $r^2_{\mathrm{P}} = 0.724$; $\xi_{\mathrm{FS}} = 0.072$; $\xi_{\mathrm{P}} = 0.367$.

To find an explanation for the much stronger theta-modulation of spike activity of the P cells, when compared to the FS cells, we investigated the firing characteristics of both of our subnetworks in response to different levels of Poisson spike train input arriving at a single cell. Results for this simulation are shown in Figure 4.5. The FS cells show a reasonably flat response to increasing input after an initial strong rise, whereas the P cells show a very steep, exponential response. Given the mean theta input fibre spike rate of 40 sp/s, for a theta input amplitude of $y_\theta = 30$ sp/s, the spike rate of the theta-modulated input fibres varies between $A_{\theta,\mathrm{trough}} = 40 - 30 = 10$ sp/s and $A_{\theta,\mathrm{peak}} = 40 + 30 = 70$ sp/s. Consequently, the total input (the sum of the constant-rate input and the theta-modulated input) experienced, on average, by a single FS cell varies between $50 \cdot 40 + 20 \cdot 10 = 2\,200$ and $50 \cdot 40 + 20 \cdot 70 = 3\,400$ sp/s. The average total input to a single P cell varies between $100 \cdot 40 + 10 \cdot 10 = 4\,100$ and $100 \cdot 40 + 10 \cdot 70 = 4\,700$ sp/s. These values correspond to the vertical lines in Figure 4.5. Notice the relatively much larger y-axis range corresponding to these input values for the P cells, when compared to the FS cells. This explains why the theta-modulation of P

FIGURE 4.4: (continued) **(A)** Spike histograms for the fast-spiking (blue, middle) and pyramidal (red, bottom) cells relative to theta phase. The amplitude of the incoming theta rhythm was set to y_θ = 30 sp/s (see equation 4.7). Histogram bin size is 25 ms. Above the spike histograms, the 'raw theta signal' (see equation 4.13) is plotted, to show which phases in the theta cycle correspond to peaks and troughs. **(B)** Spike counts (color code) relative to theta phase (x-axis) for the fast-spiking (top) and pyramidal (bottom) cells as a function of theta amplitude y_θ (y-axis). Spike count bin size is 25 ms and bins were non-overlapping. **(C)** Two different measures of theta modulation of spike times: Pearson's r^2 (top) and relative modulation amplitude ξ (bottom; see equation 4.14) as a function of incoming theta amplitude y_θ. **(D)** The same two measures as a function of theta input distribution.

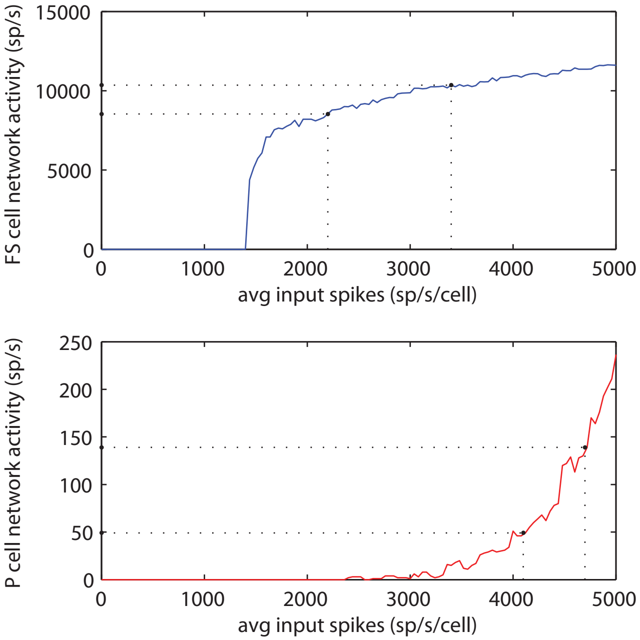

Figure 4.5: Frequency/input curves for the two model subnetworks: the fast-spiking cells (top) and the pyramidal cells (bottom). The dotted lines perpendicular to the x-axis represent the total range of spike train input experienced by the subnetworks due to the theta-modulated input fibres. Dotted lines perpendicular to the y-axis represent the resulting subnetwork spike activity. While the theta-modulation of input spikes is stronger for the FS cells than for the P cells, the resulting difference in subnetwork spike activity is greater for the P cells, as can be observed from the intersection of the horizontal lines with the y-axis.

cell activity is so strong, even though the FS cells receive a much more strongly theta-modulated input.

Effect of theta input to different subnetworks In the above-mentioned simulations and analyses, theta-modulated input, when present, was always presented to both subnetworks of P and FS cells of our model network. We also investigated the effect of theta-modulated input to each of the subnetworks separately.

To assess the amount of theta-modulation present in the spike times of the FS and P cell subnetworks, we computed two measures sensitive to this modulation (see Methods). Figure 4.4D shows the results for these simulations. The spiking activity of the pyramidal cells is theta-modulated when either (or both) of the two subnetworks receives theta-modulated input. The spiking activity of the fast-spiking cells, however, is only theta-modulated when they directly receive theta-modulated input, irrespective of whether the pyramidal cells receive theta-modulated input or not.

This finding can be explained by looking at the input response curves for the two subnetworks (Figure 4.5): (1) the FS cells show a flat input response curve, thereby requiring a large change in input to obtain a small change in activity, and (2) the overall spiking activity of the P cells is very small, when compared to the FS cells or the input spike trains. When only the P cell subnetwork receives theta-modulated input, this will be reflected in the spiking activity of this subnetwork (see Figure 4.4D). The P cell subnetwork activity is still very low, however, when compared to the total input to a single FS cell, coming from other FS cells and input spike trains. Therefore, the theta-modulated P cell activity will not have a large enough impact on the FS cells to be noticeable in their spiking activity.

4.3.4 Theta modulation of LFP gamma activity

In the previous section we demonstrated that the spiking activity of the pyramidal and fast-spiking cells is theta-modulated when these subnetworks are presented with theta-modulated input spike trains. Additionally, we showed that pyramidal cell activity is theta-modulated if either the pyramidal cells or the fast-spiking cells receive theta-modulated input, while fast-spiking cell activity is only theta-modulated when they directly receive theta-modulated input.

This raises the following two interrelated questions. First, is the LFP gamma activity, caused by the FS cell shunting inhibitory synapses on the P cells, also theta-modulated? And second, if a theta/gamma coupling exists, which theta-modulated input fibre projections are necessary and, therefore, presumably responsible, for this coupling?

Gamma frequency modulation by theta phase To answer these questions, we computed simulated LFP from our model network in four different conditions: no theta input, theta input only to the P cells, theta input only to the FS cells, or theta input to both subnetworks. Time-frequency representations for 1 s of these recordings are shown in Figure 4.6A. In all four conditions the spectral power peaks in the gamma range near 50 Hz.

To determine whether a phase/frequency coupling between the incoming theta signal and the gamma LFP occurred in our network, we plotted the highest-

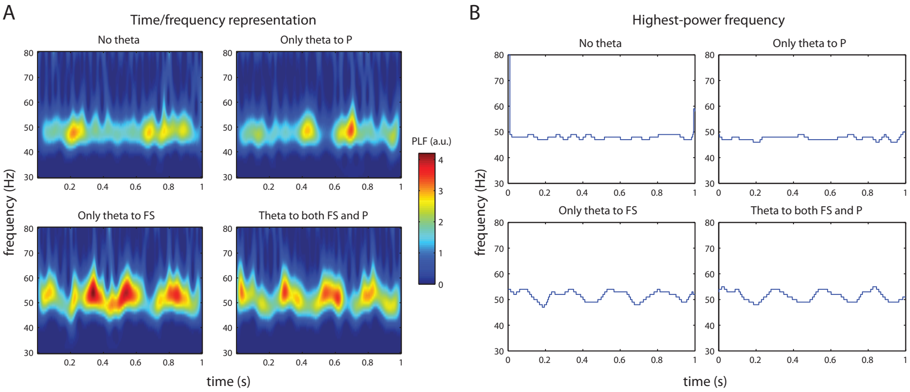

FIGURE 4.6: Effect of theta-modulated input on LFP gamma frequency. **(A)** Time-frequency representations of one second of simulated LFP activity. The four panels correspond to theta-modulated input fibres projecting to different parts of the model network. **(B)** The frequency within the gamma band with the highest power, for the same data segments shown in A. Theta phase/gamma frequency coupling is observed if and only if the FS cells receive theta-modulated input.

power frequency from the above-mentioned time-frequency representations as a function of time (Figure 4.6B). These plots show that the highest-power gamma frequency varied with the theta rhythm only when the FS cells received theta-modulated input. Variation in the peak gamma frequency as a function of theta phase thus requires projections from the simulated hippocampal afferent fibres to the FS cells.

Gamma amplitude modulation by theta phase To determine whether the gamma amplitude is modulated by theta phase, we computed a composite theta phase/gamma amplitude signal $z(t)$. Theta phase is, by construction, distributed uniformly, since the theta rhythm is generated by a simple sine function. Therefore, clustering of $z(t)$ in the complex plane (resulting in a radially asymmetric distribution around the origin) is an indication of phase/amplitude coupling (Canolty et al., 2006) (see Methods for details). Distributions of $z(t)$, for each of the four theta input conditions, are shown in Figure 4.7A. $z(t)$ is distributed uniformly with respect to theta phase when only the P cells receive theta-modulated input. However, when the FS cells receive theta-modulated input, the distribution is clearly non-uniform.

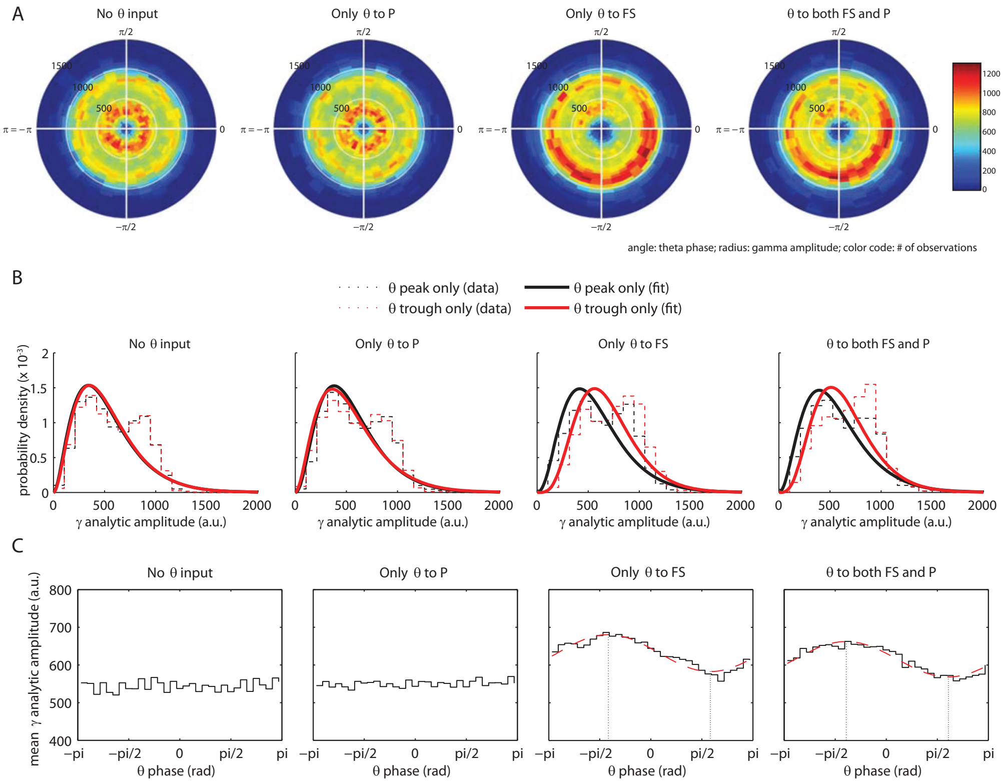

FIGURE 4.7: Effect of theta-modulated input on LFP gamma amplitude. **(A)** The distribution of a composite theta phase/gamma amplitude signal $z(t)$ in the complex plane. Color code represents the number of observations; angle corresponds to theta phase (divided into 32 equally-sized bins); radius corresponds to gamma amplitude (divided into 32 equally-sized bins). **(B)** Histograms of gamma amplitudes occurring in $\frac{2\pi}{32}$ wide phase bins centered at the peak of the theta rhythm ($\varphi_\theta = \frac{\pi}{2}$; black) and at the trough ($\varphi_\theta = -\frac{\pi}{2}$; red). Dashed lines correspond to the observed data histograms; solid lines represent the best-fit gamma distribution for this data. When FS cells receive theta-modulated input, the best-fit distribution for the theta trough is shifted to the right, compared to the distribution for the theta peak (parameter differences are significant, $p < 0.0001$). **(C)** Mean gamma amplitude as a function of theta phase. For the two rightmost plots, the best-fit sine functions are shown by a dashed red line. Gamma amplitudes are higher at the trough than at the peak of the theta rhythm, and the lowest and highest gamma amplitudes (indicated by dotted vertical lines) occur somewhat after the theta peak and trough, respectively.

To get a more detailed view of the nature of theta phase/gamma amplitude coupling, we investigated the distribution of gamma amplitudes a_γ at just the peaks and troughs of the theta rhythm (the phase relates to the sine phase, so a peak is at $\varphi_\theta = \frac{\pi}{2}$ and a trough is at $\varphi_\theta = -\frac{\pi}{2}$). Figure 4.7B shows these distributions for each of the four theta input conditions. Note that the data histograms in Figure 4.7B do not directly correspond to a single 'arm' of the polar phase/amplitude histograms shown in Figure 4.7A. To obtain the distributions most accurately corresponding to the two theta extremes, bins for 4.7B were *centered* at either the theta peak or trough, while the theta peak and trough correspond to a bin *edge* for 4.7A. The solid lines in this figure correspond to the best-fit gamma distributions of gamma amplitudes for the theta trough (red) and the theta peak (black). We used gamma distribution fits for our amplitude data because we wanted to be able to compare our results with Canolty et al. (Canolty et al., 2006). The distribution we observed, however, seems to correspond more to a bimodal distribution (also visible as two concentric rings of higher distribution density in all four plots of Figure 4.7A). The best-fit distribution is shifted to the right, compared to the distribution for the theta peak, when the FS cells receive theta-modulated input. The differences between the distribution parameters are significant ($p < 0.0001$). This indicates that gamma amplitude is higher at the theta trough than at the theta peak; a finding that is in agreement with physiological findings in humans (Canolty et al., 2006).

Finally, to get a quick 'bird's eye' view of the coupling between theta phase and gamma amplitude, we divided theta phase into 32 bins and computed the mean gamma amplitude for each of these bins. Plots of these data (Figure 4.7C) clearly show that, when the FS cells receive theta-modulated input, gamma amplitudes are higher at the trough than at the peak of the theta rhythm. The lowest and highest gamma amplitudes occur somewhat after the theta peak and trough, respectively. More specifically, the extremes in gamma amplitudes lag behind the (opposite) theta extremes by 0.26 rad (for the FS only condition) or 0.34 rad (for the FS+P condition). These values correspond to delays of 10.36 and 13.54 ms.

4.3.5 Robustness of core results to various model parameters

So far, we have used a fixed theta frequency of $f_\theta = 4$ Hz throughout this chapter, which is on the low end of the frequency range usually associated with theta oscillations (see, e.g., (Kahana et al., 2001)). To determine whether the results

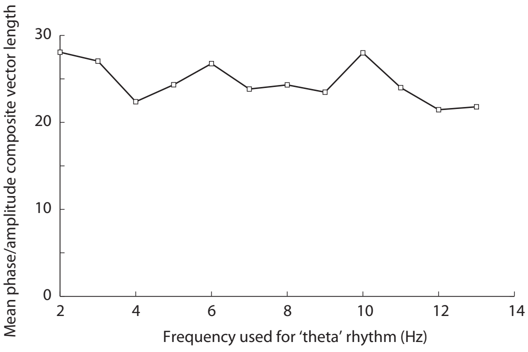

FIGURE 4.8: Phase-amplitude coupling as a function of the phase-providing frequency.

we obtain are specific to 4 Hz, or whether they generalize to other theta-range frequencies, we systematically varied the frequency f_θ between 2 and 13 Hz and repeated our phase/amplitude analysis based on the composite signal $z(t)$. We quantified the phase-amplitude distribution $z(t)$ this by computing $\|\overline{z(t)}\|$, i.e., the norm of the mean of all composite phase/amplitude values. We examined whether this value depended on the frequency of the theta input (Figure 4.8). Although we observed a correlation trend between these two variables ($r^2 = 0.2893$), this trend did not reach significance ($p = 0.07$). We conclude that our main finding does not crucially depend on theta frequency.

Electrophysiological data suggests that the projections from the hippocampus to neocortical networks are stronger to interneurons than to pyramidal cells (Tierney et al., 2004; Gabbott et al., 2002). We incorporated this difference into our model by supplying the FS cells with a more strongly theta-modulated input than the P cells, yielding the results described above. We highlighted the crucial role the FS cells play in the coupling between the theta and gamma rhythms. An additional simulation, in which we switched the two theta-modulated input strengths (i.e., in which the input to the P cells was more strongly theta-modulated than the input to the FS cells), resulted in the same outcome: a coupling between the theta and gamma rhythms only occurred in the two conditions in which the FS cells received theta-modulated input (results not shown). Therefore, the crucial role played by the FS cells is not dependent on them receiving more strongly theta-modulated input than the P cells.

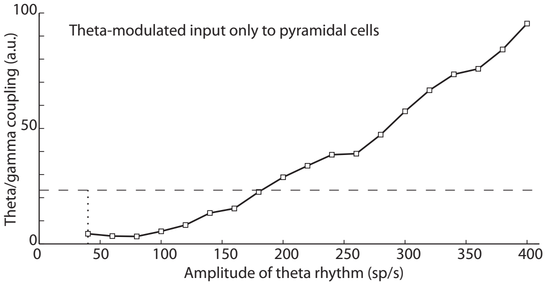

FIGURE 4.9: Phase-amplitude coupling when only the pyramidal cells receive theta-modulated input.

This, of course, prompted the question: what amplitude of theta modulated input *would* drive the P cell gamma activity to become theta modulated, in the total absence of theta input to the FS cells? To gain insight into this question, we disconnected all theta fibres from the FS cells, while making no other changes to the model (so FS to P synapses were intact, etc.). We varied the mean spike rate of the theta input fibres between A_θ = 40 sp/s and A_θ = 400 sp/s, while the amplitude of the modulation was set to $y_\theta = A_\theta - 10$ sp/s, so we simultaneously varied both the average spike rate of the theta fibres and its modulation strength. We analyzed theta/gamma phase-amplitude coupling again by computing the mean of $z(t)$, as described above. Results for this analysis are shown in Figure 4.9; the dashed horizontal line indicates the value of the plotted coupling metric for the physiologically constrained parameters used in the original simulations described in the bulk of this chapter (this parameter value is indicated by the dotted vertical line). It can clearly be seen that the amount of theta modulation required for theta/gamma coupling, when only the P cells receive theta input, is much higher than when the FS cells receive theta input as well. Specifically, coupling comparable to the results described above (obtained with A_θ = 40 sp/s, y_θ = 30 sp/s, modulation of 75% of mean) is only observed with the very high values A_θ = 160 sp/s and y_θ = 150 sp/s (modulation of 94% of mean) or above, when theta input is restricted to the P cells only.

A further interesting factor to investigate is to what extent does the observed theta/gamma coupling depend on the gamma synchronization of the FS cells? Since we found that gamma synchronization cruciallly depends on the value of the GABA-ergic synaptic reversal potential E_{GABA}, we varied this parameter

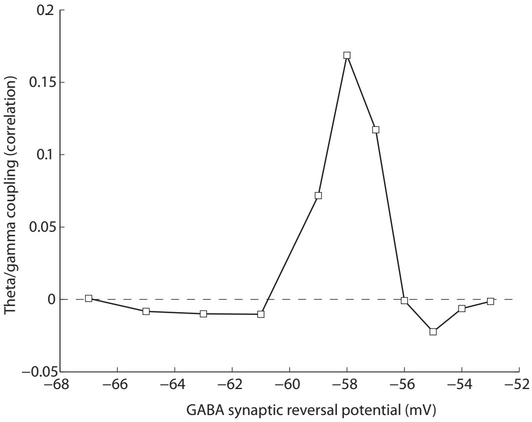

Figure 4.10: Phase-amplitude coupling as a function of GABA-ergic synaptic reversal potential.

to investigate this question. We computed, for various values of this parameter, the correlation between the sinusoidal theta rhythm used as input to the model network, and the amplitude envelope of the gamma-filtered LFP. (Note that this correlation measure is somewhat different from the mean composite phase/amplitude vector length we report above. We use a correlation here instead because binning the gamma amplitude values is not well-defined when gamma synchrony is very low.) Results for this analysis are shown in Figure 4.10. Evident from this plot is a clear regime between about −60 and −57 mV where theta/gamma coupling occurs, whereas for both lower and higher GABA reversal potentials, the coupling is absent. These values of E_{GABA} correspond well to the values which were found to lead to the greatest robustness in gamma synchronization of the FS cells (see Figure 4.2 and earlier in Results).

Finally, we note that our choice of simulated LFP potential is not trivial. Often, the sum of synaptic transmembrane currents is used to model the LFP. The LFP indeed mainly depends on postsynaptic currents, but it is mainly the low-frequency components of these currents that determine the extracellulary measured LFP (Pettersen et al., 2012). In effect, the extracellular medium acts as a rather complex low-pass filter. While attempts have been made at accurately computing the LFP, taking this into account (Pettersen et al., 2012; Bédard et al., 2004), we decided to use the summed membrane *potential* as a simple proxy instead. The temporal profile of the membrane potential is also low-pass filtered when compared to the transmembrane currents, due to the conductance properties of the membrane. Of course, it is important to ensure that our core results do not qualitatively depend on the choice of our simulated LFP signal. Therefore, we conducted a control analysis in which we investigated the effect of the choice of simulated LFP on our results. We found that the phase/amplitude distribution is quite a bit sharper when considering currents instead of potential (not shown in figures). This is expected, because the 'smearing' properties of the membrane potential are not incorporated when using transmembrane current. Crucially, however, the main features of the distribution remain the same: a clustering is observed for gamma amplitude as a function of theta phase.

4.4 Discussion

We have put forward a biophysical conductance-based neural network model, composed of fast-spiking (FS) and pyramidal (P) cells, that displays robust gamma oscillations. When supplied with hippocampal theta-modulated input fibres, the network shows spike activity that is biased by the theta rhythm. Furthermore, both the frequency and amplitude of the local field potential (LFP) gamma oscillations are modulated by the phase of the theta rhythm. Importantly, this latter phenomenon *only* occurs when the FS cells directly receive hippocampal theta-modulated input, highlighting the crucial role these cells play in the interplay between neocortex and hippocampus.

The conductance-based neuron models we used in our study provide the most realistic approximation of actual single-neuron activity (Izhikevich, 2004) to date. This is in sharp contrast to integrate-and-fire neurons, which can be simulated far more quickly, but provide a much rougher approximation of neural activity (Izhikevich, 2004). Cross-frequency coupling of neuronal oscillations has been analysed with biophysical model neurons before, mainly in relation to network firing rate. Mazzoni et al. (2010), for instance, find a significant coupling between delta phase and gamma amplitude, for network parameters quite similar to the ones we used in the present study. Crucially, previous work on this topic has generally used integrate-and-fire neurons, whereas we show cross-frequency phase/amplitude coupling for the—to our knowledge—first time using a conductance-based model for all simulated neurons.

4.4.1 Gamma synchronization and oscillations

When studied in isolation, our subnetwork of FS cells, coupled with fast inhibitory synapses and gap junctions, shows synchronized activity at a gamma frequency (Figure 4.2). For GABA-ergic synapses with a hyperpolarizing reversal potential, this synchronization quickly dissipates with increasing heterogeneity of the input drive. For shunting reversal potentials, however, the network remains robustly synchronized for relatively high levels of drive heterogeneity. This finding is a replication of earlier work (Vida et al., 2006; Bartos et al., 2007).

The optimally robust synaptic reversal potential for the gamma synchronization of the FS cells was dependent upon mean input drive (Figure 4.2D). For increasing input currents, the optimal reversal potential shifts towards more negative values, but remains well above the membrane potential at rest. This phenomenon likely reflects the important role of strong mutual inhibition between the FS cells in the generation of the gamma rhythm (Wang & Buzsáki, 1996). When the input current is strong, the FS cells become strongly excited, and the inhibition balancing this excitation may not be strong enough when the synaptic reversal potential is relatively high. This might allow some cells to fire out of phase with the gamma rhythm. Lower synaptic reversal potentials, on the other hand, result in sufficiently strong inhibition to silence out any 'rogue' cells during the interval between population spike peaks.

The FS cells proved effective in imposing their synchronized rhythm on a population of P cells (Figure 4.3). When the FS cell subnetwork was coupled to the P cell subnetwork, the LFP quickly became dominated by the GABA-ergic post-synaptic potentials caused by the FS cells' spiking activity. This resulted in an increase in LFP power in the gamma band and in an increased synchronization of the P cells' spike times. Thus, gamma oscillations in our inhibitory interneuron subnetwork carry over to the pyramidal cells to which it was coupled. This fits nicely with prominent theories on the role of the gamma rhythm as a fundamental computational mechanism (Fries et al., 2007), in which the amplitude of input to a pyramidal cell network can be transformed into a phase code. This transformation is achieved through a coupling of the network to fast-spiking interneurons network which are firing in a gamma rhythm (Fries et al., 2007).

In *in vivo* recordings of cortical LFP, the power spectrum is usually characterized by a very dominant $1/f$ or 'power law' component (Baranauskas et al., 2012). We do not show such a power law scaling in the spectra computed for our model (Figures 4.2C, 4.3B, 4.6A), which is not in line with these *in vivo* findings. However, the power law scaling of LFP power is usually absent from *in vitro* recordings (e.g. Buhl et al., 1998; Cunningham et al., 2003; Gloveli et al., 2005). Therefore, the involvement of large-scale dynamic interactions with the rest of the brain seems essential for the power law scaling to be apparent. Since model studies typically simulate a small patch of cortex, their object of study is much more similar to *in vitro* than to *in vivo* recordings. This is also the case for our study, so the lack of a dominant $1/f$ component is expected for our power spectra.

4.4.2 Effect of theta-modulated input

When the network received not only constant-rate input, but also input from theta-modulated hippocampal afferent fibres, its spiking activity was modulated by the theta rhythm (Figure 4.4). This is in accordance with empirical findings (Sirota et al., 2008; Siapas et al., 2005; Sirota et al., 2003).

Theta-modulated input to our model network also had an effect on the gamma oscillations visible in the LFP. Both the frequency (Figure 4.6) and the amplitude (Figure 4.7) of the gamma oscillations were modulated by the phase of the theta rhythm, but only when the FS cells directly received a theta-modulated input. Theta/gamma coupling was completely absent, both regarding frequency and amplitude, when only the P cells received theta-modulated input, even though the P cells' spiking activity *was* theta-modulated in this condition. This can be explained by the fact that the gamma rhythm is generated by the FS cells and imposed upon the P cell subnetwork by these cells. It follows easily that, when the activity of the FS cells is not theta-modulated, the gamma rhythm, as observed in the LFP, is not theta-modulated either. An exception to this rule was only observed when theta-modulated input to the P cells was much higher than would be physiologically plausible (Figure 4.9).

The frequency of the gamma rhythm was higher during the peak of the theta rhythm than during the trough (Figure 4.6). The gamma rhythm is generated by the FS cells. During the theta peaks these experience a stronger net total input and, therefore, increase their firing rate while remaining synchronized, hence resulting in a higher frequency of the corresponding gamma oscillations. We do not know of any empirical reports on a coupling between hippocampal theta phase and neocortical peak gamma *frequency* (as opposed to gamma amplitude), but this is an interesting prediction that can be tested.

The amplitude of the LFP gamma oscillations was also influenced by the phase of the incoming theta rhythm (Figure 4.7). Gamma amplitude was higher during the trough than during the peak of the theta rhythm, a phenomenon that was also reported for human subjects (Canolty et al., 2006). The highest gamma amplitude occurred somewhat after the theta trough and the lowest gamma amplitude occurred somewhat after the theta peak.

The mechanisms by which the amplitude of gamma oscillations is actually *highest* during the periods of *least* net total input to the network are not entirely clear to us. Canolty et al. (Canolty et al., 2006) found a similar phase/amplitude coupling between the theta and gamma rhythms, in the human neocortex. As to the mechanism of this coupling, they hypothesize that "basal forebrain cortical-projecting GABAergic neurons (…) preferentially synapse onto intracortical GABAergic neurons (…), with disinhibitory spike bursts causing a brief increase in gamma power at the theta trough" (Canolty et al., 2006, p. 1628).

While the basal forebrain (BF) GABA-ergic neurons probably play a role in the modulation of neocortical networks (Lin et al., 2006), our results suggest that they are not responsible for the coupling between theta phase and gamma amplitude. We were able to reproduce such a coupling using only *excitatory* (glutamatergic) fibres to carry the theta rhythm. Of course, this does not directly preclude the alternative hypothesis (i.e., the BF GABA-ergic neurons playing the crucial role), but we believe this alternative to be unlikely for the following reason. The gamma oscillations visible in the EEG and LFP are mainly due to post-synaptic potentials in the pyramidal cells resulting from spike events in intracortical GABA-ergic fast-spiking cells. If the latter cells receive inhibition (e.g., from BF GABA-ergic neurons), the result would be a *weakening* of the gamma oscillations, and not an increase in amplitude. Therefore, we believe that excitatory, rather than inhibitory, projections to the FS cells are responsible for the modulation of gamma amplitude by theta phase.

4.4.3 Functional role of cross-frequency coupling

Between- and within-region coupling between neuronal oscillations of different frequencies, in particular between the phase of a lower-frequency oscillation and the amplitude of a higher-frequency one, has been observed in rodents (Sirota et al., 2008; Siapas et al., 2005; Sirota et al., 2003), macaque monkeys (Chapter 3, Lakatos et al., 2005), and humans (Canolty et al., 2006; Axmacher et al., 2010; Voytek et al., 2010b). This type of cross-frequency coupling is thought to play an important role in the integration of the various timescales at which the brain processes information: large-scale dynamical brain networks, reflected in lower-frequency oscillations, entrain high-frequency local neuronal computations, thereby enabling various brain regions to process the incoming information in the most efficient and task-relevant manner (Canolty & Knight, 2010).

It has recently been suggested that cross-frequency coupling between the alpha (8–12 Hz) and gamma bands could implement a mechanism of pulsed inhibition by which salient stimuli are given priority over less salient ones (Chapter 3, Jensen et al., 2012). This suggestion was inspired by evidence that the phase of alpha oscillations modulates both perception (Chapter 2, Mathewson et al., 2009; N. Busch et al., 2009) and gamma amplitude (Chapter 3, Osipova et al., 2008; Voytek et al., 2010b). Alpha activity likely serves to inhibit brain regions that are irrelevant to the behaviour at hand; e.g. to inhibit parts of visual cortex that correspond to non-attended parts of the visual field (Händel et al., 2011). To still enable processing of important stimuli in those non-attended parts of the environment, by those inhibited brain regions, alpha activity creates a temporal code that serves to order the stimuli according to saliency. The actual processing itself is reflected in the gamma band, thus resulting in coupling between the phase of alpha and the amplitude of gamma (Jensen et al., 2012).

While the present chapter is mainly concerned with coupling between hippocampal theta and neocortical gamma oscillations, it seems equally applicable to such coupling within the neocortex between the alpha and gamma bands. The core findings of our model are upheld when we change the low-frequency signal from the theta to the alpha band, as shown in Figure 4.8. This is particularly interesting considering the crucial role we find for inhibitory cells in our model: the cross-frequency relation between alpha and gamma in humans is hypothesized to fulfill a temporal code in which local inhibition of brain regions is crucial. A mechanism of low-frequency modulation of gamma oscillations very similar to the one we explore here might thus elegantly explain the ordering and inhibition of stimuli according to saliency as well. Of course, further work is needed to determine to what extent this speculation holds.

In conclusion, our model demonstrates that the empirically observed coupling between the hippocampal theta and neocortical gamma rhythms crucially involves a neocortically local network of fast-spiking interneurons. Thus, our findings shed light on the mechanism behind large-scale cortical interactions responsible for an ‘oscillatory hierarchy’ of neuronal information processing (Lakatos et al., 2005; Fries et al., 2007). The crucial role of fast-spiking interneurons in cross-region phase/amplitude coupling is, we believe, an interesting and testable prediction of our model.

4.5 Methods

All network simulations were conducted using version 7.1 of the NEURON simulation environment (Hines & Carnevale, 1997), released on January 15th, 2009. All data analyses were conducted using custom scripts, written either for NEURON 7.1, or for MATLAB (Mathworks Inc., Natick, MA, USA).

4.5.1 Interneuron subnetwork

The interneuron subnetwork was modelled after some quite extensive previous neurophysiological and modelling work (Bartos et al., 2002, 2007), and consists of a virtual ring of 200 single-compartmental Hodgkin-Huxley-like model neurons (Hodgkin & Huxley, 1952). We used this ring-like structure because we use a synaptic connection probability that is dependent on cell distance (described in more detail below): if we had just used an unfolded one-dimensional line, cells at the edges of the line would have fewer synaptic connections than cells near the middle of the line. Using a ring avoids this problem (Bartos et al., 2002, 2007).

Cells had a resting potential of $E_{\text{rest}} = -65$ mV and a membrane surface area of 100 μm^2. Leakage, Na^+, and K^+ conductances were inserted into each neuron according to the model of Wang & Buzsáki (Wang & Buzsáki, 1996; 'WB' conductances). These differ from standard Hodgkin-Huxley ('HH') conductances in two important respects: first, the fast Na^+ current activation variable m is substituted by its steady-state value m_∞; second, the remaining gating kinetics for the Na^+ and K^+ current are sped up by a factor $\phi = 5$. These specifics are computationally efficient, because of the $m = m_\infty$ substitution, and, because of the adjusted time course of the currents, ensure that a firing pattern emerges that is characteristic of fast-spiking inhibitory interneurons (Wang & Buzsáki, 1996).

Each interneuron receives incoming GABA-ergic synapses from a subset of its neighbours on the ring with a Gaussian probability dependent upon the distance between two cells, up to a maximum connection distance of 50 cells ($3\sigma = 50$). Synapses were either on or off; the Gaussian probability only governs whether or not there will be a synapse and is not used to determine synaptic strength.

Synaptic events were modelled by insertion of a conductance determined by a two-state kinetic scheme of the form:

$$g_{\text{syn}}(t) = \bar{g}_{\text{syn}} N \left(e^{-\frac{t}{\tau_d}} - e^{-\frac{t}{\tau_r}} \right) \tag{4.1}$$

with resulting current:

$$I_{\text{syn}}(t) = g_{\text{syn}}(t)(V(t) - E_{\text{syn}}) \tag{4.2}$$

where $\bar{g}_{\text{syn}}$ is the maximum synaptic conductance, E_{syn} is the synapse reversal potential, and N is a normalization factor:

$$N = \frac{1}{\exp\left(-\frac{\tau_r}{\tau_d - \tau_r} \ln\left(\frac{\tau_d}{\tau_r}\right)\right) - \exp\left(-\frac{\tau_d}{\tau_d - \tau_r} \ln\left(\frac{\tau_d}{\tau_r}\right)\right)} \tag{4.3}$$

that ensures that the peak conductance is given by the relevant parameter $\bar{g}_{\text{syn}}$.

The GABA-ergic synapses were governed by a rise time constant $\tau_{\text{GABA,rise}} = 0.16\,\text{ms}$ and a decay time constant of $\tau_{\text{GABA,decay}} = 1.8\,\text{ms}$. The unitary post-synaptic peak conductance was $\bar{g}_{\text{GABA}} = 0.1\,\text{mS cm}^{-2}$. These values are consistent with empirical findings (Bartos et al., 2001; Buhl et al., 1995). The synaptic reversal potential was varied for the study of gamma rhythm generation, while it was set to $E_{\text{GABA}} = -57\,\text{mV}$ for all subsequent simulations, in accordance with gamma rhythm results and previous studies (Vida et al., 2006; Chance et al., 2002).

In addition to GABA-receptors, AMPA- and NMDA-receptors were also present at the membrane of the fast-spiking cells, in order to model the connections between the two subnetworks and to model incoming spike trains as input. These were modelled by conductance insertion according to two separate bi-exponential functions of the type described by equation 4.1. Separate time constants were used to model the AMPA and NMDA currents: $\tau_{\text{AMPA,rise}} = 0.5\,\text{ms}$, $\tau_{\text{AMPA,decay}} = 2.0\,\text{ms}$, $\tau_{\text{NMDA,rise}} = 3\,\text{ms}$, $\tau_{\text{NMDA,decay}} = 40\,\text{ms}$ (Kleppe & Robinson, 1999; Gabbiani et al., 1994). The reversal potential for both receptor types was set to $E_{\text{AMPA}} = E_{\text{NMDA}} = 0\,\text{mV}$. The unitary post-synaptic peak conductances for the glutamatergic synapses on the fast-spiking cells were given by $\bar{g}_{\text{AMPA}} = 0.5\,\mu\text{S cm}^{-2}$ and $\bar{g}_{\text{NMDA}} = 0.05\,\mu\text{S cm}^{-2}$. These conductance values were chosen to ensure that the average net current input to the fast-spiking cells, resulting from synaptic events, was comparable in amplitude to the direct current input used in the model of Vida and colleagues (Vida et al., 2006).

Apart from the above-mentioned chemical synapses, electrical synapses, or gap junctions, were included in the interneuron network. Gap junctions allow small quantities of ions to flow between two coupled cells; a given cell is thereby able to directly influence the membrane potential of another cell. Between each cell and its 8 nearest neighbours, a gap junction was inserted with a probability of 0.5, resulting in, on average, 4 gap junctions per cell (Vida et al., 2006).

Gap junctions were modelled by a constant conductance insertion of $g_{\text{gap}} = 10\,\text{pS}$ between two cells (Venance et al., 2000; Traub et al., 2001). The resulting current between two coupled cells i and j is given by

$$I_{\text{gap}} = g_{\text{gap}}(V_i - V_j) \tag{4.4}$$

4.5.2 Pyramidal cell subnetwork

The pyramidal cell subnetwork consists of a two-dimensional sheet of $30 \times 30 = 900$ single-compartmental Hodgkin-Huxley model neurons (standard NEURON implementation) (Hodgkin & Huxley, 1952; Hines & Carnevale, 1997). This results in an anatomically realistic ratio of $900/1100 = 82\%$ pyramidal cells versus $200/1100 = 18\%$ interneurons (Sirota et al., 2008). The resting potential of the pyramidal cells was equal to that of the interneurons, $E_{\text{rest}} = -65\,\text{mV}$, and standard Hodgkin-Huxley conductances were inserted to model cell membrane channels (Hodgkin & Huxley, 1952). Each neuron received glutamatergic synaptic afferents from a subset of its neighbours according to a two-dimensional Gaussian probability, dependent on cell distance. Maximum (Euclidean) connection distance was 8 cells ($3\sigma_x = 3\sigma_y = 8$), ensuring a realistic ratio of synaptic densities within the pyramidal cell subnetwork (see Table 4.1).

As with the interneuron subnetwork, here it is also important to avoid edge effects on the number of synapses per cell. For this two-dimensional case, we created a torus out of our network by folding opposing edges onto each other.

Incoming glutamatergic and GABA-ergic synaptic events were modelled by the same bi-exponential functions as described above for the fast-spiking cells (see equation 4.1), but with different peak conductances: for the pyramidal cells, $\bar{g}_{\text{AMPA}} = 3\,\mu\text{S cm}^{-2}$, $\bar{g}_{\text{NMDA}} = 0.4\,\mu\text{S cm}^{-2}$, and $\bar{g}_{\text{GABA}} = 0.05\,\text{mS cm}^{-2}$. These values were chosen to obtain accurate cortical pyramidal cell firing characteristics

	Model (%)	Anatomy (%)
FS→FS	4.24	1.34
P→FS	4.47	4.97
P→P	28.09	28.17
FS→P	6.30	7.62
ext→FS	7.09	6.66
ext→P	49.80	50.66

Table 4.1: Model connectivity values. Shown is the number of synapses of different types, presented as ratios of the total number of synapses. Model values were either chosen to reflect connectivity known from anatomy (reported anatomical values are from (Liley & Wright, 1994)), or, in the case of the FS→FS connectivity, based on previous modelling work (Vida et al., 2006).

for the model neurons; most importantly, they ensured an ongoing 'background firing noise' of about 1 – 2 sp/s (Hirase et al., 2001; Sirota et al., 2008).

4.5.3 Subnetwork interconnections and network input

For the investigation of theta–gamma coupling, each pyramidal cell received GABA-ergic afferents from, on average, 14 randomly chosen fast-spiking cells and each fast-spiking cell received glutamatergic afferents from, on average, 45 randomly chosen pyramidal cells. These values were chosen to obtain realistic ratios of synaptic densities between the two subnetworks (see Table 4.1). For the investigation of the influence of the gamma-synchronized interneuron subnetwork on the synchronization of the pyramidal cells, the average number of incoming P synapses per FS cell was kept constant at 45, while the average number of incoming FS synapses per P cell was varied in the range between 0 and 20.

For the investigation of gamma rhythm generation by the interneuron subnetwork, a direct current input was supplied to the fast-spiking cells. This allowed a straightforward comparison of our simulations with results found in the literature (Vida et al., 2006). The amplitude of the current was different for different cells, and varied as a function of time. This resulted in a variable intrinsic firing frequency for each fast-spiking cell, enabling the study of the robustness of network synchronization as a function of different parameters.

Specifically, drive amplitude was determined by drawing a mean drive μ_i for each cell $i \in \{1, 2, \dots, 200\}$ from a normal distribution with mean I_μ and then, for each time window of 1 ms, drawing a specific drive amplitude from a new normal distribution with mean μ_i:

$$\mu_i = \mathcal{N}(I_\mu, \sigma^2) \tag{4.5}$$

$$I_{\text{ext},i}(t) = \mathcal{N}(\mu_i, \sigma_i^2) \tag{4.6}$$

The spread of the distributions was defined in terms of coefficients of variation (CV), resulting in standard deviations $\sigma = CV_{\text{cells}} I_\mu$ and $\sigma_i = CV_{\text{time}} \mu_i$. The variation over time was kept constant, $CV_{\text{time}} = 10\%$, while both I_μ and CV_{cells} were varied to assess the network's robustness in generating a gamma rhythm.

To investigate (1) the influence of the gamma-synchronized interneuron subnetwork on the pyramidal cells and (2) the influence of the theta rhythm on the interconnected network of fast-spiking and pyramidal cells, direct current input was replaced by Poisson spike train input acting on glutamatergic synapses, to serve as a more realistic model of actual neuronal input.

Two pools of Poisson input spike trains were initialized, both consisting of 1 000 fibres. The fibres in the first pool had a constant average firing rate, $r_{\text{const}} = 40$ sp/s, modelling cortical background noise. The firing patterns of these fibres were mutually uncorrelated. The fibres in the second pool varied their spiking rate according to a sinusoid, modelling the ascending fibres that carry the theta rhythm. The average spiking rate for the 'variable-spiking' fibres is given by:

$$r_{\text{var}}(t) = A + y \sin(2\pi f_\theta t) \tag{4.7}$$

with average spiking rate $A = 40$ sp/s, amplitude $y = 30$ sp/s, and frequency $f_\theta = 4$ Hz. For each fibre in the two pools, the probability of a time window of $\Delta t = 1$ ms containing a single spike is given by $p_{\text{spike}} = r\Delta t \leq 0.07$.

Each pyramidal cell received incoming synapses from, on average, 100 randomly selected fibres with a constant firing rate and 10 randomly selected variable-spiking fibres, while each fast-spiking cell received incoming synapses from, on average, 50 randomly selected fibres with a constant firing rate and 20 randomly selected variable-spiking fibres. The strong projection from hippocampal afferents to interneurons, relative to pyramidal cells, is in accordance with previous morphological and physiological findings (Gabbott et al., 2002; Tierney et al., 2004; see table 4.1).

All of the synaptic densities reported above (i.e., concerning synapses within one of the two subnetworks, synapses between the two subnetworks, and external afferent synapses) were either chosen to reflect anatomically known ratios of different synaptic types ((Liley & Wright, 1994); see Table 4.1), or based on previous modelling work (Vida et al., 2006).

4.5.4 Network analyses and simulation characteristics

Assessment of network synchrony Two different measures were used to assess network synchrony. The first is the normalized averaged cross-correlation based 'network coherence' measure κ introduced by Wang & Buzsáki (Wang & Buzsáki, 1996). To determine this measure, two binary spike trains with bin size $\Delta t = 1$ ms and resulting length $L = \frac{T}{\Delta t}$ are given by $X(l) = 0$ or 1, $Y(l) = 0$ or 1, with 0 – no spikes and 1 – a spike present in time bin with index $l = 1, 2, \ldots, L$. The pairwise coherence between two spike trains X and Y is given by:

$$\kappa_{XY} = \frac{\sum_{l=1}^{L} X(l)Y(l)}{\sqrt{\sum_{i=1}^{L} X(i) \sum_{j=1}^{L} Y(j)}} \tag{4.8}$$

The network coherence measure κ is then defined as the average pairwise coherence for all neuron pairs in the network. Wang & Buzsáki (Wang & Buzsáki, 1996) define network coherence κ as a function of bin size and, indeed, this measure is quite strongly dependent upon bin size. Network synchrony is most accurately reflected by κ, however, when bin size is small. As a statistic, therefore, we report this measure only for a bin size of 1 ms, i.e., our $\kappa = \kappa(1)$. This is in accordance with previous work (Bartos et al., 2002).

As a second measure of network synchrony, we introduce the average spike volley peak height. To automatically determine the occurrence of a volley peak, all of the network's spikes are first aggregated in $\Delta t = 1$ ms bins, such that the number of spikes in the interval $[t - \Delta t, t)$ is given by $A(t)$ (time in ms). The occurrence of a peak is then defined as:

$$k(t) = \begin{cases} 1 & \text{if } A'(t - \Delta t) > 0, \\ & \text{and } A'(t) < 0, \\ & \text{and } A(t) \geq A_{\text{thr}} \\ 0 & \text{otherwise.} \end{cases} \tag{4.9}$$

where $A_{\text{thr}} = \frac{1}{10} N_{\text{FScells}}$ for the fast-spiking cells and $A_{\text{thr}} = \frac{1}{200} N_{\text{Pcells}}$ for the pyramidal cells. The discrete derivative $A'(t) = \frac{A(t+\Delta t)-A(t)}{\Delta t}$. The average spike volley peak height is given by:

$$\lambda = \frac{\sum_{t=t_0}^{t_{\text{stop}}} k(t)A(t)}{\sum_{t=t_0}^{t_{\text{stop}}} k(t)} \tag{4.10}$$

with t_0 and t_{stop} the begin and end times (in ms) of the simulation period to be analyzed, respectively.

Simulation timings It is important to ensure that a truly (pseudo-)random firing pattern will emerge in the network, so that no initialization effects will influence the results. Therefore, at the beginning of a network simulation, at $t = -400$ ms, no synaptic connections are inserted, within or between the two subnetworks. At $t = -200$ ms, synapses and gap junctions are inserted, and all analyses of network firing characteristics are started at $t = t_0 = 0$ ms, allowing the network to settle into its new, connected, state and preventing transient network properties due to synapse initialization to affect the results. All results reported in the present article were robust across simulations; i.e., the network always settled into the same state when initial conditions were identical. Noise due to the random number generator was of course different across simulations. For the study of gamma generation, simulations were stopped at $t = t_{\text{stop}} = 2^{11} - 1 = 2\,047$ ms; for the study of theta modulation of gamma oscillations, simulations were stopped at $t = t_{\text{stop}} = 2^{16} - 1 = 65\,535$ ms.

Measure of electrical activity The main phenomena in which gamma oscillations are usually said to occur are the local field potential (LFP) and electroencephalogram (EEG). Both these measures of neural activity are thought to reflect the summed total electrical activity in the dendrites of pyramidal cells (see, e.g., (Pettersen et al., 2012)). In order to analyse not only the spike times, but also the continuous electrical activity of our network, we generated a simulated LFP by calculating the negative summed total pyramidal cell potential:

$$V_{\text{total}}(t) = -\sum_{j=1}^{N_{\text{pyr}}} V_j(t) \tag{4.11}$$

and low-pass filtering this signal using an FFT-based finite impulse response filter with a −3 dB cutoff frequency of 300 Hz. The LFP is taken as the negative, rather than the positive, summed total, because the LFP is measured *outside* the cells in electrophysiological work. The summed total pyramidal cell potential in our model corresponds to the potential *inside* the cells, so a sign change is needed for our simulated LFP to accurately correspond to its electrophysiological counterpart.

Assessment of theta modulation of spike times To quantify the amount of theta modulaton of spike times in both the fast-spiking and pyramidal cell populations, we used two measures. To compute these, all of a subnetwork's spikes are first summed into 1 ms non-overlapping bins, such that the number of spikes in the interval $[t-1, t)$ is given by $A(t)$ (time in ms). The resulting population activity measure is then aggregated over all theta periods:

$$A_{\mathrm{aggr}}(\tau) = \sum_{k=0}^{\frac{t_{\mathrm{stop}}}{T_\theta}-1} A(kT_\theta + \tau) \tag{4.12}$$

with theta period $T_\theta = \frac{1000}{f_\theta} = 250$ and $0 \leq \tau \leq T_\theta$.

The first measure used to quantify spike time theta modulation is the squared Pearson correlation coefficient r^2, computed between this aggregate activity measure and the 'raw' theta signal given by:

$$\theta(t) = \sin(2\pi f_\theta t) \tag{4.13}$$

As a second measure of theta modulation of spike times, we introduce a simple *modulation score* ξ. To compute this measure, the aggregate activity A_{aggr} with bin size 1 ms is re-binned into 25 ms bins, resulting in an activity measure $B(v)$ with $v \in \{1, 2, \ldots, \frac{T_\theta}{25}\}$. This re-binning prevents any high-frequency (> 40 Hz) information from influencing the modulation score. The modulation score ξ is then given by:

$$\xi = \frac{\max(B) - \min(B)}{2 \cdot \mathrm{mean}(B)} \tag{4.14}$$

and can be interpreted as the *relative amplitude* of any theta oscillation, if such an oscillation is reflected in the spiking activity of the network. The two subpopulations of cells, the FS and P cells, differ strongly in their average firing rate (as do pyramidal and fast-spiking cell populations in the real brain). Therefore, the absolute amplitude of theta-modulated spiking activity cannot be used to compare the two subpopulations. We thus use this relative amplitude measure ξ, rather than an absolute amplitude, to compare the variations in activity in the two subpopulations of cells.

Note that, because of the period-wise aggregation described by equation 4.12, the time values τ and υ mentioned above correspond to certain phases $\varphi_\theta \in (0, 2\pi]$ in the theta cycle:

$$\varphi_\theta = \frac{2\pi\tau}{T_\theta} = 25\frac{2\pi\upsilon}{T_\theta} \tag{4.15}$$

This relationship will be used in plotting spike counts versus theta phase.

Measure of cross-frequency phase/amplitude coupling To quantify cross-frequency phase/amplitude coupling, we used a measure very similar to that employed by Canolty et al. (Canolty et al., 2006).

First, a gamma-only signal is derived from the LFP by band-pass filtering the latter signal between 30 and 150 Hz. We denote this gamma-only signal by $x_\gamma(t)$. We obtain the analytic representation $u_\gamma(t)$ of $x_\gamma(t)$ using the Hilbert transform:

$$u_\gamma(t) = x_\gamma(t) + i \cdot \widehat{x}_\gamma(t) \tag{4.16}$$

$$= a_\gamma(t) \cdot e^{i\varphi_\gamma(t)} \tag{4.17}$$

where $\widehat{f}$ denotes the Hilbert transform of a function f, $a_\gamma(t)$ is the analytic amplitude time series, and $\varphi_\gamma(t)$ is the analytic phase time series. We also obtain the analytic representation $u_\theta(t)$ of the 'raw' theta signal (equation 4.13). These two measures are combined into a single, complex-valued signal $z(t)$:

$$z(t) = a_\gamma(t) \cdot e^{i\varphi_\theta(t)} \tag{4.18}$$

Theta phase is distributed uniformly, since the theta rhythm is generated according to a simple sine function. Therefore, if gamma amplitude and theta phase are independent, the distribution of $z(t)$ values should be approximately radially symmetric relative to the origin in the complex plane. If, however, the two are not independent, clustering of $z(t)$ values in the complex plane is expected to occur. We use the distribution of $z(t)$ in the complex plane as a measure of theta phase/gamma amplitude coupling (see Figure 4.7).

Finally, note that our measure differs in an important respect from that used by Canolty et al. (Canolty et al., 2006). Canolty et al.'s measure was computed on two signals that were obtained by band-pass filtering the same signal using two different frequency bands. Our analysis uses a (gamma) band-pass filtered signal for the amplitude time series, but uses a different signal for the phase time series, namely the raw theta signal that governs the variable-rate input spike trains. This is simply an adaptation of Canolty et al.'s measure to a set of simulated data; the interpretation of the measure does not change.

Chapter 5

Predictive processing in visual search is associated with lateralized visual alpha and motor beta activity

5.1 Abstract

The speed of visual search depends on bottom-up stimulus features (e.g., we quickly locate a red item among blue distractors), but it is also facilitated by the presence of top-down perceptual predictions about the item. Recent evidence for the role of prediction in visual search has come from interrupted serial visual search tasks, which show faster performance for a resumed search than for a new search. We attempted to identify the nature, source, and neuronal substrate of the predictions that speed up resumed visual search. Human subjects were presented with a visual search array that was briefly flashed and repeated up to four times, while brain activity was recorded using magneto-encephalography (MEG). Behavioral data showed a marked reaction time facilitation on a proportion of trials during resumed visual search, resulting in a bimodal reaction time distribution. Neurophysiological recordings indicated that rapidly resumed visual search was associated with a prediction of (1) target location, by preparing the spatially relevant part of visual cortex for the upcoming stimulus, as reflected by hemispheric alpha band (8-12 Hz) modulation; and (2) target identity and its associated motor plan, by preparing the relevant motor cortical areas for an upcoming response, as reflected by beta band (15-30 Hz) modulation. Furthermore, the data suggest that these predictions are generated in the first 500 ms of processing the previous stimulus array, in a network consisting of medial superior frontal cortex and right temporo-parietal junction. These findings underscore the importance and nature of perceptual hypotheses for efficient visual search.

5.2 Introduction

Humans have a remarkable ability to quickly find a single item in a cluttered visual world, filled with other, distracting, items. Visual search has been the subject of intense study (Wolfe, 1998). Early research in visual search focused mostly on examining how bottom-up stimulus properties determined visual search efficiency (Treisman & Gelade, 1980). However, visual search efficiency is also strongly shaped by our prior knowledge of the scene, either derived from scene context (Biederman, 1972; Bar, 2004) or from past experience with a scene (Chun & Jiang, 1998; Stokes et al., 2012). Both of these factors provide a rich source of predictive information about the visual world that can be used to guide and optimize visual selection.

Recent evidence for the role of prediction in visual search has come from interrupted serial visual search tasks (Lleras et al., 2005, 2007). In a serial visual search task, subjects are briefly presented with a search array, consisting of a target amongst distractors. This search array is repeated after a short delay, until the subject makes a judgment on this target. The crucial behavioral finding is that subjects are sometimes much faster in responding to a search display that they had been presented with before, a phenomenon known as rapid resumption. It has been suggested that trials showing rapid resumption involve a perceptual prediction about the upcoming stimulus that is absent on trials without rapid resumption (Enns & Lleras, 2008). Interestingly, these predictions appear implicit (i.e., unconscious), as observers perform at chance when the search display fails to reappear (Lleras et al., 2005).

Several things remain unclear from these psychophysical experiments, however. First, what is the nature of the prediction? Do initial glimpses give rise to a spatial prediction ('This location may contain a target'), thus prioritizing a particular part of visual space for subsequent processing (Chun & Jiang, 1998; Stokes et al., 2012)? Such a prioritization would likely be reflected in a hemispheric lateralization of posterior alpha band (8-12 Hz) activity (Worden et al., 2000; Thut et al., 2006). Do subjects form a hypothesis about the target identity, based on initial glimpses ('The target may be an inverted T')? Given the appropriate target-response mapping, such a hypothesis would be reflected in lateralized beta band (15-30 Hz) activity over motor cortex (Pfurtscheller & Lopes da Silva, 1999; Donner et al., 2009; de Lange et al., 2013). Recent studies suggest that high-level aspects of a visual stimulus can be rapidly and unconsciously processed, potentially biasing subsequent visual search (Nakayama & Martini, 2011). Second, the neural implementation of the biasing of visual search by prior information is unclear. Which areas may be the sources and beneficiaries of resource allocation by prior information during visual search?

In this study, we tackle these questions by recording brain activity using magneto-encephalography (MEG) while subjects performed a serial visual search task. Foreshadowing our results, we replicate previous behavioral studies (Lleras et al., 2005, 2007) and find that on a proportion of trials subjects are much faster in responding to a display that has been presented before, resulting in a bimodal response time distribution. Furthermore, we find that brain activity prior to these fast subsequent responses is markedly different from that prior to slow ('normal') subsequent responses. Specifically, we find evidence for implicit predictions concerning both spatial location and target identity. Finally, neural activation in medial superior frontal cortex and right temporo-parietal junction appears to be involved in the generation of these sensory predictions that bias subsequent visual search.

5.3 Methods

5.3.1 Participants

Twenty healthy subjects (14 female; average age 22; range 18-31) participated in the study, which was conducted in accordance with the Declaration of Helsinki. Ethical approval was obtained from the local ethics committee (CMO region Arnhem-Nijmegen). One subject was excluded because of excessive head movement during the magnetoencephalograhy (MEG) recording, leaving nineteen subjects in the study. The subjects were paid for participating. All subjects were right handed individuals with normal or corrected-to-normal vision, and had no history of psychiatric or neurological illnesses (based on self-report).

5.3.2 Stimuli and experimental design

The experimental stimuli used consisted of a search display with fifteen distracters (L-shape, rotated at random multiples of 90 °) and one target (normal or inverted T-shape), which were presented using a PC running the MATLAB-based Psychophysics toolbox software (Brainard, 1997). Each trial started with a fixation cross (1 000 ms), followed by the search array stimulus (100ms) and a blank (1 300 ms). The stimulus-blank routine was repeated until the subject

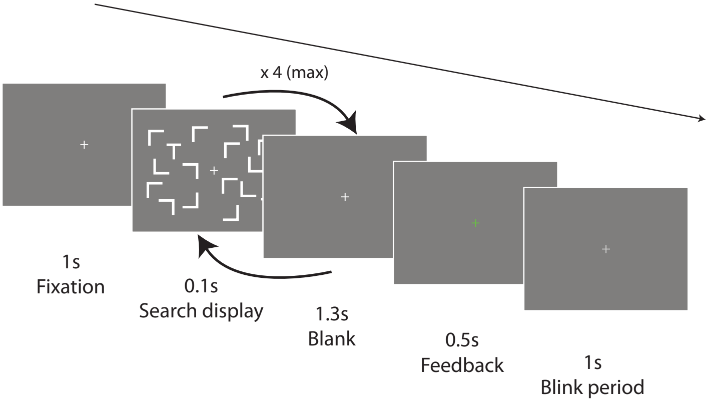

FIGURE 5.1: Experimental design. After a 1s fixation period, subjects were presented with a search array for 0.1s, consisting of 15 L-shaped distractors and 1 T-shaped target. The subject was instructed to respond with a button press as soon as possible when he/she felt confident whether the T was upright or inverted. The search display was presented iteratively, with 1.3s blanks in between displays, up to 4 times, or until the subject made a response.

responded, with a maximum of four repeats (Figure 5.1A). The task for the subject was to indicate the orientation of the target, giving a left-hand response for an upright T, or a right-hand response for an inverted T. The trial ended with a feedback screen (500 ms, green or red fixation cross for correct/incorrect response) and a dimmed fixation cross (1 000 ms), signifying a moment of rest for the subject. The subject was instructed to respond as fast and as accurate as possible, to blink as little as possible and to keep fixating on the fixation cross in the middle of the screen for the whole duration of the experiment. The search display consisted of eight objects in both the left and the right visual field. The stimulus array comprised 10 degrees of visual angle, while each object subtended 1 degree of visual angle. The exact position of the objects was randomly generated within these spatial constraints, with an equal occurrence of the target in the left and right visual fields. Before the actual experiment, subjects engaged in three practice blocks (50 trials each) outside the MEG and one practice block (20 trials) within the MEG environment. Hereafter, the subjects performed 10 blocks (50 trials each) of the task while MEG measurements were acquired.

For all reported MEG analyses, the time axis is such that t = 0s corresponds to the onset of the display at which the subject identified the target. By consequence, t = -1.4s corresponds to the onset of the previous display. Trials in which subjects identified the target after the first display were not included in the MEG analyses, nor were trials for which subjects made an incorrect response. When results refer to 'fast' or 'slow' responses or trials, 'fast' always refers to reaction times below the median of that subject, while 'slow' refers to reaction times above the median.

5.3.3 Experimental equipment

Stimuli were presented by back-projection onto a semi-translucent screen by an EIKI LC-XL100L projector. The projection measured 46 cm in width, and had a resolution of 1024 × 768 pixels. Subjects were seated in a magnetically shielded room, at 80 cm distance from the projection screen. Throughout the experiment, MEG was recorded using a 275-channel axial gradiometer CTF MEG system. An online lowpass filter (cutoff 300 Hz) was applied, and the data was digitized at 1.2 kHz. In addition, we continually recorded subjects' gaze position using an SR Research Eyelink 1000 eye tracking device, to monitor fixation during the task and to record eye blinks for offline artifact rejection. Also for artifact rejection purposes, the electrocardiogram (ECG) was recorded using three 10mm Ag-AgCl surface electrodes. After the MEG experimental session, structural magnetic resonance imaging (MRI) images were obtained from all subjects using a 1.5 T Siemens Magnetom Avanto system.

5.3.4 MEG data preprocessing

All MEG data was analyzed using the FieldTrip toolbox (Oostenveld et al., 2011) and custom-written scripts for MATLAB, version R2012a. Artifact rejection was done for each subject individually. First, trials with muscle or MEG jump artifacts were identified and removed from the data using a semi-automatic routine. Then, using Independent Component Analysis (ICA) (Bell & Sejnowski, 1995; Jung et al., 2000) we removed eye-movement and cardiac related activity from the MEG signals, by comparing ICA output to the eye tracker and ECG recordings. Finally, the data was inspected visually to remove any remaining artifacts that were not identified by these automated procedures. After artifact rejection, data was resampled offline to 400 Hz (after applying an anti-aliasing filter), to speed up subsequent analyses.

5.3.5 Frequency-domain source analysis

All reported MEG analyses were conducted in source space. To obtain source estimates, we always first conducted a frequency-domain beamformer known as dynamic imaging of coherent sources (DICS) (Gross et al., 2001). The DICS algorithm computes a spatial filter from the cross-spectral density matrix (CSD) of the data and a lead field matrix. To obtain the lead fields for each subject, we constructed a realistically shaped single-shell head model based on the individual anatomical MRI (Nolte, 2003), after spatially co-registering the MRI to sensor space MEG data by identifying fiducials in the nasion and the two ears. Each brain volume was divided into a grid of points spaced 8 mm apart, and warped to the template Montreal Neurological Institute (MNI) brain. The lead field was calculated for each grid point using a realistic volume conductor model (Nolte, 2003).

We selected data from a time window preceding the search display at which subjects identified the target, ranging between -1 and -0.1s, and subjected this to a Fourier transform. This particular time window was chosen such that it did not include transient activity related to the processing of the previous display (which had its onset at -1.4 s). For the reconstruction of alpha sources (Figure 5.5A), we estimated activity at 10 Hz, and applied a set of multiple Slepian tapers to obtain a frequency smoothing of 2 Hz, resulting in an activity estimate in the band of 8-12 Hz. For the reconstruction of beta activity (Figure 5.6A), we again used a Fourier transform after applying multiple Slepian tapers, now to obtain an activity estimate in the 16-30 Hz band (23 ± 7 Hz smoothing). From the computed Fourier spectra, the cross-spectral density (CSD) was computed. The CSD and the lead field together were used to compute our frequency-domain source estimates. We computed the CSD using trials from all conditions combined, and applied the resulting filters to the conditions separately.

For visualization, the beamformer results and associated statistics were interpolated onto the single-subject MNI template brain using smudge interpolation. Percentage change of $A > B$ is computed as $2\frac{A-B}{A+B} \cdot 100\%$ (% change in figure legends refers to power % change).

5.3.6 Time-domain source analysis and time-frequency analysis

For the grid points resulting in a significant source space frequency-domain difference, we computed a time domain beamformer to obtain temporal source activity estimates. Specifically, we computed a linearly constrained minimum variance (LCMV) (Van Veen et al., 1997) beamformer spatial filter, using the same lead field matrix as computed for the DICS beamformer. The LCMV beamformer uses the time-domain covariance, rather than the CSD, to compute the spatial filter. The covariance was computed from the entire epoch length (-2 to +1s), after subtracting the mean and fitting and subtracting a linear trend. As for the frequency domain beamformer, we computed the covariance from all conditions combined. Applying the LCMV spatial filter to our data resulted in single-trial estimates of time-resolved current density at the significant grid points in three orthogonal orientations. Subsequently computed power values were averaged over grid points and orientations to get a single estimate per source cluster.

For the signal thus reconstructed at each grid point, and for each orientation, we computed a time-frequency representation (TFR) of power (Figures 5.5B, 5.6B). To obtain the TFR of power, we used a sliding time window Fourier transform, moving over our trials' time axes in steps of 25ms. The time window was always 400ms long and multiplied with a Hanning taper of equal length. Estimates were obtained in steps at frequencies between 2 and 40 Hz, in steps of 2 Hz. For visualization purposes, the TFR maps were smoothed by applying a two-dimensional spline interpolation.

For the time courses of alpha and beta modulation (Figures 5.5C, 5.6C), we averaged the (unsmoothed) time-frequency representation of power in the frequency bands of 8-12 Hz and 16-30 Hz, respectively. Modulation is expressed in decibel (dB), and defined as $\text{mod} = 10 \cdot \log_{10} \frac{\text{pow}_{\text{left}}}{\text{pow}_{\text{right}}})$, where powleft and powright refer to the power of trials with either left or right target (in the case of visuospatial alpha modulation) or left or right response hand (in the case of motor beta modulation).

5.3.7 Statistical tests

To statistically quantify the robustness of our results, we performed cluster-based permutation tests (Maris & Oostenveld, 2007) across subjects. Specifically, for each voxel (either time/frequency (Figures 5.5B, 5.6B, 5.7B), time (Figures 5.5C, 5.6C), or $x/y/z$ (Figures 5.5A, 5.6A, 5.7A) voxels) we computed a difference metric between conditions. When raw power formed the input to the statistical test, we used the normalized difference; $\text{diff} = \frac{A-B}{A+B}$. When the input variables were already expressed as some relative metric (e.g. alpha/beta modulation in dB), a *t*-

score was used instead. This metric was computed both for the observed data and for 1 500 permutations of the conditions. Based on the per-voxel permutation distribution of descriptives thus obtained, we applied a threshold to the observed values, using the 95^{th} percentile of this distribution as the threshold value, to obtain cluster candidates. For each permutation, the cluster candidate with the highest sum of voxel-level descriptives was added to the permutation distribution of cluster statistics. The sum of descriptives for each observed cluster candidate was compared to this permutation distribution to assess significance for each cluster. For the source-space voxels, we used the maximum value of voxel-level descriptives per cluster (rather than the sum of all descriptives) as the cluster statistic to test, since spatial extent of clusters in beamforming typically is not closely related to the reliability of the source reconstruction (i.e., beamforming tries to make sources as small as possible; in the ideal case neighbouring voxels are independent). For the time- and time-frequency analyses, using the sum of descriptives makes more sense, as cluster extent is informative as to the reliability of the finding (i.e., neighbouring time/frequency points are likely highly correlated).

5.3.8 Whole-brain analysis

The MEG results presented in Figures 5.5 and 5.6 examined specific and well-established neurophysiological signals: lateralization of visuospatial alpha-band power (in relation to target location) and somatomotor beta-band power (in relation to target identity and associated button press). In addition to these analyses, that were motivated by the question of the nature of predictive signals (spatial, identity), we also performed a more exploratory analysis investigating the potential source of predictive signals. For this analysis, we computed a time-frequency representation of power (as described above) for all MEG sensor time courses, after computing an approximation of the vertical and horizontal planar gradient. Comparing these TFR maps between fast and slow responses yielded a significant sensor-level difference in the 10-20 Hz band, in the time window -1.5 to -1s, with a right-lateralized centro-frontal sensor topography (not shown). We subsequently selected these time and frequency limits to better localize the underlying sources using a beamformer source reconstruction, and proceeded as described above for the a priori contrasts. The statistical testing for these sources involved one additional step: for both the observed data and each permutation, we applied an image opening algorithm (Dougherty, 1992) to the binary maps of cluster candidates, before computing the cluster-level statistic. This step ensured separability of the clusters in space.

5.4 Results

We presented human subjects ($n = 19$) with a visual search array, consisting of 8 stimuli in both the left and right visual fields (Figure 5.1). One of these was an upright or inverted T-shaped target stimulus, the others were L-shaped distractor stimuli. The subjects were instructed to identify whether the target was upright or inverted by pressing a button with either the left (upright) or right (inverted) hand, as soon as they had found the target. The search array was presented briefly for 100 ms, followed by a 1300 ms blank screen, and repeated up to 4 times, or until the subject made a response. We refer to a single presentation of the search array as a 'display', and to the time window consisting of a display plus the blank that followed it as an 'epoch', in line with existing literature. A 'trial' thus refers to a set of between 1 and 4 epochs. During the entire experiment, we recorded brain activity using magneto-encephalography (MEG). Time courses reported for all MEG analyses follow the convention that $t = 0$ s corresponds to the onset of the display in which the subjects identified the target (with $t = -1.4$ s thus corresponding to the onset of the previous display). Trials in which the subject identified the target during the first display were not used for the MEG analyses, nor were trials with incorrect responses.

5.4.1 Rapid resumption during serial visual search

In just over half of all trials, subjects responded after seeing the display only once, so during the first epoch (number of trials = 266 ± 22, mean ± standard error across subjects). In the remaining 216 ± 22 trials, subjects responded after the second, third, or fourth display. For the trials with responses during the first epoch, the mean reaction time was 985 ± 14 ms. On average, subjects were significantly faster when they responded during a later epoch, with a mean reaction time of 752 ± 21 ms, (paired-sample $t_{18} = 10.00, p < 10^{-8}$). Importantly, the reaction time distribution showed a clear single peak around the mean reaction time for the first epoch, while this distribution was broader for the later epochs (Figure 5.2)., When inspecting the reaction time distribution normalized separately for the first and later epochs, a clear bimodal distribution was visible for the later epochs, but not for the first (Figure 5.3). We formally

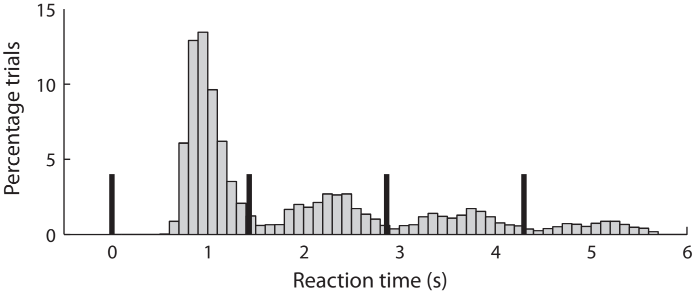

Figure 5.2: Grand average reaction time histogram across all epochs. Vertical black bars indicate the onset of each of the four displays. A clear difference is visible between the distribution after the first display and those after the subsequent displays.

tested this bimodality by fitting both a single Gaussian curve and a sum of two Gaussians to the reaction time distributions. We found that for the later epochs, the sum of two Gaussians fitted the data significantly better than the single Gaussian (Wald $F_{7,15} = 4.24$, $p = 0.045$), while this was not the case for the first epoch ($F_{7,15} = 2.07$, $p = 0.18$). (The Wald test controls for the trivial increase in explained variance because of the increase in degrees of freedom of the model used (Fox, 1997).) We thus confirm a clear distinction between trials that show rapid resumption and trials that do not, confirming previous findings (Lleras et al., 2005).

For every subject, we defined trials showing rapid resumption, or 'fast' trials, as those having a reaction time below the median for that subject, while 'slow' trials are those trials having a reaction time above the median. Fast and slow trials are only defined for epochs 2, 3, and 4. This resulted in a mean reaction time for fast trials of 492 ± 27 ms, and a mean reaction time for slow trials of 1010 ± 27 ms. The mean reaction time for slow trials was not significantly different from the mean reaction time in epoch 1 ($t_{18} = 1.11$, $p = 0.28$), indicating that the time course of visual search for a previously-seen display, without rapid resumption, is similar to the time course of visual search to a display that has not been seen before. Although hit rates were significantly higher for epoch 1, hit rate = 0.88 ± 0.019, than for later epochs, hit rate = 0.73 ± 0.027, $t_{18} = 6.10$, $p < 10^{-5}$, there was no significant difference between hit rate for fast and slow responses ($t_{18} = 0.89$, $p = 0.38$, Figure 5.4), demonstrating that fast responses were not

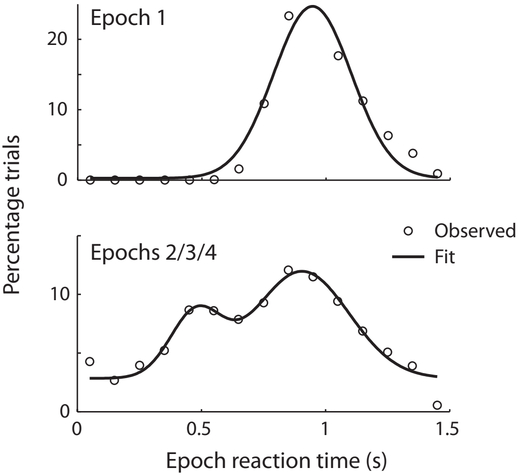

Figure 5.3: Grand average reaction time distributions, normalized separately for the first and subsequent epochs. Circles indicate the observed data, solid line indicates the best-fitting single (epoch 1) or double (epochs 2/3/4) Gaussian curve.

simply fast guesses due to a more liberal decision criterion.

5.4.2 Rapid visual search is associated with a preselection of relevant visual space

The visual search targets could be present in either the left or right visual field. Therefore, we reasoned that if rapid visual search is caused by a pre-selection of the relevant location where the target is expected to be found (based on earlier glances), we should see stronger modulation of visuospatial preparatory processes for fast than slow responses. To investigate this, we looked at alpha-band modulation over occipital and occipito-parietal cortex. It is a well-established finding that alpha (8-12 Hz) activity in posterior cortex is modulated in a retinotopically specific manner, when subjects covertly direct their visuospatial attention (Worden et al., 2000; Thut et al., 2006). Furthermore, it is known that the extent of this alpha modulation is predictive of subsequent target detection performance (Thut et al., 2006; Händel et al., 2011). Specifically, alpha-band modulation should be evident before the display at which subjects identified

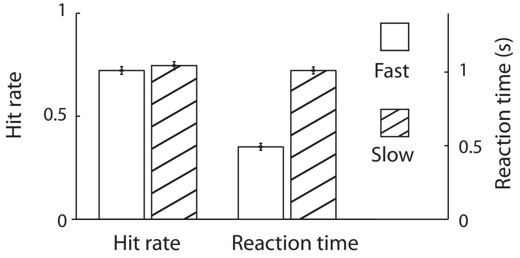

Figure 5.4: Reaction time and hit rate, separately for trials classified as having a fast or slow response. Reaction time is different by construction, while no significant difference was observed for hit rate.

the target, if part of the 'perception cycle' is completed before that display (as is hypothesized to be the case for the fast trials).

In line with this, we found significant alpha modulation in occipital cortex during the 900 ms period before display reappearance (Figure 5.5A; whole-brain cluster-corrected permutation test left cluster $p = 0.035$, right cluster $p = 0.0020$). Conducting a time-frequency analysis on source space signals extracted from the bilateral occipital clusters revealed that the effect was limited to the alpha band (Figure 5.5A).

Crucially, the anticipatory modulation of alpha differed between fast and slow trials. The alpha modulation (left versus right target) is plotted separately for the left and right hemisphere, and for fast and slow trials, in Figure 5.5C. We found that anticipatory modulation occurred for both fast and slow responses. The anticipatory alpha band modulation was stronger for the fast than for the slow trials (modulation in left versus right hemisphere, cluster-corrected permutation test $p = 0.003$). Moreover, the modulation appeared to have an earlier onset (i.e., the point of divergence between the red and blue lines in Figure 5.5C) for fast than for slow trials.

5.4.3 Rapid visual search is associated with a preselection of target identity

Having established that spatial location is a part of the perceptual predictions being made during rapid visual search, we next asked if also information con-

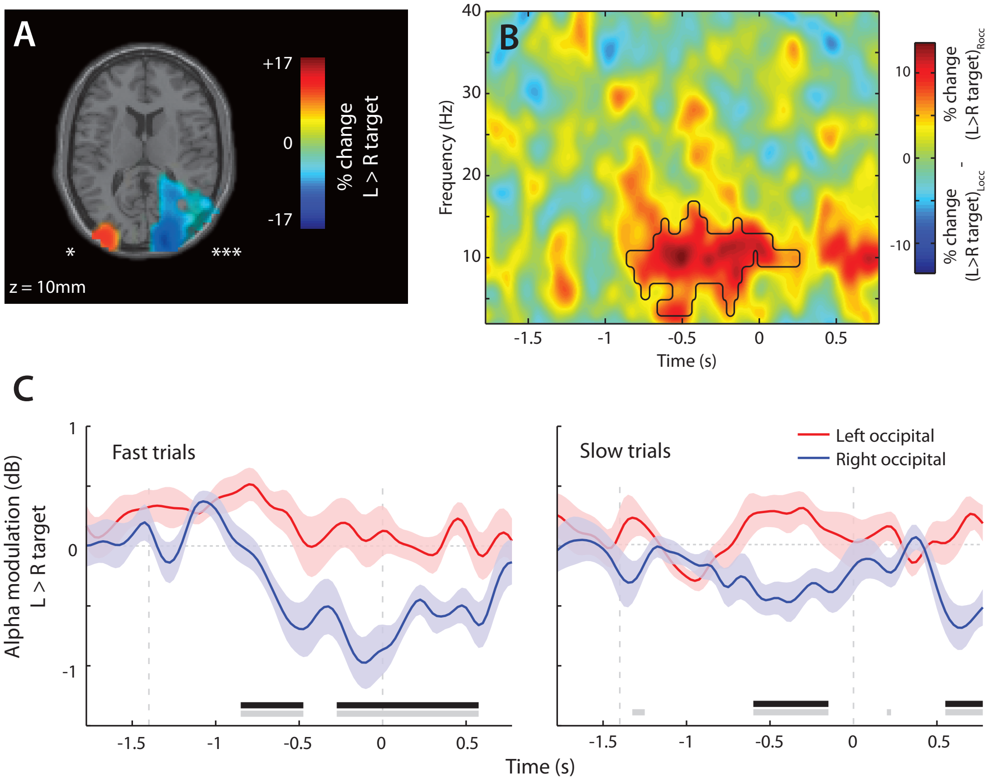

Figure 5.5: Anticipatory posterior alpha modulation. **(A)** Beamformer results for anticipatory alpha power, interpolated onto the single-subject MNI template anatomy (shown is a transverse slice at MNI $z = 10$ mm). Plotted activity is masked with cluster-corrected $p < 0.05$. The image is displayed using neurological convention (left hemisphere displayed on the left). * $p < 0.05$; *** $p < 0.005$. **(B)** Time-frequency representation of power in reconstructed source time series. Shown is the difference in alpha modulation between left and right occipital cortex. Outline, cluster-corrected $p < 0.05$. Locc, left occipital; Rocc, right occipital. **(C)** Time course of alpha modulation, shown separately for fast (left) and slow (right) trials. Anticipatory alpha modulation (i.e., a significant difference between the two traces in each panel) is visible for fast and slow trials, but is much more pronounced for the fast trials, and persists during stimulus processing. Error shading reflects unbiased within-subjects corrected standard error (Cousineau, 2005; Morey, 2008). Horizontal bars underneath the curves reflect uncorrected (gray) and cluster-corrected (black) significant differences at $p < 0.05$.

cerning target identity could be observed before the response display. Because our subjects were instructed to respond with a left hand button press when they perceived the target as upright, and with a right hand response for an inverted target, motor preparatory processes provided a window into the preselection of target identity and its corresponding motor plan (Donner et al., 2009; de Lange et al., 2013). It has previously been shown that lateralization of beta band (16-30 Hz) oscillatory activity observed over motor areas is a sensitive marker of preparation of either the left or the right response hand, with activity building up gradually during the accumulation of sensory evidence that is linked to a particular response (Donner et al., 2009).

Indeed, we observed significant preparatory modulation of beta power over the motor cortices (Figure 5.6A; whole-brain cluster-corrected permutation test left cluster $p = 0.01$, right cluster $p = 0.001$) during the 900 ms period before display reappearance. Conducting a time-frequency analysis on source space signals extracted from the bilateral central clusters revealed that the effect was most prominent in the beta band (Figure 5.6B).

Crucially, this prestimulus beta band modulation was markedly different for fast trials, compared to slow trials. The beta band modulation (upright versus inverted target) is plotted separately for fast and slow trials in Figure 5.6C. Significant preparatory beta band activity was observed starting at -0.5s for the fast responses (p = 0.001), while no preparatory beta band activity was observed for the slow responses. These findings are consistent with the notion of a perceptual prediction concerning target identity being generated before the onset of the display to which subjects responded, with the confirmation of this prediction following only after the onset of this display. This temporal dissociation between the prediction and confirmation phase then explains the occurrence of rapid resumption.

5.4.4 Superior frontal cortex and right temporo-parietal junction are associated with prediction generation

The above analyses focused on the nature of the perceptual prediction: is rapid visual search associated with a preselection of the relevant visual space, and/or the relevant target identity and associated motor program? We find empirical evidence for both of these preselection mechanisms. Next we asked whether we could localize the source of the perceptual prediction: is there any neural

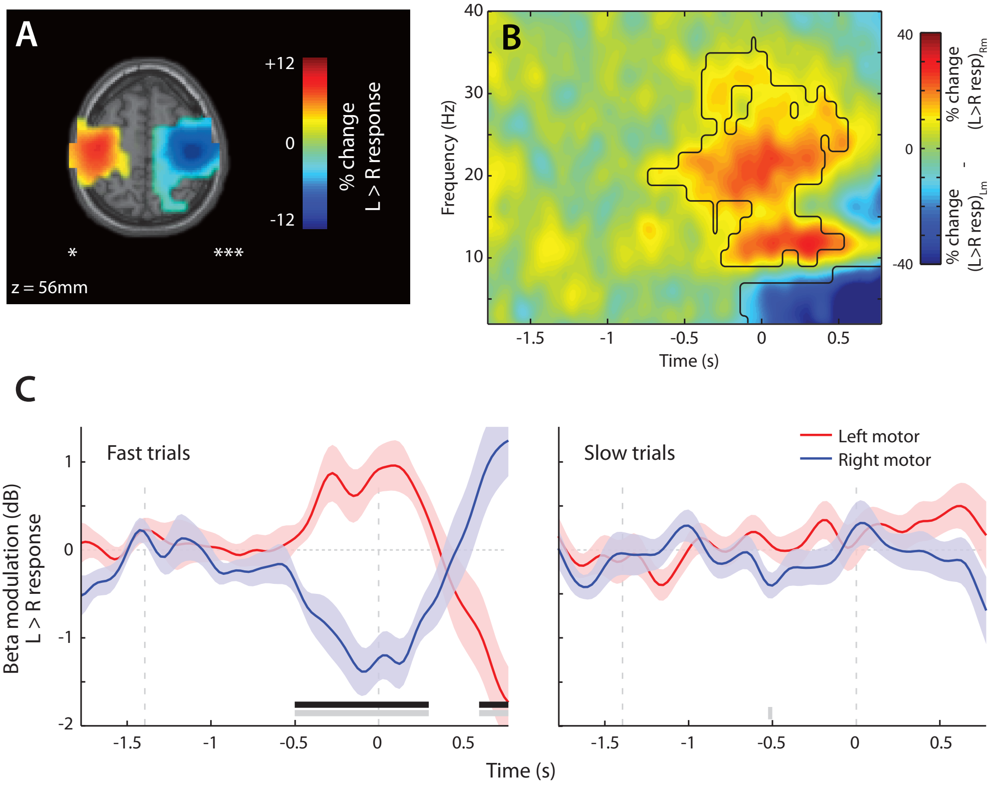

FIGURE 5.6: Anticipatory motor beta modulation. All panels analogous to Figure 5.5, but computed for the beta frequency band and in motor cortex source clusters. A clear anticipatory motor beta modulation is present for the fast trials, but not for the slow trials.

activity that distinguishes rapid from slow visual search and that precedes the biasing signals of visual and motor activity?

To answer this question, we performed an exploratory (i.e., 'whole-brain') analysis contrasting oscillatory power in fast versus slow trials. Indeed, we found a significant difference in the 10-20 Hz frequency band, in the time window between -1.5 to -1 s, which originated from two spatial clusters. These clusters were located on the medial surface of the superior frontal cortex (whole-brain cluster-corrected permutation test $p = 0.031$) and in the right temporoparietal junction ($p = 0.033$; Figure 5.7A). The time window of significant difference, $t = -1.5$ to -1 s, corresponds to the presentation of the search display preceding the search display at which subjects identified the target. As such, neural activity in these two brain regions around the time of stimulus processing dissociated between a perceptual prediction being generated or not.

5.5 Discussion

Visual search is often greatly facilitated by prior knowledge, such as context knowledge or previous acquaintance with a visual scene. In this study, we examined the nature of predictive information that leads to rapid resumption in visual search, as well as the neural sources that may generate this predictive information. We presented subjects with a repeated visual search array, and confirmed previous reports that studied interrupted visual search: When subjects resume a visual search, their reaction time distribution shows a bimodal pattern, compared to a unimodal response pattern for initial visual search. Neural data suggest that the markedly fast visual search times that can be seen at the early peak of the bimodal distribution are due to several predictive processes that are generated prior to the display at which subjects identified the target. Both information concerning target location and target identity were present in these perceptual hypotheses: we found significant preparatory alpha modulation over visual cortex and significant preparatory beta modulation over motor cortex. Furthermore, we found that medial superior frontal cortex and the right temporo-parietal junction might be responsible for generating these perceptual predictions.

The perceptual prediction contained information about the spatial location of the target. This was evident from the alpha modulation which was significantly elevated before the onset of the responded-to display. The alpha modulation

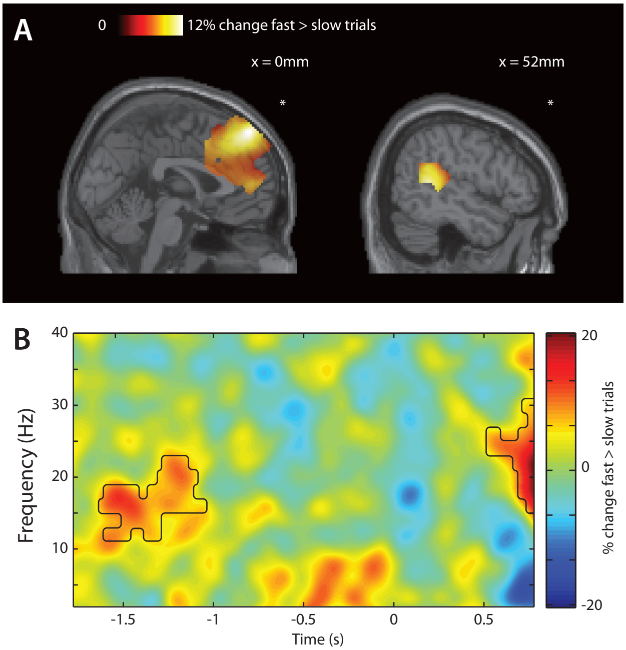

FIGURE 5.7: Neural sources active during the generation of a perceptual prediction. **(A)** Sources that are significantly stronger activated for fast versus slow responses after display n, during the processing of display $n - 1$. Shown are coronal slices at MNI $x = 0$ (left panel) and 52 (right panel) mm, revealing activation in medial superior frontal gyrus (left) and right temporoparietal junction. Activation maps are masked with cluster-corrected $p < 0.05$. * $p < 0.05$. **(B)** Time-frequency representation of power in reconstructed source time series for the frontal source cluster. Shown is relative change between fast versus slow trials. Outline, cluster-corrected $p < 0.05$.

was elevated throughout a much longer time window for trials with a fast response than those with a slow response. No prestimulus alpha modulation was observed for trials where there was no response (data not shown). The presence of anticipatory alpha modulation indicates an active preparation of the subjects' visual system for the upcoming target. It is known that the allocation of visual spatial attention modulates the topographical organization of alpha activity, when attention is directed in response to an endogenous cue (Worden et al., 2000; Thut et al., 2006). Our study did not employ such an endogenous cue; rather, the attentional effect was driven by the target stimulus itself. However, the time course of the effect (starting for the fast trials approximately 600ms, and for the slow trials approximately 1s after stimulus onset) suggests that this effect is mediated by a top-down anticipatory drive, and does not reflect a purely exogenous attentional shift.

Not just the location of the target, but also its identity was apparent as a prestimulus prediction. We found clear pre-stimulus beta modulation over the motor cortex in the direction of the correct target identity and corresponding response. This modulation was only present for subsequent 'fast' trials, i.e., in trials where a perceptual prediction was generated. No beta modulation was observed in trials without such a prediction. Build-up of choice-predictive activity in motor cortex during a perceptual decision making task is a well-established phenomenon (Donner et al., 2009) and can also be elicited by prior sensory expectations (de Lange et al., 2013). Because we observed a clear dissociation between fast and slow responses, we believe the proper interpretation of the beta band modulation here is as a reflection of an actively generated top-down prediction or expectation. If the beta band activity reflected only the passive accumulation of evidence, this would have resulted in a unimodal reaction time distribution (as we observe for the first search display), rather than the bimodality that we observed for resumed visual search. Our finding of a prediction concerning target identity being generated before stimulus onset is in line with psychophysical results demonstrating that rapid resumption is abolished when target identity is changed between subsequent displays (Jungé et al., 2009).

For displays with subsequently fast responses, we found greater activity in the right temporoparietal junction (TPJ) and the medial superior frontal gyrus (SFG) during the processing of the previous display, compared to slow responses. In other words, activity in these regions during processing of display $n - 1$ was predictive of whether subjects responded fast or slow after stimulus display n. Interestingly, these two nodes are part of two different frontoparietal networks typically associated with attentional processes. The right TPJ is considered to be part of the ventral attentional network, while (part of) the SFG is a node in the dorsal attentional network (Corbetta & Shulman, 2002). The dorsal network is thought to be involved in the direction and maintenance of top-down driven attention (e.g. in response to an endogenous cue), while the ventral network is more involved in the redirection of attention in response to salient external stimuli. Our observed right TPJ and SFG activation can be interpreted in light of these frontoparietal attentional networks: During processing of the search display, the right TPJ may on some trials signal the presence of the task-relevant target stimulus. Thus, the ventral attentional network of which it is part may execute its 'circuit breaker' role to shift attention in the direction of this stimulus. Because the stimulus array is followed by a relatively long delay, visuospatial attention needs to be endogenously maintained in order to prepare the sensory system for the upcoming next display. This task is performed by the dorsal attentional network, of which the SFG is part. Consistent with this idea, it has been shown that the dorsal network controls spatial attention through a modulation of posterior alpha activity (Capotosto et al., 2009), which we also observed. The frontal eye fields (FEF) form the frontal node in the dorsal attentional network. Although the extent of our activated cluster is consistent with it involving the FEF, the inherent uncertainty of the spatial resolution of MEG does warrant some caution in interpreting the functional neuroanatomy.

One crucial question is whether our results pertain to a perceptual process. A possible alternative explanation of the rapid resumption phenomenon could be that subjects have actually already identified the target on display $n - 1$, yet consciously decide to wait until the next display to be absolutely sure of their decision. However, if this were the case, subjects would be expected to perform above chance when they are forced to respond during a trial for which no response had been made yet. In contrast to this notion, Lleras et al. (2005) found that when a display is presented, but, unexpectedly to the subjects, not repeated, performance is at chance for trials during which subjects chose to withhold their response until a subsequent display. This suggests that the predictive mechanisms that lead to rapid resumption in visual search are implicit, rather than strategic.

Do subjects actually make an informed prediction, or could our results be explained by them randomly directing their attention to the right location at the right time? If the attentional spotlight (by random wandering) happens to be at the location of the target at the onset time of the display, subjects might be expected to respond faster than when attention happens to be directed away from the target. This phenomenon could also result in a bimodal distribution of reaction times. However, this account dictates that also responses after the first display should show such a bimodality. In contrast, we find a bimodal reaction time distribution only after second and later displays. Therefore, we can conclude that the biasing of spatial attention and target identity-related response activity only occurs in response to visual information (i.e., the first display). This visual information is therefore likely the source of the spatial and target-identity predictions being generated.

Summarizing, based on our results, how is visual search helped by prior glances? We find that on some trials, subjects find the target immediately after the first display, and make their decision. This corresponds to all three phases (activate, predict, confirm) of the 'perception cycle' being completed after only a single display (Enns & Lleras, 2008). On other trials, a subthreshold signal reflecting the target's location and identity is perceived after the first (or a subsequent) display (the 'activate' phase). This is associated with activation of the stimulus-driven (ventral) and top-down controlled (dorsal) attentional networks. In turn, the dorsal attentional network effects a prioritization of the visual field where the target is expected to occur, and a prioritization of the motor decision associated with the identity of the target (the 'predict' phase). These biasing processes before the target display onset then lead to a rapid identification of the target, as only the third ('confirm') phase of the perception cycle needs to be completed.

Chapter 6

Lateralized alpha and beta oscillations index the goal of upcoming saccades during free viewing

6.1 Abstract

It is well-established that the direction of covert spatial attention is associated with a spatially specific pattern of oscillatory activity in the alpha band over occipital and parietal cortical regions. Interestingly, one brain region typically associated with the direction of covert attention, the posterior parietal cortex, is also critically involved in the generation of saccadic eye movements, i.e., the direction of overt attention. While the neural basis of saccades has been extensively studied, typically these studies involve the production of saccades in some experimentally predefined direction (i.e., towards or away from a cue stimulus). Surprisingly little is known about the neural basis of self-initiated saccades in humans during free viewing. Here, we investigated this phenomenon by presenting human subjects with natural images, which they were instructed to examine and remember. We recorded eye movements using a video-based eye tracker, and brain activity using magneto-encephalography (MEG). Contrasting brain activity just prior to a leftward versus a rightward saccade, we find that these conditions are dissociable by (1) alpha power in the right posterior parietal cortex, (2) alpha and beta power in the left occipital cortex, and (3) beta power in the cerebellum. Contrary to expectations, we do not find evidence of oscillatory phase reset in response to a saccade. The occipital and parietal findings suggest a common mechanism underlying the direction of both covert and overt attention, and tie this mechanism to visual exploration, or 'active sensing', in the human.

6.2 Introduction

The act of spatially directing attention without moving the eyes is known as covert attention. This is opposed to overt attention: the reorienting of attention which involves moving the eyes and foveating the attended target. When humans covertly direct their spatial attention to the left or right visual hemifield, this results in a clearly lateralized pattern of alpha oscillatory activity over posterior cortices (Worden et al., 2000; Kelly et al., 2006; Thut et al., 2006; Rihs et al., 2007). The amount to which subjects direct their spatial attention is predictive of cognitive performance (Thut et al., 2006; Händel et al., 2011) and clinically relevant (ter Huurne et al., 2013). The direction of covert spatial attention is strongly associated with the parietal cortex, in particular its posterior part (Colby & Goldberg, 1999; Corbetta & Shulman, 2002). Interestingly, this brain region is also important for the generation of saccadic eye movements, i.e. the direction of overt attention (Pierrot-Deseilligny et al., 2004; Van Der Werf et al., 2009; Anderson et al., 2012). The parietal eye fields (PEF), located in posterior parietal cortex, have both direct and indirect (through the frontal eye fields, FEF) projections to the superior colliculus, which in turn projects to brainstem nuclei for the generation of saccades (Goldberg, 2000; Pierrot-Deseilligny et al., 2004). Indeed, it has been repeatedly suggested that both the covert and overt orienting of attention are subserved by similar neural mechanisms (Posner, 1980; Rizzolatti et al., 1987; Moore & Fallah, 2001).

Although the neural pathways for the generation of saccades are relatively well known, the vast majority of studies into this topic have focused on saccades generated under fairly artificial conditions. Typically, subjects are instructed to saccade toward some peripherally presented target (a pro-saccade), or in the opposite direction (an anti-saccade). While such an experimental protocol is highly valuable, it dissociates saccadic behaviour from its ecological context, namely, that of visual exploration in order to actively sense the visual world (Schroeder et al., 2010). Examples of studies employing free viewing of natural images to study the neural basis of saccades are available (e.g. Ito et al., 2011; Brunet et al., 2013; Jutras et al., 2013), but the relation between exploratory saccadic behaviour and the oscillatory mechanisms typically associated with covert attention is unclear, especially in humans.

Here, we present novel results on the role of neural oscillations in the planning and generation of saccades. In brief, we find that alpha activity in the right posterior parietal cortex; alpha/beta activity in left occipital cortex; and beta activity in the right cerebellum are predictive of whether an upcoming saccade is directed leftward or rightward. These results are in agreement with the idea that overt and covert attention are subserved by similar neural systems, and highlight the continuously updating nature of spatial attention during natural, free viewing.

6.3 Methods

6.3.1 Participants

19 subjects (8 female; age range 18–51) with no history of neurological or psychiatric disorders (based on self-report) participated in this experiment. All subjects gave written informed consent according to the Declaration of Helsinki. The study was approved by the local ethics committee (CMO region Arnhem-/Nijmegen). Due to technical difficulties during MEG acquisition (specifically, a mid-session crash of the MEG system's electronics array), data for three subjects had to be excluded. Two further subjects were excluded because of excessive head movement (¿ 1 cm) during the MEG session. Finally, one subject was excluded because the eye tracker was unable to properly track this subject's gaze position. This leaves a total of 13 subjects on which the analyses are based.

It should be noted that, at the time of writing, we are acquiring more data sets using the same experimental setup.

6.3.2 Experimental design

Each experimental session consisted of six blocks:

1. Subjects were instructed to fixate at a small fixation dot in the center of the screen (4 minutes).

2. Subjects were instructed to keep their eyes closed (4 minutes).

3. Subjects were presented with full-colour natural images, representing a human face, birds, or a natural landscape. Subjects were instructed to try to remember as much of each image as possible. Each image was presented for 5 s, the inter-image-interval was 1 s. Images subtended 26.2 x 19.7 degrees of visual angle and were centered on the screen. The images block lasted for a total of 10 minutes.

4. Subjects were instructed to stare ahead for 4 minutes in a complete dark room.
5. Subjects were instructed to make occasional saccades "as if they were still looking at the computer screen", while the room was entirely dark (8 minutes).
6. Subjects were presented with light flashes from a Xenon stroboscope at a rate of ~ 1 Hz in a dark room (8 minutes).

Between each of the blocks there was a self-paced break for the subject.

We here only report results concerning the image viewing block. We defined leftward and rightward saccades as those with a horizontal component > 1 degrees and a vertical component < 6 degrees.

6.3.3 Experimental equipment

Stimuli were presented by back-projection onto a semi-translucent screen by an EIKI LC-XL100L projector. The projection measured 46 cm in width, and had a resolution of 1024 × 768 pixels. Subjects were seated in a magnetically shielded room, at 80 cm distance from the projection screen. Throughout the experiment, the magnetoencephalogram (MEG) was recorded at a sampling rate of 1.2 kHz using a 275-sensor axial gradiometer CTF MEG system. Before digitization, an anti-aliasing lowpass filter (cutoff 300 Hz) was applied. In addition, we continuously recorded subjects' gaze position using an SR Research Eyelink 1000 eye tracking device. At the start of the experiment, the eye tracker was calibrated by having subjects look at a sequence of 9 points presented in a uniform 3 × 3 grid. After the MEG experimental session, structural magnetic resonance imaging (MRI) images were obtained from all but one of the subjects using a 3 T Siemens Magnetom Skyra system.

6.3.4 MEG data preprocessing

All MEG data were analyzed using MATLAB R2012a, using custom-written scripts and the FieldTrip toolbox (Oostenveld et al., 2011). All data was inspected for artifacts using a semi-automatic routine. Segments containing MEG SQUID jumps were removed, as were all data segments containing eye blinks or excessive muscular activity.

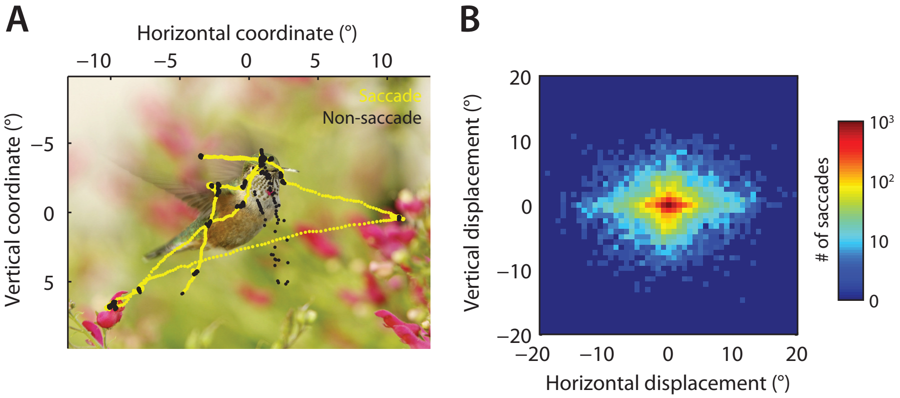

Figure 6.1: **(A)** An example stimulus image that was presented to our subjects. Gaze position (tracked at 1.2 kHz) for one subject is superimposed; segments classified as saccadic are plotted in yellow, while non-saccadic segments (fixation and possibly noisy data) are plotted in black. **(B)** The distribution of observed saccades, as a function of horizontal and vertical displacement. Note the logarithmic color scale.

6.3.5 Source analysis

MEG source analysis was performed using a beamforming spatial filtering technique known as dynamic imaging of coherent sources (DICS) (Gross et al., 2001). This analysis was based on the data recorded from the axial gradiometers. The DICS algorithm computes a spatial filter from the cross-spectral density matrix (CSD) of the data and a lead field matrix. Data was selected in the interval between 0.3 and 0.05 s before saccade onset, separately for leftward and rightward saccades. The 250 ms-window thus selected resulted in a spectral resolution of 4 Hz. The CSD was estimated using the combined data of the two conditions. To obtain the lead fields for each subject, we constructed a realistically shaped single-shell head model based on the individual anatomical MRI (Nolte, 2003), after spatially co-registering the MRI to sensor space MEG data by identifying fiducials at the nasion and the two ears. Each brain volume was divided into a grid of points spaced 7.5 mm apart, and warped to the template Montreal Neurological Institute (MNI) brain. The lead field was calculated for each grid point (Nolte, 2003). The estimated power in source space was averaged over trials. For visualization purposes, the grand-average grid was interpolated onto the single-subject MNI template brain.

For the grid points resulting in a significant source space frequency-domain difference, we computed a time domain beamformer to obtain broadband temporally-resolved source activity estimates. Specifically, we computed a linearly constrained minimum variance (LCMV) (Van Veen et al., 1997) beamformer spatial filter, using the same lead field matrix as computed for the DICS beamformer. The LCMV beamformer uses the time-domain covariance, rather than the CSD, to compute the spatial filter. As for the frequency domain beamformer, we computed the covariance from all conditions combined. Applying the LCMV spatial filter to our data resulted in single-trial estimates of time-resolved current density at the significant grid points. From these single-trial time courses, we computed time-frequency representations of power (see below).

6.3.6 Cluster-based permutation statistics

To statistically quantify our results, we performed cluster-based permutation tests (Maris & Oostenveld, 2007) across subjects. Specifically, for each voxel we computed the relative difference between conditions: $\text{diff} = \frac{A-B}{A+B}$. This metric was computed both for the observed data and for 1 000 permutations of the conditions. Based on the per-voxel permutation distribution of descriptives thus obtained, we thresholded the observed values with the 95^{th} percentile of this distribution to obtain cluster candidates. For each permutation, the cluster candidate with the maximum voxel-level descriptive was added to the permutation distribution of cluster statistics. The maximum descriptive for each observed cluster candidate was compared to this permutation distribution to assess significance for each cluster.

6.3.7 Evoked activity

For the event-related field (ERF) analysis, MEG data was low-pass filtered at 45 Hz using a Kaiser-windowed sinc finite impulse response (FIR-WS) filter (Widmann et al., in press). Artifact-free epochs from 0.3 s before saccade onset to 0.4 s after saccade onset were extracted, averaged per subject, and a grand average was computed from these per-subject averages. ERF data are presented as axial gradiometer data.

In addition to presenting a grand-average ERF, we also analyzed evoked activity separately for each saccade. Specifically, we investigated the influence of saccade duration on the evoked field. For this purpose, we aligned each saccade such that time t = 0 s corresponded to saccade offset (i.e., fixation onset), allowing us to plot the individual ERFs (Jung et al., 2001), sorted by saccade duration, and with the saccade onset trace superimposed. We applied a 100-trial wide moving average kernel to the ERP image to increase the signal-to-noise ratio (Jung et al., 2001). Note that for visualization, we use all saccades, for all subjects, stacked together. However, all statistical tests reported in the text use variance across subjects (i.e., they are random-effects analyses).

6.3.8 Time-frequency analysis

To get a time-frequency representation (TFR) of power and inter-trial coherence (ITC), we used a sliding time window fast Fourier transform (FFT) approach. A linear trend was fitted to the epoched data and removed before spectral analysis. Frequencies of interest ranged from 4 to 40 Hz in steps of 1 Hz. The sliding time window was 300 ms long, with a temporal resolution of 50 ms. Each instance of the sliding time window was multiplied by a Hanning taper and Fourier-transformed, thus yielding a time-resolved complex Fourier spectrum. Power values $\text{pow}_n(f,t)$ for trial n, frequency f, and time point t were computed by squaring the absolute value of the Fourier coefficients $c_n(f,t)$, i.e. $\text{pow}_n(f,t) = |c_n(f,t)|^2$, and were averaged over trials. Inter-trial coherence was defined as the absolute value of the complex mean of the Fourier values, after normalizing them by unit length:

$$\text{ITC}(f,t) = \left| \frac{1}{N} \sum_{n=1}^{N} \frac{c_n(f,t)}{|c_n(f,t)|} \right|$$

For the analysis of sensor data, TFRs of power and inter-trial coherence were computed after the data was transformed to an approximation of the planar magnetic gradient, which results in maxima that are located above the underlying neural generating, thus providing a topography which is more easily interpretable (Hari & Salmelin, 1997; Bastiaansen & Knsche, 2000).

For visualisation, TFR maps were smoothed using a two-dimensional spline interpolation.

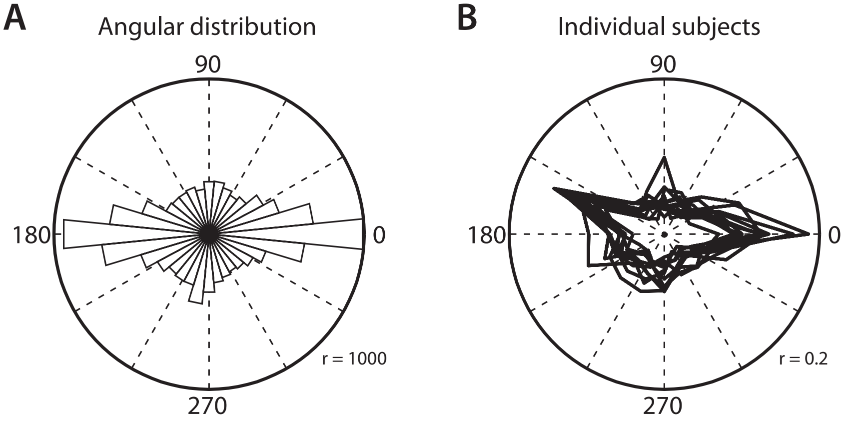

FIGURE 6.2: Distribution of saccade angles. **(A)** Saccades for all subjects combined. Note the dominance of horizontal over vertical saccades. **(B)** Normalized saccade angle histograms for each subject.

6.4 Results

Human subjects freely viewed and explored images of human faces, natural scenes, or birds, each presented 5 s at a time. We recorded eye movements using a video-based eye tracker, and brain activity using MEG.

6.4.1 Saccade characteristics

On average, 1121.4 ± 236.3 (± standard deviation over subjects) saccadic eye movements were detected per subject, after data segments contaminated with artifacts were removed (see Figure 6.1A for an example eye movement trace). Average saccadic amplitude was 3.9 ± 0.9 degrees of visual angle (see Figure 6.1B). Saccades were significantly more pronounced in the horizontal (2.9 ± 0.6 degrees) than the vertical (1.9 ± 0.5 degrees) direction (paired $t12 = 9.17$, $p = 9 \cdot 10^{-7}$; see Figure 6.2). On average, a single saccade lasted for 37 ± 4 ms, and inter-saccade interval was 295 ± 69 ms (Figure 6.3). There were just as many saccades oriented leftward (32.1 ± 5.5 %) as rightward (31.9 ± 5.2 %; note that these two values do not sum to 100% because only unambiguously left- or rightward oriented saccades were included in the relevant analyses).

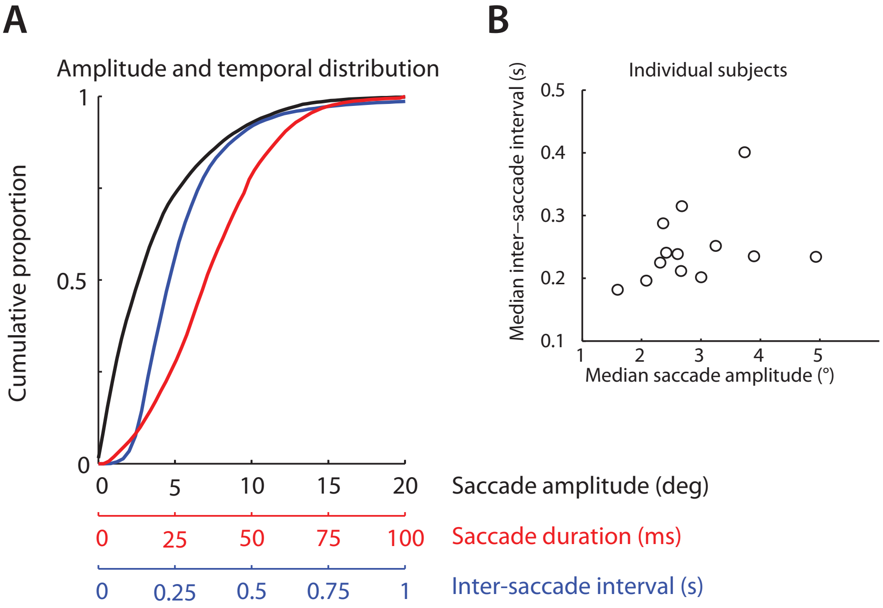

FIGURE 6.3: **(A)** Cumulative histogram of saccade amplitude (black), saccade duration (red) and inter-saccade interval (blue), combined over all subjects. **(B)** Median saccade amplitude and inter-saccade interval for each subject individually.

6.4.2 Oscillatory sources dissociating leftward from rightward saccades

In covert attention paradigms, the typical comparision is leftward versus rightward attention, which reveals robust lateralized activity in the alpha band (Worden et al., 2000; Kelly et al., 2006; Thut et al., 2006; Rihs et al., 2007). In a similar vein, we here contrasted left- versus rightward saccades, in order to determine which neural signature, if any, is associated with the direction of overt spatial attention. We computed the contrast of interest within the a priori defined alpha (6-14 Hz), beta (16-24 Hz), and gamma (65-95 Hz) bands.

First, using a frequency-domain beamformer analysis, we found that leftward saccades are preceded by elevated alpha (6-14 Hz) power in the right posterior parietal cortex, when compared to rightward saccades (Figure 6.4A; cluster-permutation test $p = 0.033$). Contrasting source level alpha power for left versus

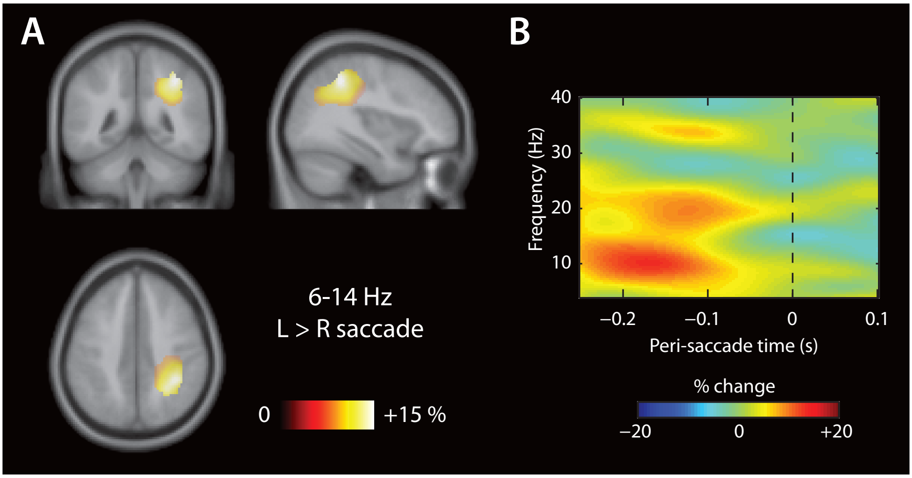

FIGURE 6.4: Alpha power over right posterior parietal cortex is elevated prior to a leftward, when compared with a rightward, saccade. **(A)** DICS beamformer results of alpha power, interpolated onto the Montreal Neurological Institute (MNI) template brain. The topographical map is masked with cluster-corrected $p < 0.05$. **(B)** Source-level time-frequency representation of power (left versus right saccade), performed in the cluster identified in (A).

right saccades also revealed a negative cluster in the right orbit. Given the almost certainly extraneural nature of this cluster, we do not show this source in our figures. We subsequently extracted broadband time-resolved activity from the activated cluster, and performed a time-frequency analysis on the resulting time courses (Figure 6.4B). This reveals that the activity is most prominent in the alpha band, and extends (weakly) into the beta band. Figure 6.4B also shows that the activity is strictly pre-saccadic, and does not persist post-saccade.

Second, contrasting source level beta band (16-24 Hz) activity revealed two significant clusters: one in the left occipital cortex (Figure 6.5; $p = 0.028$) and one in the medial to right cerebellum (Figure 6.6; $p = 0.028$). Performing source-level time frequency analysis revealed that the left occipital cluster, although identified using a beta frequency beamforming contrast, actually shows just as strong pre-saccadic activity in the alpha band (Figure 6.5B). The cerebellar cluster, in contrast, shows an activity profile limited to the beta band (Figure 6.6B).

It should be noted that these effects cannot be explained by activity induced

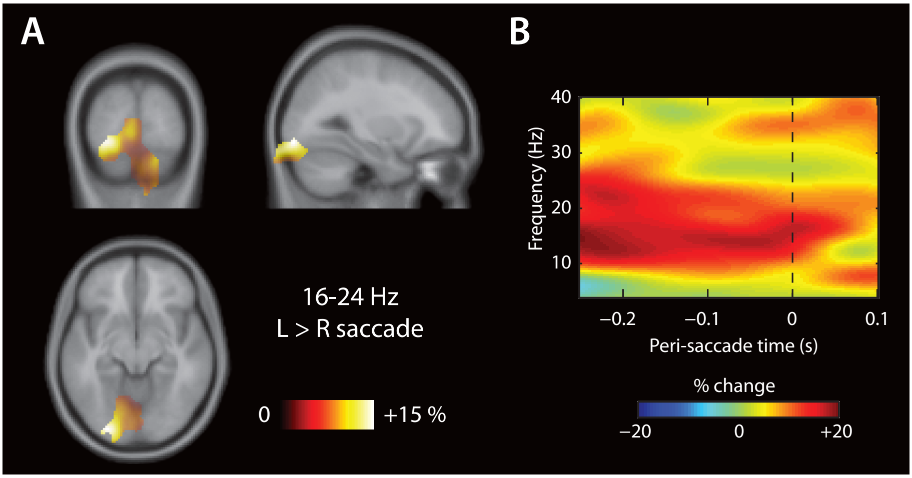

FIGURE 6.5: Alpha and beta power over left occipital cortex are elevated prior to a leftward, when compared with a rightward, saccade. Panels analogous to Figure 6.4.

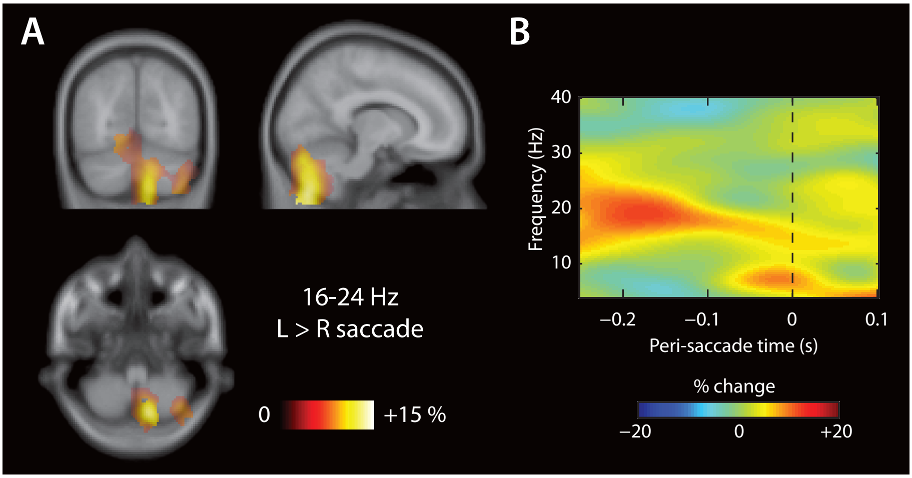

FIGURE 6.6: Beta power over medial/right cerebellum is elevated prior to a leftward, when compared with a rightward, saccade. Panels analogous to Figure 6.4.

by the previous saccade, as performing the identical analysis on a post-saccadic time window did not reveal any significant clusters (data not shown). Therefore, we conclude that activity in right posterior parietal cortex, left occipital cortex, and right cerebellum is involved in saccade generation in a spatially specific manner. We discuss these findings in more detail below.

We did not observe any significant differences in the gamma frequency band between left- and rightward saccades.

6.4.3 Saccade-evoked brain activity is locked to saccade onset, rather than offset

We next shifted our focus from pre-saccadic to post-saccadic activity. We computed the grand-average saccade-evoked response (event-related field, ERF); this is shown in Figure 6.7A. The pattern that emerges is consistent with a visual P1/N1/P2 complex typically observed after visual stimulus onset (Luck et al., 2000), and its largest deflection at ˜100 ms has a sensor topography is compatible with a generator located in occipital cortex (Figure 6.7B).

The saccade-locked ERF could be a consequence of the arrival of novel visual information in sensory cortex, following the onset of fixation. If this were the case, the saccade-locked ERF should be primarily locked to saccade offset (i.e. fixation onset), since the earliest time at which novel visual input could arrive is the onset of fixation. However, an alternative cause for the saccade-locked ERF deflections is an event related to saccade onset, e.g. the visual transient caused by saccade initiation, or a non-visual phenomenon, such as an efferent copy of the saccadic motor program. To disambiguate between these two possibilities, we computed the ERF locked to fixation onset, and sorted the saccades according to saccade duration. Result for this analysis are shown in Figure 6.7C: the dashed vertical line indicates fixation onset, while the solid vertical curve indicates saccade onset. It is clear from this plot that the main ERF deflections are time-locked to saccade onset, rather than offset. The strong negative correlation between saccade duration and the time of the highest saccade-locked deflection (Spearman correlation across saccades per subject, $r = -0.70 \pm 0.24$, $p < 10^{-6}$ in all subjects) indicates that this is a robust phenomenon observed in all subjects. Thus, the saccade-locked ERF in visual cortex is locked to saccade initiation. Either the visual transient or the motor program associated with this saccade initiation could be the crucial factor.

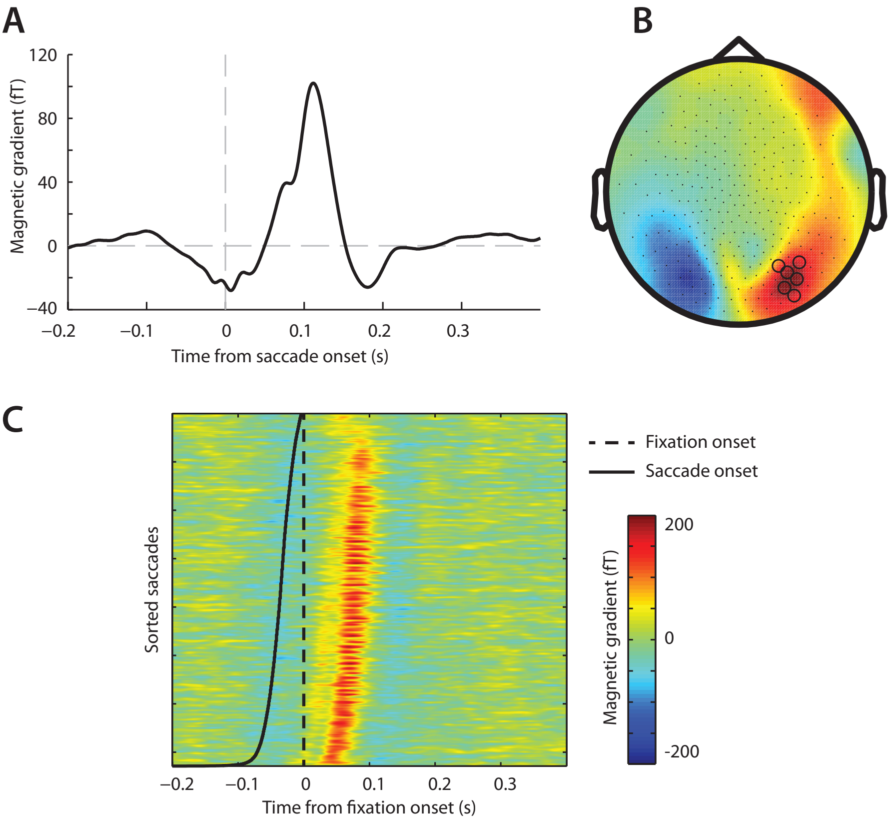

Figure 6.7: Saccadic event-related field (ERF). **(A)** Grand-average saccade-locked ERF, for the axial sensors highlighted in (B). **(B)** Topography of the primary ERF deflection at ~100 ms after saccade onset. Note the predominantly occipital topography, consistent with a generator in visual cortex. **(C)** ERFs locked to fixation onset, for all observed saccades, sorted according to saccade duration. Superimposed are fixation onset (dashed line) and saccade onset (solid line). The primary deflection is clearly locked to saccade, rather than fixation, onset.

6.4.4 Time-frequency representations of power and inter-trial coherence

Next, we investigated the modulation of neural oscillations surrounding a saccade. The grand-average time-frequency representation (TFR) of power is shown in Figure 6.8A. After a transient increase in power at ~ 100 ms, a more sustained decrease in alpha band power can be observed, with a predominantly occipital topography (0.2-0.5 s; Figure 6.8B). Note that this topographic representation is obtained from comparing post- to pre-saccadic power. Since the saccades all occurred during natural viewing, it is inevitable that further saccades occur during the time window used as a baseline for some saccades. Therefore, the apparent alpha band decrease evident from Figure 6.8A might partly be caused by an increase in overall power following previous saccades.

Apart from saccade-related power, we also analyzed saccade-related oscillatory phase consistency, defined as inter-trial coherence (ITC). We observed a clear transient increase in ITC around saccades (Figure 6.8C), with an occipital topography (0.2-0.5s; Figure 6.8D). The transient increase in (broadband) ITC is a frequency-domain reflection of the strong saccade-evoked response (see Figure 6.7A). In contrast to previous reports based on invasive monkey electrophysiology (Ito et al., 2011) we did not observe elevated ITC constrained to the alpha frequency range.

6.5 Discussion

We investigated the neural signatures of volitional saccades, initiated by humans engaged in a free viewing task. First, we found that neural structures that are known to be involved in the direction of covert attention are also involved in the reorienting of overt attention during free visual exploration. Specifically, when comparing the activity prior to a leftward versus a rightward saccade, the right posterior parietal cortex showed elevated alpha band activity; the left occipital cortex showed elevated alpha and beta band activity, and the medial/right cerebellum showed elevated beta band activity. Second, we reported an evoked response that shares its overall profile with the familiar P1/N1/P2 complex observed in response to visual stimulation (Luck et al., 2000). Interestingly, this evoked response was clearly locked to saccade onset, rather than fixation onset, indicating that it cannot entirely be explained by the arrival of novel visual information in occipital cortex. Third, we did not find evidence for phase-locking of ongoing oscillations in response to a saccade, in contrast to our expectations.

Alpha band activity in right posterior parietal cortex was stronger prior to a leftward saccade than prior to a rightward saccade. The posterior parietal cortex is known to be involved in the direction of both covert and overt spatial attention (Colby & Goldberg, 1999; Pierrot-Deseilligny et al., 2004), as part of the dorsal attentional orienting network (Corbetta & Shulman, 2002). This involvement is more pronounced for the right hemisphere than the left; specifically, the right parietal cortex is responsible for attentional orienting to either of the visual fields, while the left parietal cortex is primarily responsive to orienting to the right visual field (Heilman & Abell, 1980). Our results add to this body of knowledge by showing that the right posterior parietal cortex is not only involved in guiding spatial attention in a top-down controlled manner, but also continually guides spatial attention during free visual exploration.

In previous studies (Van Der Werf et al., 2008), it was reported that planning of a cued horizontal (pro- or anti-) saccade is associated with a decrease in contralateral occipital and parietal alpha power. A curious discrepancy between the Van der Werf study and our parietal result is that we observe an increase in contralateral parietal alpha power. We do not have a clearcut explanation for this discrepancy. It should be noted, though, that the peak decrease in the Van der Werf study is located more posteriorly than the one we observed, and indeed might partly include occipital activation as well (see their Figure 7C). The occipital modulation we observed is in line with Van der Werf et al.'s observations. A further important difference between our study and theirs is that they used an explicit cue to indicate saccade direction, followed by a fixed delay, after which the saccade was initiated. We analyzed saccades endogenously generated using natural viewing. It would be highly interesting to see what light future studies can shed on the observed discrepancy.

The posterior alpha rhythm is often interpreted as reflecting the (spatially specific) functional inhibition of brain regions (Jensen & Mazaheri, 2010). We find stronger alpha and beta power over left occipital cortex prior to a leftward saccade than prior to a rightward saccade. We believe this lateralized pattern is best explained by considering it a covert precursor to the orienting of overt attention: at any particular foveation point, something interesting might be located in the left visual periphery. Such a stimulus will lead to a spatially specific pattern of alpha power over occipital cortex. In the example case, alpha activity will decrease over the right hemisphere, where the interesting stimulus is

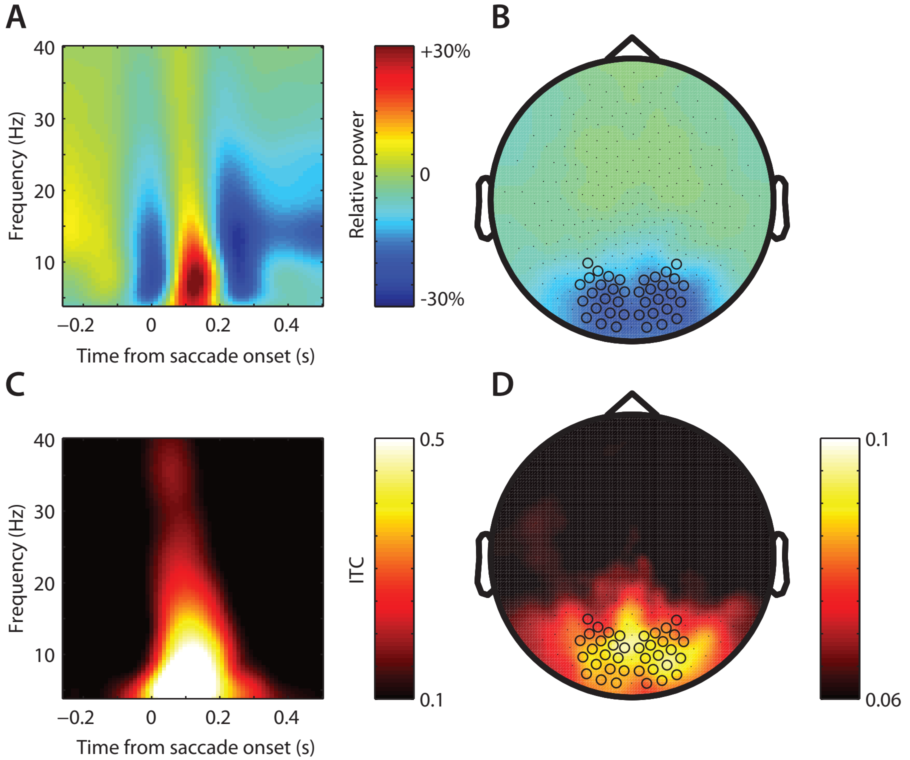

Figure 6.8: Time-frequency representations (TFRs) of power and inter-trial coherence (ITC). **(A)** TFR of power, locked to saccade onset, for the combined planar gradient sensors highlighted in (B). Power is expressed as relative change from a pre-saccadic baseline (-0.3 to -0.1 s peri-saccade). **(B)** Topography for the ˜15 Hz suppression observed around 0.2 0.5 s after saccade onset. **(C)** Absolute ITC around saccade onset. **(D)** Topography for ITC in the same time-frequency window (0.2 0.5 s; ˜15 Hz) as the power topography in (B).

processed; while it will increase over the left hemisphere, in accordance with the functional-inhibition hypothesis. This lateralization might reflect the processing of the interesting stimulus itself, or the brief covert orienting of attention toward it as a precursor to subsequent overt reorienting (i.e., a saccade). This result shows that visual alpha lateralization, previously typically associated with the top-down controlled direction of covert attention following an explicit spatial cue, also occurs during natural viewing.

As a final spatially selective marker dissociating left- from rightward saccades, we found elevated beta power in the medial to right cerebellum prior to a leftward saccade. Although it has been debated to what extent MEG is sensitive to cerebellar sources, various studies have by now shown that cerebellar MEG is feasible (Tesche & Karhu, 2000a; Gross et al., 2002; Dalal et al., 2013). This literature, and the physiologically plausible nature of the sources we observed, demonstrate that our cerebellar findings are not artifactual.

Since saccadic eye movements are very brief, there is not enough time for retinal feedback to guide the movement. Instead, an accurate motor plan is essential for the correct positioning of the eyes. The cerebellum, in particular the part of the posterior vermis known as the oculomotor vermis (Noda & Fujikado, 1987), as well as the caudal fastigial nucleus (CFN), to which the oculomotor vermis projects, is known to be responsible for ensuring that horizontal saccades are fast, accurate, and consistent (Robinson & Fuchs, 2001). Activity in these regions is associated with driving saccades toward the contralateral visual hemifield (Noda et al., 1988). Our observation of elevated beta power over medial/right cerebellum before a leftward saccade is consistent with an activation of this oculomotor vermis-CFN system. It is probably mainly related to the saccadic motor program, rather than to attentional orienting itself (as we interpreted the cortical effects to be).

The analysis of saccade-evoked responses (Figure 6.7, particularly 6.7C) revealed that the saccadic ERF is locked to saccade onset, and not to fixation onset. If the ERF (which shows a profile consistent with the typical P1/N1/P2-response observed after visual stimulus onset (Luck et al., 2000)) were caused by the visual 'stimulus onset' related to fixation onset, one would have expected the ERF to be locked to this event instead. Thus, we can conclude that the arrival of novel visual information after fixation onset cannot (entirely) explain the observed ERF. Two possible explanations remain for the onset-locking of the saccadic ERF: it could reflect the strong visual transient because of eye movement onset (and thus still be primarily of retinal origin), or it could reflect an extraretinal signal related to the initiation of the saccade itself.

On the basis of our current findings, we cannot exclude the possibility of the visual transient related to saccade onset being the primary cause of the ERF. However, it is interesting to entertain the alternative. Visual perception is suppressed during the execution of saccadic eye movements; this well-established phenomenon is known as saccadic suppression (Ross et al., 2001). In contrast, we can easily perceive abrupt changes in visual display, and visual perception is not disrupted during exogenously initiated eye movements. Therefore, saccadic suppression must rely on a form of corollary discharge, by which the visual system is informed of the to-be-executed eye movement and through which perception is temporarily suppressed. It has been proposed that this corollary discharge is also responsible for optimally preparing the visual cortex for the post-saccadic arrival of new sensory information (Melloni et al., 2009). Indeed, recent reports show evidence for the existence of such a mechanism (Rajkai et al., 2008; Bosman et al., 2009; Ito et al., 2011). Our observation that the saccade-locked ERF is strongly locked to saccade onset, rather than offset, is compatible with the view that this ERF reflects a corollary discharge related to saccade initiation.

Previous studies have reported significant post-saccade phase concentration in the theta (Rajkai et al., 2008) and alpha (Bosman et al., 2009; Ito et al., 2011) frequency bands. Such a phase concentration could be the result of a phase reset in ongoing neural oscillations, or it could reflect an evoked component. Although we found a strong increase in phase locking post-saccade, we believe this phase locking is merely a frequency-domain reflection of the saccade-evoked response. Consistent with this interpretation, the TFR of phase locking (Figure 6.8c) reveals that phase locking is broadband and tightly time-locked to the saccade. We note here that MEG has an inherently poorer signal-to-noise ratio than invasive electrophysiological recordings. Therefore, we cannot provide a conclusive answer to the question of whether ongoing neural oscillations are phase reset in response to saccades produced during natural viewing. Further work is needed to fully address this issue.

Taken together, our findings show the following. During visual exploration of natural images, the occipital pattern of alpha activity mirrors the spotlight of attention. A particular visual location might be selected as interesting enough to warrant a reorientation of overt attention. The right posterior parietal cortex is involved in this process. A saccade is initiated, probably through a direct projection from parietal cortex to the superior colliculus, or possibly indirectly through the FEF (Goldberg, 2000; Pierrot-Deseilligny et al., 2004). The cerebellum is involved to ensure a fast and accurate eye movement. Prior to the end of the saccade (i.e., the start of the new fixation), a response is already underway in visual cortex, possibly reflecting a prediction of what new visual input the saccade will provide (Friston et al., 2012).

CHAPTER 7

Discussion

With the work presented in this thesis, I have attempted to contribute to our understanding of the role that alpha oscillations in the visual system play in the structuring of neural information processing. I set out to anwer the following three questions: First, to what extent is the involvement of alpha oscillations in the structuring of visual perception causal, as opposed to merely correlational? Second, by what network mechanisms do alpha oscillations modulate the neural processing of visual information? And third, does the modulation of alpha activity constitute a general cognitive mechanism, or is it limited to a specific experimental setting? In this Chapter, I discuss how my empirical findings relate to these three core questions. It should be noted that in the empirical chapters themselves, several additional findings, less related to the core questions of this thesis, were reported. These findings are discussed in the individual chapters, and this discussion is not repeated here.

7.1 Overview and interpretation of core findings

In Chapter 2, I showed that alpha oscillations can become entrained to external stimuli, thus allowing a direct manipulation of alpha activity, without an associated cognitive cue. The entrained alpha oscillations persisted after the external stimuli were switched off, thus demonstrating that the alpha activity is maintained endogenously by the brain. This was confirmed by source analysis, which showed that the generators of the entrained alpha were located in early visual cortex. Importantly, the entrained alpha activity had consequences for perception: subjects were better at detecting a near-threshold target at certain phases of the alpha cycle than at others, an effect which also persisted after the offset of the entraining stimuli.

The results of Chapter 2 show that alpha activity is causally responsible for these perceptual modulations, since in the experiment reported there I directly manipulated alpha oscillations without any causal intermediary. This is in contrast to the majority of studies on alpha oscillations in attention: typically, a cue is presented to subjects, instructing them to covertly direct their attention to one part of visual space (in the most common case of a study on visuospatial attention). Subsequently, visual alpha activity will display a spatially specific pattern in anticipation to some stimulus, and this pattern is predictive of behavioural performance. Although this commonly observed correlation is interesting, by itself it does not demonstrate that alpha oscillations are responsible for the behavioural effect. Both the modulations in the alpha band and the behaviour could be consequences of some other neural mechanism, thus reducing alpha activity to an epiphenomenon. To test this explanation, in Chapter 2, alpha was manipulated directly, and a behavioural effect was observed. Therefore, the association between alpha and visual perception is not epiphenomenal. This conclusion is in line with previous reports based on transcranial magnetic stimulation (Romei et al., 2010; Thut et al., 2011).

In Chapter 3, I investigated the neural mechanisms that might underly the role that alpha activity plays in modulating perception. Using data recorded from a laminar electrode spanning all layers of monkey primary visual cortex, I showed that, on such a fine neural scale, gamma activity interacts with the alpha rhythm on two timescales. First, the amplitude of gamma is negatively correlated with the amplitude of alpha, on a timescale of several seconds. Second, gamma activity is locked to the phase of the alpha rhythm, an association on the timescale of < 100 ms. The sources of alpha were located in the deep cortical layers, most likely layer 5, while gamma activity was most prominent in the granular and supragranular layers. This separation of low- and high-frequency activity within the cortical column is in agreement with previous reports (Bollimunta et al., 2008; Maier et al., 2010), and Chapter 3 now for the first time demonstrates the interacting nature of these different processes.

Coupling between alpha phase and gamma amplitude within the cortical column provides a potential mechanism by which alpha activity might be associated with visual perception. Gamma activity is typically associated with active processing of information; specifically, gamma band synchronization in a cortical area is thought to be an effective mechanism for driving other areas located downstream in the cortical hierarchy (Salinas & Sejnowski, 2001; Fries et al., 2007; Fries, 2009). In contrast to gamma, which is primarily observed during stimulus processing (Jensen et al., 2007), modulations of alpha activity can be observed also without stimulation, and are therefore thought to be under top-down control; specifically, they are thought to reflect the functional inhibition of sensory regions (Klimesch et al., 2007; Thut & Miniussi, 2009; Jensen et al., 2012). It is interesting to note that recent studies have shown that spike-field coherence in the alpha band is reduced with attention specifically in the deeper cortical layers, while gamma band synchronization is enhanced specifically in the superficial layers (Buffalo et al., 2011). If alpha reflects top-down controlled functional inhibition, and gamma reflects bottom-up stimulus processing and drives downstream brain regions, one effective way in which alpha might achieve its modulation of neural processing is through locally interacting with gamma. In Chapter 3, we found evidence for the existence of such a mechanism.

Chapter 4 took us into even smaller territory. In it, I asked what cellular network mechanisms could be responsible for implementing phase-amplitude coupling between slow and fast oscillations, as observed in Chapter 3. To answer this question, I turned to the interaction between gamma and the hippocampal theta rhythm, as the physiology underlying this rhythm is better understood than that underlying alpha. After constructing and analyzing a biophysically realistic computational model, I found that the likely route through which the phase of low-frequency activity can influence the amplitude of high-frequency activity is through a projection onto fast-spiking interneurons. This result was shown not to be limited to theta oscillations, but could equally well apply to alpha activity.

Of course, the results presented in Chapter 4 do not conclusively demonstrate that, in vivo, the alpha rhythm modulates gamma through an interaction with the fast-spiking inhibitory interneurons. However, such a mechanism is raised as an interesting possibility, which can be tested empirically. The results presented in Chapters 3 and 4 can be integrated in the light of this possibility. In Chapter 3, we reported that layer 5 pyramidal cells are the most likely source of the alpha rhythm responsible for modulating the gamma activity. It is known that these cells project to inhibitory interneurons in the same layer (Kapfer et al., 2007; Silberberg & Markram, 2007), which in turn project to the superficial layers (Dantzker & Callaway, 2000; Xu & Callaway, 2009; Iurilli et al., 2012), the layers which show the strongest gamma activity. Taken together, alpha activity in deeper layers of neocortex could influence gamma activity in superficial layers (and, thereby, the processing of visual information) through an interaction with the fast-spiking interneurons underlying gamma rhythm generation.

After the excursion into the physiology of the cortical column (Chapter 3) and the dynamics of a biophysical network only a few hundred cells large (Chapter 4), in the subsequent chapters we returned to the domain of human cognition. In Chapter 5, I demonstrated that a spatially specific modulation of alpha band activity is present when subjects are engaged in a visual search task. Specifically, when a target amongst distractors was presented in the left visual hemifield, alpha power was increased in the left occipital cortex, and decreased in the right. The reverse held when the target was present in the right visual hemifield. This modulation mirrors the 'classical' alpha lateralization typically observed following an explicit spatial cue. The extent of the observed alpha modulation predicted subsequent search performance, and was observed before subjects had consciously identified the target.

For Chapter 6, I studied the relationship between alpha activity and the free viewing of natural images. I demonstrated that, during such free visual exploration, a spatially specific pattern of parietal and occipital alpha activity can be observed prior to a saccadic eye movement. The occipital alpha pattern might reflect a brief shift in covert attention in response to an interesting stimulus in the visual periphery. The associated parietal alpha activity might reflect the subsequent reorienting of overt attention and the initiation of a saccade. Thus, during natural viewing, the pattern of alpha activity over posterior cortical regions mirrors the rapidly shifting spotlight of attention.

As mentioned previously, the bulk of evidence in the literature concerning the modulation of alpha activity with attention is based on explicit spatial cues presented to subjects who are not allowed to move their eyes. While such evidence has been hugely instructive, it has left open the question of whether modulations of alpha also occur in more ecologically valid settings. Neither of the experiments performed in Chapters 5 and 6 employed an explicit spatial cue, yet in both we observed spatially specific modulations of alpha band activity. Taken together, these last two chapters have shown that the modulation of alpha activity in order to structure and prioritize visual information processing is probably a general neural mechanism and not limited to more or less artificial experimental conditions. The results are consistent with alpha activity serving as a gain control of neural processing in everyday life.

7.2 General conclusion

Taking all these findings together, how do they answer the three core questions posed in the introduction and repeated above? First, is alpha causally involved in structuring visual perception, or is this involvement merely correlational? Yes, alpha activity plays a causal role for visual perception. Second, by what network mechanisms does alpha activity fulfil its role in structuring information processing? Through a cortically local interaction with gamma activity, involving the fast-spiking inhibitory interneurons. Third, to what extent does a modulation of alpha activity subserve everyday cognition, or is this phenomenon restricted to specific experimental settings? Alpha is involved in preparing the brain for upcoming stimuli during visual search, and in preparing overt (saccadic) shifts of attention during free visual exploration.

Summarizing, the work in this thesis has shed light on various aspects of the hypothesis that alpha oscillations serve to structure and prioritize neural information processing in the visual system, and comprises evidence in favour of this hypothesis. Thereby, this thesis has taken one step further towards the "principled displacement of folk psychology" (see Chapter 1) in favour of understanding the basis of cognition in truly mechanistic terms.

Back matter

References

Anderson, E. J., Jones, D. K., O'Gorman, R. L., Leemans, A., Catani, M., & Husain, M. (2012). Cortical network for gaze control in humans revealed using multimodal MRI. *Cerebral Cortex*, *22*(4), 765–775.

Arnal, L. H., & Giraud, A.-L. (2012). Cortical oscillations and sensory predictions. *Trends in Cognitive Sciences*, *16*(7), 390–398.

Axmacher, N., Henseler, M. M., Jensen, O., Weinreich, I., Elger, C., & Fell, J. (2010). Cross-frequency coupling supports multi-item working memory in the human hippocampus. *Proceedings of the National Academy of Sciences*, *107*(7), 3228.

Bar, M. (2004). Visual objects in context. *Nature Reviews Neuroscience*, *5*(8), 617–629.

Baranauskas, G., Maggiolini, E., Vato, A., Angotzi, G., Bonfanti, A., Zambra, G., ... Fadiga, L. (2012). Origins of 1/F2 scaling in the power spectrum of intracortical local field potential. *Journal of Neurophysiology*, *107*(3), 984–994.

Bartels, A., & Zeki, S. (2004). The neural correlates of maternal and romantic love. *Neuroimage*, *21*(3), 1155–1166.

Bartos, M., Vida, I., Frotscher, M., Geiger, J. R. P., & Jonas, P. (2001). Rapid signaling at inhibitory synapses in a dentate gyrus interneuron network. *Journal of Neuroscience*, *21*(8), 2687.

Bartos, M., Vida, I., Frotscher, M., Meyer, A., Monyer, H., Geiger, J. R. P., & Jonas, P. (2002). Fast synaptic inhibition promotes synchronized gamma oscillations in hippocampal interneuron networks. *Proceedings of the National Academy of Sciences*, *99*(20), 13222–13227.

Bartos, M., Vida, I., & Jonas, P. (2007). Synaptic mechanisms of synchronized gamma oscillations in inhibitory interneuron networks. *Nature Reviews Neuroscience*, *8*(1), 45–56.

Bastiaansen, M. C., & Knsche, T. R. (2000). Tangential derivative mapping of axial MEG applied to event-related desynchronization research. *Clinical Neurophysiology*, *111*(7), 1300–1305.

Bauer, M., Kluge, C., Bach, D., Bradbury, D., Heinze, H. J., Dolan, R. J., & Driver, J. (2012). Cholinergic enhancement of visual attention and neural oscillations in the human brain. *Current Biology*, *22*(5), 397–402.

Bédard, C., Kröger, H., & Destexhe, A. (2004). Modeling extracellular field potentials and the Frequency-Filtering properties of extracellular space. *Biophysical Journal*, *86*(3), 1829–1842.

Bédard, C., Kröger, H., & Destexhe, A. (2006). Does the 1/f frequency scaling of brain signals reflect self-organized critical states? *Physical Review Letters*, *97*(11), 118102.

Bell, A. J., & Sejnowski, T. J. (1995). An information-maximization approach to blind separation and blind deconvolution. *Neural Computation*, *7*(6), 1129–1159.

Belluscio, M. A., Mizuseki, K., Schmidt, R., Kempter, R., & Buzski, G. (2012). Cross-frequency phase-phase coupling between theta and gamma oscillations in the hippocampus. *Journal of Neuroscience*, *32*(2), 423–435.

Berkeley, G. (1710). *A treatise concerning the principles of human knowledge.* (Public Domain, Project Gutenberg, book ID 4723.)

Bernander, j., Koch, C., & Usher, M. (1994). The effect of synchronized inputs at the single neuron level. *Neural Computation*, *6*(4), 622–641.

Biederman, I. (1972). Perceiving real-world scenes. *Science*, *177*(4043), 77–80.

Bollimunta, A., Chen, Y., Schroeder, C. E., & Ding, M. (2008). Neuronal mechanisms of cortical alpha oscillations in awake-behaving macaques. *Journal of Neuroscience*, *28*(40), 9976–9988.

Bollimunta, A., Mo, J., Schroeder, C. E., & Ding, M. (2011). Neuronal mechanisms and attentional modulation of corticothalamic alpha oscillations. *Journal of Neuroscience*, *31*(13), 4935 –4943.

Bonnefond, M., & Jensen, O. (2012). Alpha oscillations serve to protect working memory maintenance against anticipated distracters. *Current Biology*, *22*(20), 1969–1974.

Börgers, C., & Kopell, N. (2003). Synchronization in networks of excitatory and inhibitory neurons with sparse, random connectivity. *Neural Computation*, *15*(3), 509–538.

Bosman, C. A., Womelsdorf, T., Desimone, R., & Fries, P. (2009). A microsaccadic rhythm modulates gamma-band synchronization and behavior. *Journal of Neuroscience*, *29*(30), 9471–9480.

Brainard, D. H. (1997). The psychophysics toolbox. *Spatial Vision*, *10*(4), 433–436.

Brunet, N., Bosman, C. A., Roberts, M., Oostenveld, R., Womelsdorf, T., Weerd, P. D., & Fries, P. (2013). Visual cortical gamma-band activity during free viewing of natural images. *Cerebral Cortex*, bht280.

Buffalo, E. A., Fries, P., Landman, R., Buschman, T. J., & Desimone, R. (2011). Laminar differences in gamma and alpha coherence in the ventral stream. *Proceedings of the National Academy of Sciences*, *108*(27), 11262 –11267.

Buhl, E. H., Cobb, S. R., Halasy, K., & Somogyi, P. (1995). Properties of unitary IPSPs evoked by anatomically identified basket cells in the rat hippocampus. *European Journal of Neuroscience*, *7*(9), 1989–2004.

Buhl, E. H., Tams, G., & Fisahn, A. (1998). Cholinergic activation and tonic excitation induce persistent gamma oscillations in mouse somatosensory cortex in vitro. *Journal of Physiology*, *513*(1), 117–126.

Busch, N., Dubois, J., & VanRullen, R. (2009). The phase of ongoing eeg oscillations predicts visual perception. *Journal of Neuroscience*, *29*(24), 7869–7876.

Busch, N. A., Dubois, J., & VanRullen, R. (2009). The phase of ongoing EEG oscillations predicts visual perception. *Journal of Neuroscience*, *29*(24), 7869–7876.

Buzsáki, G. (2002). Theta oscillations in the hippocampus. *Neuron*, *33*(3), 325–340.

Buzsáki, G. (2006). *Rhythms of the brain*. Oxford: Oxford University Press.

Buzsáki, G., & Draguhn, A. (2004). Neuronal oscillations in cortical networks. *Science*, *304*(5679), 1926–1929.

Buzsáki, G., & Moser, E. I. (2013). Memory, navigation and theta rhythm in the hippocampal-entorhinal system. *Nature Neuroscience*, *16*(2), 130–138.

Callaway, E. M. (2004). Feedforward, feedback and inhibitory connections in primate visual cortex. *Neural Networks*, *17*(56), 625–632.

Canolty, R. T., Edwards, E., Dalal, S. S., Soltani, M., Nagarajan, S. S., Kirsch, H. E., … Knight, R. T. (2006). High gamma power is phase-locked to theta oscillations in human neocortex. *Science*, *313*(5793), 1626–1628.

Canolty, R. T., & Knight, R. T. (2010). The functional role of cross-frequency coupling. *Trends in Cognitive Sciences*, *14*(11), 506–515.

Capilla, A., Pazo-Alvarez, P., Darriba, A., Campo, P., & Gross, J. (2011). Steady-state visual evoked potentials can be explained by temporal superposition of transient event-related responses. *PLoS ONE*, *6*(1), e14543.

Capotosto, P., Babiloni, C., Romani, G. L., & Corbetta, M. (2009). Frontoparietal cortex controls spatial attention through modulation of anticipatory alpha rhythms. *Journal of Neuroscience*, *29*(18), 5863–5872.

Capotosto, P., Babiloni, C., Romani, G. L., & Corbetta, M. (2012). Differential contribution of right and left parietal cortex to the control of spatial attention: a simultaneous EEG-rTMS study. *Cerebral Cortex*, *22*(2), 446–454.

Cardin, J. A., Carlén, M., Meletis, K., Knoblich, U., Zhang, F., Deisseroth, K., …

Moore, C. I. (2009). Driving fast-spiking cells induces gamma rhythm and controls sensory responses. *Nature*, *459*(7247), 663–667.

Chance, F. S., Abbott, L. F., & Reyes, A. D. (2002). Gain modulation from background synaptic input. *Neuron*, *35*(4), 773–782.

Chrobak, J. J., & Buzski, G. (1998). Gamma oscillations in the entorhinal cortex of the freely behaving rat. *Journal of Neuroscience*, *18*(1), 388–398.

Chun, M. M., & Jiang, Y. (1998). Contextual cueing: Implicit learning and memory of visual context guides spatial attention. *Cognitive Psychology*, *36*(1), 28–71.

Churchland, P. M. (1981). Eliminative materialism and the propositional attitudes. *Journal of Philosophy*, *78*(2), 67–90.

Colby, C. L., & Goldberg, M. E. (1999). Space and attention in parietal cortex. *Annual Review of Neuroscience*, *22*(1), 319–349.

Colgin, L. L., Denninger, T., Fyhn, M., Hafting, T., Bonnevie, T., Jensen, O., … Moser, E. I. (2009). Frequency of gamma oscillations routes flow of information in the hippocampus. *Nature*, *462*(7271), 353–357.

Corbetta, M., & Shulman, G. L. (2002). Control of goal-directed and stimulus-driven attention in the brain. *Nature Reviews Neuroscience*, *3*(3), 201–215.

Cousineau, D. (2005). Confidence intervals in within-subjects designs: A simpler solution to loftus and masson's method. *Tutorials in Quantitative Methods for Psychology*, *1*, 42–45.

Cravo, A. M., Rohenkohl, G., Wyart, V., & Nobre, A. C. (2013). Temporal expectation enhances contrast sensitivity by phase entrainment of low-frequency oscillations in visual cortex. *Journal of Neuroscience*, *33*(9), 4002–4010.

Csicsvari, J., Jamieson, B., Wise, K. D., & Buzski, G. (2003). Mechanisms of gamma oscillations in the hippocampus of the behaving rat. *Neuron*, *37*(2), 311–322.

Cunningham, M. O., Davies, C. H., Buhl, E. H., Kopell, N., & Whittington, M. A. (2003). Gamma oscillations induced by kainate receptor activation in the entorhinal cortex in vitro. *Journal of Neuroscience*, *23*(30), 9761–9769.

Dalal, S. S., Osipova, D., Bertrand, O., & Jerbi, K. (2013). Oscillatory activity of the human cerebellum: The intracranial electrocerebellogram revisited. *Neuroscience & Biobehavioral Reviews*, *37*(4), 585–593.

Dantzker, J. L., & Callaway, E. M. (2000). Laminar sources of synaptic input to cortical inhibitory interneurons and pyramidal neurons. *Nature Neuroscience*, *3*(7), 701–707.

Dégenètais, E., Thierry, A. M., Glowinski, J., & Gioanni, Y. (2003). Synaptic influence of hippocampus on pyramidal cells of the rat prefrontal cortex: an in vivo intracellular recording study. *Cerebral Cortex*, *13*(7), 782–792.

de Graaf, T. A., Gross, J., Paterson, G., Rusch, T., Sack, A. T., & Thut, G. (2013). Alpha-band rhythms in visual task performance: Phase-locking by rhythmic sensory stimulation. *PLoS ONE*, *8*(3), e60035.

de Lange, F. P., Rahnev, D. A., Donner, T. H., & Lau, H. (2013). Prestimulus oscillatory activity over motor cortex reflects perceptual expectations. *Journal of Neuroscience*, *33*(4), 1400–1410.

Dolan, R. J., & Fletcher, P. C. (1997). Dissociating prefrontal and hippocampal function in episodic memory encoding. *Nature*, *388*, 582–585.

Donner, T. H., Siegel, M., Fries, P., & Engel, A. K. (2009). Buildup of choice-predictive activity in human motor cortex during perceptual decision making. *Current Biology*, *19*(18), 1581–1585.

Dougherty, E. R. (1992). *An introduction to morphological image processing*. Bellingham, WA, USA: SPIE Optical Engineering Press.

Dugué, L., Marque, P., & VanRullen, R. (2011). The phase of ongoing oscillations mediates the causal relation between brain excitation and visual perception. *Journal of Neuroscience*, *31*(33), 11889–11893.

Eichenbaum, H. (2000). A cortical-hippocampal system for declarative memory. *Nature Reviews Neuroscience*, *1*, 41–50.

Eichenbaum, H., & Cohen, N. (2014). Can we reconcile the declarative memory and spatial navigation views on hippocampal function? *Neuron*, *83*(4), 764–770.

Enns, J. T., & Lleras, A. (2008). What's next? new evidence for prediction in human vision. *Trends in Cognitive Sciences*, *12*(9), 327–333.

Fiebelkorn, I. C., Saalmann, Y. B., & Kastner, S. (2013). Rhythmic sampling within and between objects despite sustained attention at a cued location. *Current Biology*, *23*(24), 2553–2558.

Fox, J. (1997). *Applied regression analysis, linear models, and related methods*. SAGE.

Francken, J. C., & Slors, M. (2014). From commonsense to science, and back: The use of cognitive concepts in neuroscience. *Consciousness and Cognition*, *29*, 248–258.

Fries, P. (2005). A mechanism for cognitive dynamics: neuronal communication through neuronal coherence. *Trends in Cognitive Sciences*, *9*(10), 474–480.

Fries, P. (2009). Neuronal gamma-band synchronization as a fundamental process in cortical computation. *Annual Review of Neuroscience*, *32*(1), 209–224.

Fries, P., Nikolić, D., & Singer, W. (2007). The gamma cycle. *Trends in Neurosciences*, *30*(7), 309–316.

Fries, P., Reynolds, J. H., Rorie, A. E., & Desimone, R. (2001). Modulation of oscillatory neuronal synchronization by selective visual attention. *Science*, *291*(5508), 1560–1563.

Friston, K., Adams, R. A., Perrinet, L., & Breakspear, M. (2012). Perceptions as hypotheses: Saccades as experiments. *Frontiers in Psychology*, *3*, 151.

Gabbiani, F., Midtgaard, J., & Knopfel, T. (1994). Synaptic integration in a model of cerebellar granule cells. *Journal of Neurophysiology*, *72*(2), 999–1009.

Gabbott, P., Headlam, A., & Busby, S. (2002). Morphological evidence that CA1 hippocampal afferents monosynaptically innervate PV-containing neurons and NADPH-diaphorase reactive cells in the medial prefrontal cortex (areas 25/32) of the rat. *Brain Research*, *946*(2), 314–322.

Galarreta, M., & Hestrin, S. (1999). A network of fast-spiking cells in the neocortex connected by electrical synapses. *Nature*, *402*, 72–75.

Gibson, J. R., Beierlein, M., & Connors, B. W. (1999). Two networks of electrically coupled inhibitory neurons in neocortex. *Nature*, *402*, 75–79.

Gloveli, T., Dugladze, T., Saha, S., Monyer, H., Heinemann, U., Traub, R., … Buhl, E. (2005). Differential involvement of oriens/pyramidale interneurones in hippocampal network oscillations in vitro. *Journal of Physiology*, *562*(1), 131–147.

Goldberg, M. E. (2000). The control of gaze. In *Principles of neural science*. New York: McGraw-Hill.

Gray, C. M., König, P., Engel, A. K., & Singer, W. (1989). Oscillatory responses in cat visual cortex exhibit inter-columnar synchronization which reflects global stimulus properties. *Nature*, *338*(6213), 334–337.

Gray, C. M., & Singer, W. (1989). Stimulus-specific neuronal oscillations in orientation columns of cat visual cortex. *Proceedings of the National Academy of Sciences*, *86*(5), 1698–1702.

Gross, J., Kujala, J., Hmlinen, M., Timmermann, L., Schnitzler, A., & Salmelin, R. (2001). Dynamic imaging of coherent sources: Studying neural interactions in the human brain. *Proceedings of the National Academy of Sciences*, *98*(2), 694–699.

Gross, J., Timmermann, L., Kujala, J., Dirks, M., Schmitz, F., Salmelin, R., & Schnitzler, A. (2002). The neural basis of intermittent motor control in humans. *Proceedings of the National Academy of Sciences*, *99*(4), 2299–2302.

Haegens, S., Händel, B. F., & Jensen, O. (2011). Top-down controlled alpha band activity in somatosensory areas determines behavioral performance in a discrimination task. *Journal of Neuroscience*, *31*(14), 5197 –5204.

Haegens, S., Nácher, V., Luna, R., Romo, R., & Jensen, O. (2011). Alpha oscillations in the monkey sensorimotor network influence discrimination performance by rhythmical inhibition of neuronal spiking. *Proceedings of the National Academy of Sciences*, *108*(48), 19377 –19382.

Hafting, T., Fyhn, M., Molden, S., Moser, M.-B., & Moser, E. I. (2005). Microstructure of a spatial map in the entorhinal cortex. *Nature*, *436*(7052), 801–806.

Halbleib, A., Gratkowski, M., Schwab, K., Ligges, C., Witte, H., & Haueisen, J. (2012). Topographic analysis of engagement and disengagement of neural oscillators in photic driving: a combined electroencephalogram/magnetoencephalogram study. *Journal of Clinical Neurophysiology*, *29*(1), 33–41.

Händel, B., Haarmeier, T., & Jensen, O. (2011). Alpha oscillations correlate with the successful inhibition of unattended stimuli. *Journal of Cognitive Neuroscience*, *23*(9), 2494–2502.

Händel, B. F., Haarmeier, T., & Jensen, O. (2011). Alpha oscillations correlate with the successful inhibition of unattended stimuli. *Journal of Cognitive Neuroscience*, *23*(9), 2494–2502.

Hanslmayr, S., Aslan, A., Staudigl, T., Klimesch, W., Herrmann, C. S., & Buml, K.-H. (2007). Prestimulus oscillations predict visual perception performance between and within subjects. *Neuroimage*, *37*(4), 1465–1473.

Hanslmayr, S., Volberg, G., Wimber, M., Dalal, S., & Greenlee, M. (2013). Prestimulus oscillatory phase at 7hz gates cortical information flow and visual perception. *Current Biology*, *23*(22), 2273–2278.

Hari, R., & Salmelin, R. (1997). Human cortical oscillations: a neuromagnetic view through the skull. *Trends in Neurosciences*, *20*(1), 44–49.

Harris, K. D., Henze, D. A., Hirase, H., Leinekugel, X., Dragoi, G., Czurkó, A., & Buzsáki, G. (2002). Spike train dynamics predicts theta-related phase precession in hippocampal pyramidal cells. *Nature*, *417*, 738–741.

Hasenstaub, A., Shu, Y., Haider, B., Kraushaar, U., Duque, A., & McCormick, D. A. (2005). Inhibitory postsynaptic potentials carry synchronized frequency information in active cortical networks. *Neuron*, *47*(3), 423–435.

Heilman, K. M., & Abell, T. V. D. (1980). Right hemisphere dominance for attention the mechanism underlying hemispheric asymmetries of inattention (neglect). *Neurology*, *30*(3), 327–327.

Henry, M. J., & Obleser, J. (2012). Frequency modulation entrains slow neural oscillations and optimizes human listening behavior. *Proceedings of the National Academy of Sciences*, *109*(49), 20095–20100.

Herrmann, C. S. (2001). Human EEG responses to 1-100 hz flicker: resonance phenomena in visual cortex and their potential correlation to cognitive phenomena. *Experimental Brain Research*, *137*(3-4), 346–353.

Hines, M. L., & Carnevale, N. T. (1997). The NEURON simulation environment. *Neural Computation*, *9*(6), 1179–1209.

Hirase, H., Leinekugel, X., Czurkó, A., Csicsvari, J., & Buzsáki, G. (2001). Firing rates of hippocampal neurons are preserved during subsequent sleep episodes and modified by novel awake experience. *Proceedings of the National Academy of Sciences*, *98*(16), 9386.

Hodgkin, A. L., & Huxley, A. F. (1952). A quantitative description of membrane current and its applications to conduction and excitation in nerve. *Journal of Physiology*, *117*, 500–544.

Ito, J., Maldonado, P., Singer, W., & Grn, S. (2011). Saccade-related modulations of neuronal excitability support synchrony of visually elicited spikes. *Cerebral Cortex*, *21*(11), 2482–2497.

Iurilli, G., Ghezzi, D., Olcese, U., Lassi, G., Nazzaro, C., Tonini, R., … Medini, P. (2012). Sound-driven synaptic inhibition in primary visual cortex. *Neuron*, *73*(4), 814–828.

Izhikevich, E. (2004). Which model to use for cortical spiking neurons? *IEEE Transactions on Neural Networks*, *15*(5), 1063 –1070.

Jaegle, A., & Ro, T. (2014). Direct control of visual perception with phase-specific modulation of posterior parietal cortex. *Journal of cognitive neuroscience*, *26*(2), 422–432.

James, W. (1890). *The principles of psychology*. New York: Holt.

Jensen, O., Bonnefond, M., & VanRullen, R. (2012). An oscillatory mechanism for prioritizing salient unattended stimuli. *Trends in Cognitive Sciences*, *16*(4), 200–206.

Jensen, O., Gelfand, J., Kounios, J., & Lisman, J. E. (2002). Oscillations in the alpha band (912 hz) increase with memory load during retention in a short-term memory task. *Cerebral Cortex*, *12*(8), 877–882.

Jensen, O., Gips, B., Bergmann, T. O., & Bonnefond, M. (2014). Temporal coding organized by coupled alpha and gamma oscillations prioritize visual processing. *Trends in Neurosciences*, *37*(7), 357–369.

Jensen, O., Kaiser, J., & Lachaux, J. P. (2007). Human gamma-frequency oscillations associated with attention and memory. *Trends in Neurosciences*, *30*(7), 317–324.

Jensen, O., & Mazaheri, A. (2010). Shaping functional architecture by oscillatory alpha activity: gating by inhibition. *Frontiers in Human Neuroscience*, *4*, 186.

JONES, M. W., & WILSON, M. A. (2005). Phase precession of medial prefrontal cortical activity relative to the hippocampal theta rhythm. *Hippocampus*, *15*(7), 867–873.

JUNG, T. P., MAKEIG, S., HUMPHRIES, C., LEE, T. W., MCKEOWN, M. J., IRAGUI, V., & SEJNOWSKI, T. J. (2000). Removing electroencephalographic artifacts by blind source separation. *Psychophysiology*, *37*(2), 163–178.

JUNG, T.-P., MAKEIG, S., WESTERFIELD, M., TOWNSEND, J., COURCHESNE, E., & SEJNOWSKI, T. J. (2001). Analysis and visualization of single-trial event-related potentials. *Human Brain Mapping*, *14*(3), 166–185.

JUNGÉ, J. A., BRADY, T. F., & CHUN, M. M. (2009). The contents of perceptual hypotheses: evidence from rapid resumption of interrupted visual search. *Attention, Perception & Psychophysics*, *71*(4), 681–689.

JUTRAS, M. J., FRIES, P., & BUFFALO, E. A. (2013). Oscillatory activity in the monkey hippocampus during visual exploration and memory formation. *Proceedings of the National Academy of Sciences*, *110*(32), 13144–13149.

KAHANA, M. J., SEELIG, D., & MADSEN, J. R. (2001). Theta returns. *Current Opinion in Neurobiology*, *11*(6), 739–744.

KAPFER, C., GLICKFELD, L. L., ATALLAH, B. V., & SCANZIANI, M. (2007). Supralinear increase of recurrent inhibition during sparse activity in the somatosensory cortex. *Nature Neuroscience*, *10*(6), 743–753.

KELLY, S. P., LALOR, E. C., REILLY, R. B., & FOXE, J. J. (2006). Increases in alpha oscillatory power reflect an active retinotopic mechanism for distracter suppression during sustained visuospatial attention. *Journal of Neurophysiology*, *95*(6), 3844–3851.

KLEPPE, I. C., & ROBINSON, H. P. C. (1999). Determining the activation time course of synaptic AMPA receptors from openings of colocalized NMDA receptors. *Biophysical Journal*, *77*(3), 1418–1427.

KLIMESCH, W., SAUSENG, P., & HANSLMAYR, S. (2007). EEG alpha oscillations: the inhibition-timing hypothesis. *Brain Research Reviews*, *53*(1), 63–88.

KOPELL, N., & ERMENTROUT, B. (2004). Chemical and electrical synapses perform complementary roles in the synchronization of interneuronal networks. *Proceedings of the National Academy of Sciences*, *101*(43), 15482–15487.

LAKATOS, P., KARMOS, G., MEHTA, A. D., ULBERT, I., & SCHROEDER, C. E. (2008). Entrainment of neuronal oscillations as a mechanism of attentional selection. *Science*, *320*(5872), 110–113.

LAKATOS, P., SHAH, A. S., KNUTH, K. H., ULBERT, I., KARMOS, G., & SCHROEDER, C. E. (2005). An oscillatory hierarchy controlling neuronal excitability and stimulus processing in the auditory cortex. *Journal of Neurophysiology*, *94*(3), 1904–1911.

LANDAU, A. N., & FRIES, P. (2012). Attention samples stimuli rhythmically. *Current Biology*, *22*(11), 1000–1004.

LAVENEX, P., & AMARAL, D. G. (2000). Hippocampal-neocortical interaction: a hierarchy of associativity. *Hippocampus*, *10*(4).

LILEY, D. T. J., & WRIGHT, J. J. (1994). Intracortical connectivity of pyramidal and stellate cells: estimates of synaptic densities and coupling symmetry. *Network: Computation in Neural Systems*, *5*(2), 175–189.

LIN, S., GERVASONI, D., & NICOLELIS, M. (2006). Fast modulation of prefrontal cortex activity by basal forebrain noncholinergic neuronal ensembles. *Journal of Neurophysiology*, *96*(6), 3209.

LISMAN, J. E., & JENSEN, O. (2013). The theta-gamma neural code. *Neuron*, *77*(6), 1002–1016.

LLERAS, A., RENSINK, R. A., & ENNS, J. T. (2005). Rapid resumption of interrupted visual search. new insights on the interaction between vision and memory. *Psychological Science*, *16*(9), 684–688.

LLERAS, A., RENSINK, R. A., & ENNS, J. T. (2007). Consequences of display changes during interrupted visual search: rapid resumption is target specific. *Perception & Psychophysics*, *69*(6), 980–993.

LOPES DA SILVA, F., & STORM VAN LEEUWEN, W. (1977). The cortical source of the alpha rhythm. *Neuroscience Letters*, *6*(23), 237–241.

LOPES DA SILVA, F. H., VOS, J. E., MOOIBROEK, J., & VAN ROTTERDAM, A. (1980). Relative contributions of intracortical and thalamo-cortical processes in the generation of alpha rhythms, revealed by partial coherence analysis. *Electroencephalography and Clinical Neurophysiology*, *50*(5-6), 449–456.

Lorincz, M. L., Kkesi, K. A., Juhsz, G., Crunelli, V., & Hughes, S. W. (2009). Temporal framing of thalamic relay-mode firing by phasic inhibition during the alpha rhythm. *Neuron*, *63*(5), 683–696.

Luck, S. J., Woodman, G. F., & Vogel, E. K. (2000). Event-related potential studies of attention. *Trends in Cognitive Sciences*, *4*(11), 432–440.

Lütkenhöner, B. (2003). Magnetoencephalography and its achilles' heel. *Journal of Physiology, Paris*, *97*(4-6), 641–658.

Maier, A., Adams, G. K., Aura, C., & Leopold, D. A. (2010). Distinct superficial and deep laminar domains of activity in the visual cortex during rest and stimulation. *Frontiers in Systems Neuroscience*, *4*(31), 1–11.

Maier, A., Aura, C. J., & Leopold, D. A. (2011). Infragranular sources of sustained local field potential responses in macaque primary visual cortex. *Journal of Neuroscience*, *31*(6), 1971 –1980.

Maris, E., & Oostenveld, R. (2007). Nonparametric statistical testing of EEG- and MEG-data. *Journal of Neuroscience Methods*, *164*(1), 177–190.

Mathewson, K. E., Gratton, G., Fabiani, M., Beck, D. M., & Ro, T. (2009). To see or not to see: prestimulus alpha phase predicts visual awareness. *Journal of Neuroscience*, *29*(9), 2725–2732.

Mathewson, K. E., Lleras, A., Beck, D. M., Fabiani, M., Ro, T., & Gratton, G. (2011). Pulsed out of awareness: EEG alpha oscillations represent a pulsed-inhibition of ongoing cortical processing. *Frontiers in Psychology*, *2*.

Mathewson, K. E., Prudhomme, C., Fabiani, M., Beck, D. M., Lleras, A., & Gratton, G. (2012). Making waves in the stream of consciousness: Entraining oscillations in EEG alpha and fluctuations in visual awareness with rhythmic visual stimulation. *Journal of Cognitive Neuroscience*, *24*(12), 2321–2333.

Mazzoni, A., Whittingstall, K., Brunel, N., Logothetis, N. K., & Panzeri, S. (2010). Understanding the relationships between spike rate and delta/gamma frequency bands of LFPs and EEGs using a local cortical network model. *Neuroimage*, *52*(3), 956–972.

McClure, S. M., Li, J., Tomlin, D., Cypert, K. S., Montague, L. M., & Montague, P. R. (2004). Neural correlates of behavioral preference for culturally familiar drinks. *Neuron*, *44*(2), 379–387.

Melloni, L., Schwiedrzik, C. M., Rodriguez, E., & Singer, W. (2009). (Micro)Saccades, corollary activity and cortical oscillations. *Trends in Cognitive Sciences*, *13*(6), 239–245.

Mitzdorf, U. (1985). Current source-density method and application in cat cerebral cortex: investigation of evoked potentials and EEG phenomena. *Physiological Reviews*, *65*(1), 37.

Mitzdorf, U., & Singer, W. (1979). Excitatory synaptic ensemble properties in the visual cortex of the macaque monkey: a current source density analysis of electrically evoked potentials. *Journal of Comparative Neurology*, *187*(1), 71–83.

Moore, T., & Fallah, M. (2001). Control of eye movements and spatial attention. *Proceedings of the National Academy of Sciences*, *98*(3), 1273–1276.

Morey, R. D. (2008). Confidence intervals from normalized data: A correction to cousineau (2005). *Tutorials in Quantitative Methods for Psychology*, *4*, 61–64.

Müller, N., & Weisz, N. (2012). Lateralized auditory cortical alpha band activity and interregional connectivity pattern reflect anticipation of target sounds. *Cerebral Cortex*, *22*(7), 1604–1613.

Nakayama, K., & Martini, P. (2011). Situating visual search. *Vision research*, *51*(13), 1526–1537.

Noda, H., & Fujikado, T. (1987). Topography of the oculomotor area of the cerebellar vermis in macaques as determined by microstimulation. *Journal of Neurophysiology*, *58*(2), 359–378.

Noda, H., Murakami, S., Yamada, J., Tamada, J., Tamaki, Y., & Aso, T. (1988). Saccadic eye movements evoked by microstimulation of the fastigial nucleus of macaque monkeys. *Journal of Neurophysiology*, *60*(3), 1036–1052.

Nolte, G. (2003). The magnetic lead field theorem in the quasi-static approximation and its use for magnetoencephalography forward calculation in realistic volume conductors. *Physics in Medicine and Biology*, *48*(22), 3637–3652.

O'Keefe, J., & Burgess, N. (2005). Dual phase and rate coding in hippocampal place cells: theoretical significance and relationship to entorhinal grid cells. *Hippocampus*, *15*(7), 853–866.

O'Keefe, J., & Dostrovsky, J. (1971). The hippocampus as a spatial map. preliminary evidence from unit activity in the freely-moving rat. *Brain Research*, *34*(1), 171–175.

O'Keefe, J., & Recce, M. L. (1993). Phase relationship between hippocampal place units and the EEG theta rhythm. *Hippocampus*, *3*(3), 317–330.

Oostenveld, R., Fries, P., Maris, E., & Schoffelen, J.-M. (2011). FieldTrip: open source software for advanced analysis of MEG, EEG, and invasive electrophysiological data. *Computational Intelligence and Neuroscience*, *2011*, 1–9.

O'Reilly, R. C., & Norman, K. A. (2002). Hippocampal and neocortical contributions to memory: Advances in the complementary learning systems framework. *Trends in Cognitive Sciences*, *6*(12), 505–510.

Osipova, D., Hermes, D., & Jensen, O. (2008). Gamma power is phase-locked to posterior alpha activity. *PLoS ONE*, *3*(12), e3990.

Pettersen, K. H., Lindén, H., Dale, A. M., & Einevoll, G. T. (2012). Extracellular spikes and current-source density. In *Handbook of neural activity measurement.* Cambridge University Press.

Pfurtscheller, G., & Lopes da Silva, F. H. (1999). Event-related EEG/MEG synchronization and desynchronization: basic principles. *Clinical Neurophysiology*, *110*(11), 1842–1857.

Pierrot-Deseilligny, C., Milea, D., & Mri, R. M. (2004). Eye movement control by the cerebral cortex. *Current Opinion in Neurology*, *17*(1), 17–25.

Posner, M. I. (1980). Orienting of attention. *Quarterly Journal of Experimental Psychology*, *32*(1), 3–25.

Rajkai, C., Lakatos, P., Chen, C.-M., Pincze, Z., Karmos, G., & Schroeder, C. E. (2008). Transient cortical excitation at the onset of visual fixation. *Cerebral Cortex*, *18*(1), 200–209.

Rihs, T. A., Michel, C. M., & Thut, G. (2007). Mechanisms of selective inhibition in visual spatial attention are indexed by alpha-band EEG synchronization. *European Journal of Neuroscience*, *25*(2), 603–610.

Rizzolatti, G., Riggio, L., Dascola, I., & Umilt, C. (1987). Reorienting attention across the horizontal and vertical meridians: Evidence in favor of a premotor theory of attention. *Neuropsychologia*, *25*(1, Part 1), 31–40.

Robinson, F. R., & Fuchs, A. F. (2001). The role of the cerebellum in voluntary eye movements. *Annual Review of Neuroscience*, *24*(1), 981–1004.

Rohenkohl, G., Cravo, A. M., Wyart, V., & Nobre, A. C. (2012). Temporal expectation improves the quality of sensory information. *Journal of Neuroscience*, *32*(24), 8424–8428.

Rohenkohl, G., & Nobre, A. C. (2011). Alpha oscillations related to anticipatory attention follow temporal expectations. *Journal of Neuroscience*, *31*(40), 14076–14084.

Romei, V., Gross, J., & Thut, G. (2010). On the role of prestimulus alpha rhythms over occipito-parietal areas in visual input regulation: correlation or causation? *Journal of Neuroscience*, *30*(25), 8692–8697.

Rosene, D. L., & Van Hoesen, G. W. (1977). Hippocampal efferents reach widespread areas of cerebral cortex and amygdala in the rhesus monkey. *Science*, *198*(4314), 315–317.

Ross, J., Morrone, M. C., Goldberg, M. E., & Burr, D. C. (2001). Changes in visual perception at the time of saccades. *Trends in Neurosciences*, *24*(2), 113–121.

Saalmann, Y., & Kastner, S. (2011). Cognitive and perceptual functions of the visual thalamus. *Neuron*, *71*(2), 209–223.

Salinas, E., & Sejnowski, T. J. (2001). Correlated neuronal activity and the flow of neural information. *Nature Reviews Neuroscience*, *2*(8), 539–550.

Sauseng, P., Klimesch, W., Heise, K. F., Gruber, W. R., Holz, E., Karim, A. A., … Hummel, F. C. (2009). Brain oscillatory substrates of visual short-term memory capacity. *Current Biology*, *19*(21), 1846–1852.

Scheeringa, R., Mazaheri, A., Bojak, I., Norris, D. G., & Kleinschmidt, A. (2011). Modulation of visually evoked cortical fMRI responses by phase of ongoing occipital alpha oscillations. *Journal of Neuroscience*, *31*(10), 3813–3820.

Schroeder, C. E., & Lakatos, P. (2009). Low-frequency neuronal oscillations as instruments of sensory selection. *Trends in Neurosciences*, *32*(1), 9–18.

Schroeder, C. E., Tenke, C. E., Givre, S. J., Arezzo, J. C., & Vaughan, H. G., Jr. (1991).

Striate cortical contribution to the surface-recorded pattern-reversal VEP in the alert monkey. *Vision Research*, *31*(7-8), 1143–1157.

Schroeder, C. E., Wilson, D. A., Radman, T., Scharfman, H., & Lakatos, P. (2010). Dynamics of active sensing and perceptual selection. *Current Opinion in Neurobiology*, *20*(2), 172–176.

Scoville, W. B., & Milner, B. (1957). Loss of recent memory after bilateral hippocampal lesions. *Journal of Neurology, Neurosurgery, and Psychiatry*, *20*(1), 11–21.

Siapas, A. G., Lubenov, E. V., & Wilson, M. A. (2005). Prefrontal phase locking to hippocampal theta oscillations. *Neuron*, *46*(1), 141–151.

Silberberg, G., & Markram, H. (2007). Disynaptic inhibition between neocortical pyramidal cells mediated by martinotti cells. *Neuron*, *53*(5), 735–746.

Sirota, A., Csicsvari, J., Buhl, D., & Buzsáki, G. (2003). Communication between neocortex and hippocampus during sleep in rodents. *Proceedings of the National Academy of Sciences*, *100*(4), 2065–2069.

Sirota, A., Montgomery, S., Fujisawa, S., Isomura, Y., Zugaro, M., & Buzsáki, G. (2008). Entrainment of neocortical neurons and gamma oscillations by the hippocampal theta rhythm. *Neuron*, *60*(4), 683–697.

Sohal, V. S., & Huguenard, J. R. (2005). Inhibitory coupling specifically generates emergent gamma oscillations in diverse cell types. *Proceedings of the National Academy of Sciences*, *102*(51), 18638–18643.

Spaak, E., Bonnefond, M., Maier, A., Leopold, D. A., & Jensen, O. (2012). Layer-specific entrainment of gamma-band neural activity by the alpha rhythm in monkey visual cortex. *Current Biology*, *22*(24), 2313–2318.

Squire, L. R. (1992). Memory and the hippocampus: A synthesis from findings with rats, monkeys, and humans. *Psychological Review*, *99*(2), 195–231.

Stokes, M. G., Atherton, K., Patai, E. Z., & Nobre, A. C. (2012). Long-term memory prepares neural activity for perception. *Proceedings of the National Academy of Sciences*, *109*(6), E360–367.

Tallon-Baudry, C., & Bertrand, O. (1999). Oscillatory gamma activity in humans and its role in object representation. *Trends in Cognitive Sciences*, *3*(4), 151–162.

Tamás, G., Buhl, E. H., Lörincz, A., & Somogyi, P. (2000). Proximally targeted GABAergic synapses and gap junctions synchronize cortical interneurons. *Nature Neuroscience*, *3*(4), 366–371.

ter Huurne, N., Onnink, M., Kan, C., Franke, B., Buitelaar, J., & Jensen, O. (2013). Behavioral consequences of aberrant alpha lateralization in attention-deficit/hyperactivity disorder. *Biological Psychiatry*, *74*(3), 227–233.

Tesche, C. D., & Karhu, J. (2000b). Theta oscillations index human hippocampal activation during a working memory task. *Proceedings of the National Academy of Sciences*, *97*(2), 919–924.

Tesche, C. D., & Karhu, J. J. (2000a). Anticipatory cerebellar responses during somatosensory omission in man. *Human Brain Mapping*, *9*(3), 119–142.

Thomson, A. M., & Bannister, A. P. (2003). Interlaminar connections in the neocortex. *Cerebral Cortex*, *13*(1), 5–14.

Thut, G., & Miniussi, C. (2009). New insights into rhythmic brain activity from TMS-EEG studies. *Trends in Cognitive Sciences*, *13*(4), 182–189.

Thut, G., Miniussi, C., & Gross, J. (2012). The functional importance of rhythmic activity in the brain. *Current Biology*, *22*(16), R658–R663.

Thut, G., Nietzel, A., Brandt, S. A., & Pascual-Leone, A. (2006). Alpha-band electroencephalographic activity over occipital cortex indexes visuospatial attention bias and predicts visual target detection. *Journal of Neuroscience*, *26*(37), 9494–9502.

Thut, G., Veniero, D., Romei, V., Miniussi, C., Schyns, P., & Gross, J. (2011). Rhythmic TMS causes local entrainment of natural oscillatory signatures. *Current Biology*, *21*(14), 1176–1185.

Tierney, P. L., Degenetais, E., Thierry, A. M., Glowinski, J., & Gioanni, Y. (2004). Influence of the hippocampus on interneurons of the rat prefrontal cortex. *European Journal of Neuroscience*, *20*(2), 514.

Tort, A. B. L., Komorowski, R., Eichenbaum, H., & Kopell, N. (2010). Measuring phase-amplitude coupling between neuronal oscillations of different frequencies. *Journal of Neurophysiology*, *104*(2), 1195 –1210.

TRAUB, R. D., KOPELL, N., BIBBIG, A., BUHL, E. H., LEBEAU, F. E. N., & WHITTINGTON, M. A. (2001). Gap junctions between interneuron dendrites can enhance synchrony of gamma oscillations in distributed networks. *Journal of Neuroscience*, *21*(23), 9478.

TREISMAN, A. M., & GELADE, G. (1980). A feature-integration theory of attention. *Cognitive psychology*, *12*(1), 97–136.

VAN DER WERF, J., BUCHHOLZ, V. N., JENSEN, O., & MEDENDORP, W. P. (2009). Neuronal synchronization in human parietal cortex during saccade planning. *Behavioural Brain Research*, *205*(2), 329–335.

VAN DER WERF, J., JENSEN, O., FRIES, P., & MEDENDORP, W. P. (2008). Gamma-band activity in human posterior parietal cortex encodes the motor goal during delayed prosaccades and antisaccades. *Journal of Neuroscience*, *28*(34), 8397–8405.

VAN DIJK, H., SCHOFFELEN, J.-M., OOSTENVELD, R., & JENSEN, O. (2008). Prestimulus oscillatory activity in the alpha band predicts visual discrimination ability. *Journal of Neuroscience*, *28*(8), 1816 –1823.

VAN EDE, F., DE LANGE, F., JENSEN, O., & MARIS, E. (2011). Orienting attention to an upcoming tactile event involves a spatially and temporally specific modulation of sensorimotor alpha- and beta-band oscillations. *Journal of Neuroscience*, *31*(6), 2016 –2024.

VAN KERKOERLE, T., SELF, M., POORT, J., DER TOGT, V., & ROELFSEMA, P. (2011). High frequencies flow in the feed-forward direction through the different layers of monkey primary visual cortex while low frequencies flow in the recurrent direction. In *Society for neuroscience program no. 270.08.*

VANRULLEN, R., & KOCH, C. (2003). Is perception discrete or continuous? *Trends in Cognitive Sciences*, *7*(5), 207–213.

VANRULLEN, R., & MACDONALD, J. S. P. (2012). Perceptual echoes at 10 hz in the human brain. *Current Biology*, *22*(11), 995–999.

VAN VEEN, B. D., VAN DRONGELEN, W., YUCHTMAN, M., & SUZUKI, A. (1997). Localization of brain electrical activity via linearly constrained minimum variance spatial filtering. *IEEE Transactions on Bio-Medical Engineering*, *44*(9), 867–880.

VENANCE, L., ROZOV, A., BLATOW, M., BURNASHEV, N., FELDMEYER, D., & MONYER, H. (2000). Connexin expression in electrically coupled postnatal rat brain neurons. *Proceedings of the National Academy of Sciences*, *97*(18), 10260–10265.

VIDA, I., BARTOS, M., & JONAS, P. (2006). Shunting inhibition improves robustness of gamma oscillations in hippocampal interneuron networks by homogenizing firing rates. *Neuron*, *49*(1), 107–117.

VOYTEK, B., CANOLTY, R. T., SHESTYUK, A., CRONE, N. E., PARVIZI, J., & KNIGHT, R. T. (2010a). Shifts in gamma phase-amplitude coupling frequency from theta to alpha over posterior cortex during visual tasks. *Frontiers in Human Neuroscience*, *4*(191), 1–9.

VOYTEK, B., CANOLTY, R. T., SHESTYUK, A., CRONE, N. E., PARVIZI, J., & KNIGHT, R. T. (2010b). Shifts in gamma phase–amplitude coupling frequency from theta to alpha over posterior cortex during visual tasks. *Frontiers in Human Neuroscience*, *4*.

WANG, X. J., & BUZSÁKI, G. (1996). Gamma oscillation by synaptic inhibition in a hippocampal interneuronal network model. *Journal of Neuroscience*, *16*(20), 6402–6413.

WATSON, A. B., & PELLI, D. G. (1983). QUEST: a bayesian adaptive psychometric method. *Perception & Psychophysics*, *33*(2), 113–120.

WIDMANN, A., SCHRGER, E., & MAESS, B. (in press). Digital filter design for electrophysiological data a practical approach. *Journal of Neuroscience Methods*.

WOLFE, J. M. (1998). Visual search. In H. Pashler (Ed.), *Attention.* London, UK: University College London Press.

WORDEN, M. S., FOXE, J. J., WANG, N., & SIMPSON, G. V. (2000). Anticipatory biasing of visuospatial attention indexed by retinotopically specific alpha-band electroencephalography increases over occipital cortex. *Journal of Neuroscience*, *20*(6), RC63.

WU, J., & OKADA, Y. C. (1999). Roles of a potassium afterhyperpolarization current in generating neuromagnetic fields and field potentials in longitudinal CA3 slices of the guinea-pig. *Clinical Neurophysiology*, *110*(11), 1858–1867.

XIANG, Z., HUGUENARD, J. R., & PRINCE, D. A. (1998). Cholinergic switching within neocortical inhibitory networks. *Science*, *281*(5379), 985–988.

Xu, X., & Callaway, E. M. (2009). Laminar specificity of functional input to distinct types of inhibitory cortical neurons. *Journal of Neuroscience*, *29*(1), 70–85.

Yamagishi, N., Callan, D. E., Goda, N., Anderson, S. J., Yoshida, Y., & Kawato, M. (2003). Attentional modulation of oscillatory activity in human visual cortex. *Neuroimage*, *20*(1), 98–113.

Zauner, A., Fellinger, R., Gross, J., Hanslmayr, S., Shapiro, K., Gruber, W., … Klimesch, W. (2012). Alpha entrainment is responsible for the attentional blink phenomenon. *Neuroimage*, *63*(2), 674–686.

Nederlandse samenvatting

Dit proefschrift gaat over zogeheten *neurale oscillaties*. Een oscillatie is simpelweg een trilling; denk bijvoorbeeld aan een snaar die trilt. Een *neurale* oscillatie is dus een 'trilling' in neuronen, de cellen waaruit ons brein is opgebouwd. Maar wat trilt er dan? Het gaat hier natuurlijk niet om een fysieke trilling van het brein zelf, dat zou hoofdpijn opleveren. Neuronen communiceren door middel van minuscule stroompjes die variëren van moment tot moment. Nu blijkt dat de variatie van deze stroom over tijd in veel gevallen sterk ritmisch is; deze ritmische patronen noemen we neurale oscillaties.

Deze neurale oscillaties kunnen op verschillende manieren gemeten worden. Het is mogelijk om op heel kleine schaal, die van een enkele cel of zelfs delen daarvan, te kijken hoe neurale oscillaties zich gedragen. Hiermee kan men veel te weten komen over de neurobiofysische principes die ervoor zorgen dat neuronen ritmische activiteit vertonen. Een stapje 'uitgezoomd' kan men met micro-elektrodes een populatie cellen, *in vitro*[1] of in levende dieren, meten, en zo zien hoe de activiteit van een kleine groep cellen (enkele tientallen tot duizenden) vormgegeven wordt doordat de individuele cellen graag ritmische stroompjes uitzenden. We kunnen ook nog verder uitzoomen, om ook grotere netwerken (van miljoenen tot tientallen miljarden neuronen) te begrijpen aan de hand van de neurale oscillaties die erin voorkomen.

Op de grootste schaal kunnen neurale oscillaties (wanneer genoeg neuronen tegelijkertijd hetzelfde doen) gemeten worden buiten het hoofd, met elektro- of magneto-encefalografie (EEG of MEG). Met zulke non-invasieve technieken kunnen dus experimenten worden gedaan met gezonde, menselijke proefpersonen. Daarmee is het mogelijk de neurale oscillaties te koppelen aan intelligent gedrag, emotie, en cognitie. Omdat neurale oscillaties op al deze verschillende

---

[1] Een klompje cellen in een (glazen) petrischaaltje.

niveaus onderzocht kunnen worden, bieden ze in mijn ogen een ideale mogelijkheid voor de cognitieve neurowetenschapper. We kunnen nu namelijk hetzelfde neurale fenomeen begrijpen in termen van welke cognitieve processen ermee samenhangen, welke hersenstructuren en -netwerken er cruciaal voor zijn, en hoe het fenomeen op cellulair of zelfs moleculair niveau in elkaar steekt. Zo wordt het mogelijk intelligentie en gewaarwording écht te begrijpen.

Neurale oscillaties komen voor in verschillende frequentiebanden die elk met een Griekse letter aangeduid worden. In dit proefschrift staan *alpha-* en, in mindere mate, *gamma*-oscillaties centraal. Alpha-oscillaties hebben een frequentie van rond de tien Hertz (trillingen per seconde), en er is veel bewijs uit EEG en MEG studies dat deze frequentieband samenhangt met selectieve aandacht. Zo blijkt de amplitude van alpha-activiteit omlaag te gaan in hersengebieden die je nodig hebt voor de taak waar je mee bezig bent (en waar je dus je aandacht op richt). Omgekeerd wordt alpha-activiteit juist sterker in hersengebieden die je niet gebruikt (zodat je aandacht niet afgeleid wordt). Op basis van deze bevindingen hebben meerdere onderzoekers de hypothese geformuleerd dat alpha een 'functionele ritmische remming' van hersengebieden weerspiegelt. Het bestaan van deze functionele remming is door verschillende onderzoeken aannemelijk gemaakt in hersengebieden zoals de motorische en auditieve schors, maar het sterkst komt deze naar voren in het visuele systeem.

Gamma-oscillaties (met een frequentie > 30 Hz) zijn ook sterk vertegenwoordigd in het visuele systeem. Gamma-activiteit is prominent waar te nemen als er nieuwe visuele informatie het brein binnenkomt. Vermoedelijk duidt het optreden van gamma-activiteit erop dat een middelgroot lokaal netwerk van neuronen tegelijkertijd actief wordt om deze nieuwe informatie te verwerken.

Mijn proefschrift behandelt drie vragen omtrent alpha-oscillaties. Ten eerste, hoewel er genoeg bewijs is dat alpha-activiteit *samenhangt* met visuele aandacht, kunnen we stellen dat deze samenhang *causaal* is? Dat wil zeggen, zijn modulaties van alpha-activiteit een *essentieel* onderdeel van selectieve aandacht? Ten tweede, welk neuronaal-netwerkmechanisme zorgt ervoor dat alpha-oscillaties het verwerken van visuele informatie kunnen beïnvloeden? Als alpha aandacht weerspiegelt, moet er zo'n mechanisme zijn, want we weten dat zaken waar we onze aandacht op richten veel efficiënter worden afgehandeld dan zaken waar we niet op letten. Ten derde, kunnen we het moduleren van alpha-oscillaties zien als een algemeen cognitief mechanisme, of is het een fenomeen dat zich alleen voordoet in kunstmatige experimentele omstandigheden?

In hoofdstuk 2 beschrijf ik de resultaten van een MEG-experiment dat ik met menselijke proefpersonen heb uitgevoerd. Ik laat erin zien dat visuele alpha-activiteit direct kan worden beïnvloed door externe ritmische stimuli (lichtflitsen) met een frequentie die lijkt op alpha. De 'alpha'-activiteit die door deze stimuli wordt veroorzaakt heeft gevolgen voor de visuele waarneming, en deze gevolgen lijken op de gevolgen die normale, spontaan gegenereerde, alpha-activiteit heeft. Daarom kunnen we concluderen dat alpha-activiteit causaal betrokken is bij het verwerken van visuele informatie. Als alpha-activiteit namelijk slechts een onbelangrijk extra gevolg zou zijn van het richten van aandacht, dan zou dat betekenen dat deze kunstmatige alpha-activiteit (die per definitie niet het gevolg was van het richten van aandacht) geen (of een ander) effect op visuele waarneming zou moeten hebben.

In hoofdstuk 3 verschuift mijn blik naar een veel kleinere schaal. Met een zogeheten 'laminaire' elektrode hebben mijn collega's de activiteit van alle lagen van één neuronaal subnetwerkje gelijktijdig kunnen meten. Met geavanceerde analyses van de resultaten van deze meting laat ik zien dat alpha en gamma op zo'n kleine schaal sterk samenhangen: de *fase* van alpha moduleert gamma-activiteit (een samenhang op een hele snelle tijdsschaal), en gamma wordt ook beïnvloed door de *amplitude* van alpha (een samenhang op een tijdsschaal van enkele seconden). Deze samenhang kan een mechanisme vormen waarmee alpha het verwerken van visuele informatie beïnvloedt.

Hoofdstuk 4 neemt enige afstand van alpha-activiteit in het visuele systeem. In hoofdstuk 3 liet ik zien dat er een koppeling bestaat tussen de fase van alpha en de amplitude van gamma. In hoofdstuk 4 onderzoek ik welke netwerkmechanismen verantwoordelijk zouden kunnen zijn voor een dergelijke koppeling. Hiervoor heb ik een model gebouwd van fase-amplitudekoppeling, en in hoofdstuk 4 laat ik zien dat een speciaal type neuronen, de zogenoemde 'snel-vurende interneuronen' waarschijnlijk cruciaal zijn voor dit type koppeling tussen verschillende neurale oscillaties.

In de laatste twee empirische hoofdstukken keer ik weer terug naar MEG met menselijke proefpersonen. In hoofdstuk 5 beschrijf ik de resultaten van een experiment waarin proefpersonen gevraagd werd bepaalde visuele stimuli zo snel mogelijk te identificeren te midden van andere, afleidende, stimuli. Het was al bekend dat mensen zich goed kunnen voorbereiden op zulke sets van stimuli, als ze weten wat ze kunnen verwachten. Ik laat nu zien dat het moduleren van alpha-activiteit één van de manieren is waarop deze voorbereiding is geïmplementeerd in het brein.

Wanneer mensen dingen bekijken, maken ze ongeveer drie keer per seconde zeer snelle oogbewegingen die *saccades* worden genoemd. Tot besluit van het empirische deel van mijn proefschrift laat ik in hoofdstuk 6 zien dat alpha-activiteit ook gemoduleerd wordt ter voorbereiding op het uitvoeren van zulke saccades. De resultaten van hoofdstuk 5 en hoofdstuk 6 tonen dus aan dat de modulatie van alpha-oscillaties een algemeen mechanisme is, dat zich niet beperkt tot kunstmatige experimentele instructies, maar zich ook voordoet bij alledaagse cognitieve taken (het bewust zoeken naar visuele informatie te midden van rommel, en simpelweg rondkijken).

Curriculum Vitae

Eelke Spaak was born on 2nd December 1985, in Nijmegen. After graduating from the Stedelijk Gymnasium Nijmegen, he went on to pursue a Bachelor's degree in Artificial Intelligence (AI) at the Radboud University. Eelke's bachelor's thesis was completed under the supervision of dr. Pim Haselager, and focused on evolutionary robotics and the development of mirror neurons. Over the course of his AI studies, Eelke started to study for a Bachelor's degree in Philosophy as well. His Philosophy bachelor's thesis was completed under the supervision of prof. dr. Marc Slors, and pertained to the metaphysical nature of causality, as applied to both physical processes and human volition. After these bachelor's degrees, Eelke attended and completed the Masters program in Cognitive Neuroscience (CNS) at the Donders Institute, doing work which prepared him for the PhD program described in this thesis. But before starting his PhD program, Eelke obtained a Huygens Talent award which enabled him to move to Edinburgh in pursuit of a Master's degree in Philosophy. After completion of this degree, Eelke joined prof. dr. Ole Jensen's group at the Donders Centre for Cognitive Neuroimaging, where he did the work leading to the present thesis. Apart from basic research, Eelke was involved in teaching several classes and the supervision of Master's students, and took part in the core development team for FieldTrip, an internationally widely used software package for the analysis of electrophysiological data. He will move to the University of Oxford in May 2015 to investigate the cortical connectivity patterns underpinning working memory, working with dr. Mark Stokes.

Author publications

Jensen, O., **Spaak, E.**, & Zumer, J.M. (2014) Human brain oscillations: From physiological mechanisms to analysis and cognition. In Supek, S., & Aine, C.J. (Eds.), Magnetoencephalography: From signals to dynamic cortical networks. Berlin: Springer.

Spaak., E., De Lange, F.P., & Jensen, O. (2014). Local entrainment of alpha oscillations by visual stimuli causes cyclic modulation of perception. *The Journal of Neuroscience*. 34(10), 3536-3544, doi:10.1523/jneurosci.4385-13.2014

Spaak, E., Bonnefond, M., Maier, A., Leopold, D.A., & Jensen, O. (2012). Layer-specific entrainment of gamma-band neural activity by the alpha rhythm in monkey visual cortex. *Current Biology*, 22(24), 23132318. doi: 10.1016/j.cub.2012.10.020

Spaak, E., Zeitler, M., & Gielen, C.C.A.M. (2012). Hippocampal theta modulation of neocortical spike times and gamma rhythm: A biophysical model study. *PLoS ONE*, 7(10): e45688. doi:10.1371/journal.pone.0045688

Spaak, E. (2009). No one is tricking anyone: A critique of Wegners theory of conscious will. *Splijtstof*, 37(3), 1526.

Spaak, E. & Haselager, P.F.G. (2008). Imitation and mirror neurons: An evolutionary robotics model. In A. Nijholt, M. Pantic, M. Poel, & H. Hondorp (Eds.) *Proceedings of BNAIC 2008, the Twentieth Belgian-Dutch Artificial Intelligence Conference*. (pp. 249256). Enschede: University of Twente.

Acknowledgements

As one might imagine, a doctoral thesis does not produce itself. And although only my name decorates this particular thesis' cover, the work described in it could not have been completed if it were not for the varied contributions of many different individuals.

First, I would like to thank my supervisor and promotor Ole Jensen. Throughout my PhD, I have benefitted a lot from your insight into the scientific literature and your know-how on how to identify and tackle the most relevant question at any particular time in the life of a research project. Your support was always there when I needed it, which was often at short notice. You supported me not only through practical and theoretical scientific advice, but also offered great guidance in navigating the international academic world (including personal introductions to many scientific 'big shots'), for which I am very grateful. Finally, your attitude to science and life in general has set a good example of how not to let stuff weigh you down; it's hard to stay stressed in the face of remarks like "Let's say you were to get a brain tumour in a month, you would still get a PhD, right?"

I would like to thank my co-promotor Floris de Lange, from whom I also learned a great deal. Thank you for the excellent scientific advice and support, and for inviting me into your research group as a full member, including to social events and your group retreat.

Thanks also go to Robert Oostenveld and Jan-Mathijs Schoffelen, the general and captain, respectively, of FieldTrip. During as well as outside the FieldTrip meetings, you taught me both the general ideas and the nitty-gritty details of how to do proper MEG data analysis. The fact that I was allowed to hack away at FieldTrip myself was the icing on the cake.

I feel privileged to have been a part of the Donders, where the stimulating intellectual atmosphere is matched by the pleasantness of the colleagues. In *no* *particular order* and with possible (intended) duplicates, I thank the past and present members of the Neuronal Oscillations group: Mathilde Bonnefond, Til Ole Bergmann (the two of you and Guillaume Sescousse thanks for the great wine nights!), Ali Bahramisharif, René Scheeringa, Jan van der Eerden, Tzvetan Popov, Niels ter Huurne, Freek van Ede, Jörn Horschig, Diego Lozano Soldevilla, Tom Marshall, Haiteng Jiang, Marieke van de Nieuwenhuijzen, Madelon Vollebregt, Bart Gips, Jim Herring, Maarten Leenders, Sophie Esterer, René Terporten, Rocio Silva Zunino, Esther Meeuwissen, Saskia Haegens, Stephen Whitmarsh, Johanna Zumer, Lisa Luther, Rodolfo Solis-Vivanco, Anne Kösem. The FieldTrip core team: Robert Oostenveld, Jan-Mathijs Schoffelen, Saskia Haegens, Stephen Whitmarsh, Roemer van der Meij, Jörn Horschig, Johanna Zumer, Lilla Magyari, Arjen Stolk, Jim Herring, Nietzsche Lam, Luca Ambrogioni, Remco Bastiaannet. My office mates: Frauke van der Ven, Susanne Vogel, Daan van Rooij, Richard Kunert, Xu Gong, Ili Ma, Monique Timmer, Liesbeth Hoekstra. All the other Donderians who have been part of my life these past years and do not fit any of the labels above: Jolien Francken (a very special mention of course; my time at the Donders would not have been complete without 'our' Foundations meetings!), Alex Backus, Anke Marit Albers, Flora Vanlangendonck, Ruben van Bergen, Ian Cameron, Jeanette Mostert, Jeroen van Baar, Kim Fairley, Lieneke Janssen, Loek Brinkman, Matthias Ekman, Miriam de Boer, Mirjam Bloemendaal, Monja Froböse, Peter Hagoort, Peter Kok, Elexa St. John-Saaltink, Pim Haselager, Iris van Rooij, Ruud Berkers, Sander Bosch, Tim van Mourik, Vincent Schoots, Winke Francx, Marieke van der Schaaf, Eric Maris, Marlieke van Kesteren. All Donderian colleagues above, and anyone I may have inadvertently forgotten, thank you for the great discussions and for all the fun we had at our various meetings, at the lunch table, or in the pub.

A word of thanks also goes out to the administration at the Donders: Sandra Heemskerk, Nicole Stekkinger, Ayse Özkan, and of course Arthur Willemsen and above all Tildie Stijns, without whom the institute would collapse. The same goes for the outstanding technical support group: Marek Tyc, Edward Gerrits, Sander Berends, Jessica Askamp, Hong Lee, and Erik van den Boogert.

I am fortunate to be surrounded by great friends and family outside the Donders as well. My dear friends Frank van Caspel, Rik van Kessel, Geert Bulte, Erik Hermans; thank you for the innumerable great times we've been having ever since school, including of course during my work on this thesis (I hope it lives up to its predecessor *Particles*, Rik). I look forward to many more years of the same. I also thank all my friends at Antworks, my *amices* at De Gong, and

others for enabling me to periodically recharge during the writing of this thesis.

My parents, Ronald and Margit Spaak, thank you for all the love and support during my entire academic career (which I take here to include everything from nursery school onwards); thank you for making all this possible.

Also the rest of my (small) family, my brother Wouter Spaak, my late grandmother Joop van Bruggen, and my uncle Rob van Bruggen, thank you for everything. The same goes for the Boefjes: thanks Nico, Simone, Maarten, Eefje, and Jeske Boef.

Both of them have already been mentioned, but I would like to thank again Wouter Spaak and Tom Marshall for doing me the honour of being my paranymphs. While writing these acknowledgements the day has not yet come, but I imagine the support you have agreed to offer during my defense will be highly welcomed. Additional thanks to Wouter for designing the cover for this book.

Finally I would like to thank Nynke Boef, for being my kindest supporter and toughest critic. When you are around, all the good things in life are that much better.

Donders Series publications

1. Van Aalderen-Smeets, S.I. (2007). *Neural dynamics of visual selection.* Maastricht University, Maastricht, the Netherlands.
2. Schoffelen, J.M. (2007). *Neuronal communication through coherence in the human motor system.* Radboud University, Nijmegen, the Netherlands.
3. De Lange, F.P. (2008). *Neural mechanisms of motor imagery.* Radboud University, Nijmegen, the Netherlands.
4. Grol, M.J. (2008). *Parieto-frontal circuitry in visuomotor control.* Utrecht University, Utrecht, the Netherlands.
5. Bauer, M. (2008). *Functional roles of rhythmic neuronal activity in the human visual and somatosensory system.* Radboud University, Nijmegen, the Netherlands.
6. Mazaheri, A. (2008). *The influence of ongoing oscillatory brain activity on evoked responses and behaviour.* Radboud University, Nijmegen, the Netherlands.
7. Hooijmans, C.R. (2008). *Impact of nutritional lipids and vascular factors in Alzheimer's disease.* Radboud University, Nijmegen, the Netherlands.
8. Gaszner, B. (2008). *Plastic responses to stress by the rodent urocortinergic Edinger-Westphal nucleus.* Radboud University, Nijmegen, the Netherlands.
9. Willems, R.M. (2009). *Neural reflections of meaning in gesture, language and action.* Radboud University, Nijmegen, the Netherlands.
10. Van Pelt, S. (2009). *Dynamic neural representations of human visuomotor space.* Radboud University, Nijmegen, the Netherlands.
11. Lommertzen, J. (2009). *Visuomotor coupling at different levels of complexity.* Radboud University, Nijmegen, the Netherlands.
12. Poljac, E. (2009). *Dynamics of cognitive control in task switching: Looking beyond the switch cost.* Radboud University, Nijmegen, the Netherlands.
13. Poser, B.A. (2009). *Techniques for BOLD and blood volume weighted fMRI.* Radboud University, Nijmegen, the Netherlands.
14. Baggio, G. (2009). *Semantics and the electrophysiology of meaning. Tense, aspect, event structure.* Radboud University, Nijmegen, the Netherlands.
15. Van Wingen, G.A. (2009). *Biological determinants of amygdala functioning.* Radboud University Medical Centre, Nijmegen, the Netherlands.
16. Bakker, M. (2009). *Supraspinal control of walking: Lessons from motor imagery.* Radboud University Medical Centre, Nijmegen, the Netherlands.
17. Aarts, E. (2009). *Resisting temptation: The role of the anterior cingulate cortex in adjusting cognitive control.* Radboud University, Nijmegen, the Netherlands.
18. Prinz, S. (2009). *Waterbath stunning of chickens - Effects of electrical parameters on the electroencephalogram and physical reflexes of broilers.* Radboud University, Nijmegen, the Netherlands.

19. Knippenberg, J.M.J. (2009). *The N150 of the Auditory Evoked Potential from the rat amygdala: In search for its functional significance.* Radboud University, Nijmegen, the Netherlands.
20. Dumont, G.J.H. (2009). *Cognitive and physiological effects of 3,4-methylenedioxymethamphetamine (MDMA or 'ecstasy') in combination with alcohol or cannabis in humans.* Radboud University, Nijmegen, the Netherlands.
21. Pijnacker, J. (2010). *Defeasible inference in autism: A behavioral and electrophysiogical approach.* Radboud University, Nijmegen, the Netherlands.
22. De Vrijer, M. (2010). *Multisensory integration in spatial orientation.* Radboud University, Nijmegen, the Netherlands.
23. Vergeer, M. (2010). *Perceptual visibility and appearance: Effects of color and form.* Radboud University, Nijmegen, the Netherlands.
24. Levy, J. (2010). *In cerebro unveiling unconscious mechanisms during reading.* Radboud University, Nijmegen, the Netherlands.
25. Treder, M. S. (2010). *Symmetry in (inter)action.* Radboud University, Nijmegen, the Netherlands.
26. Horlings C.G.C. (2010). *A weak balance: Balance and falls in patients with neuromuscular disorders.* Radboud University, Nijmegen, the Netherlands.
27. Snaphaan, L.J.A.E. (2010). *Epidemiology of post-stroke behavioural consequences.* Radboud University Medical Centre, Nijmegen, the Netherlands.
28. Dado - Van Beek, H.E.A. (2010). *The regulation of cerebral perfusion in patients with Alzheimer's disease.* Radboud University Medical Centre, Nijmegen, the Netherlands.
29. Derks, N.M. (2010). *The role of the non-preganglionic Edinger-Westphal nucleus in sex-dependent stress adaptation in rodents.* Radboud University, Nijmegen, the Netherlands.
30. Wyczesany, M. (2010). *Covariation of mood and brain activity. Integration of subjective self-report data with quantitative EEG measures.* Radboud University, Nijmegen, the Netherlands.
31. Beurze S.M. (2010). *Cortical mechanisms for reach planning.* Radboud University, Nijmegen, the Netherlands.
32. Van Dijk, J.P. (2010). *On the Number of Motor Units.* Radboud University, Nijmegen, the Netherlands.
33. Lapatki, B.G. (2010). *The Facial Musculature - Characterization at a Motor Unit Level.* Radboud University, Nijmegen, the Netherlands.
34. Kok, P. (2010). *Word order and verb inflection in agrammatic sentence production.* Radboud University, Nijmegen, the Netherlands.
35. van Elk, M. (2010). *Action semantics: Functional and neural dynamics.* Radboud University, Nijmegen, the Netherlands.
36. Majdandzic, J. (2010). *Cerebral mechanisms of processing action goals in self and others.* Radboud University, Nijmegen, the Netherlands.
37. Snijders, T.M. (2010). *More than words - Neural and genetic dynamics of syntactic unification.* Radboud University, Nijmegen, the Netherlands.
38. Grootens, K.P. (2010). *Cognitive dysfunction and effects of antipsychotics in schizophrenia and borderline personality disorder.* Radboud University Medical Centre, Nijmegen, the Netherlands.
39. Nieuwenhuis, I.L.C. (2010). *Memory consolidation: A process of integration - Converging evidence from MEG, fMRI and behavior.* Radboud University Medical Centre, Nijmegen, the Netherlands.
40. Menenti, L.M.E. (2010). *The right language: Differential hemispheric contributions to language production and comprehension in context.* Radboud University, Nijmegen, the Netherlands.
41. Van Dijk, H.P. (2010). *The state of the brain, how alpha oscillations shape behaviour and event related responses.* Radboud University, Nijmegen, the Netherlands.
42. Meulenbroek, O.V. (2010). *Neural correlates of episodic memory in healthy aging and*

Alzheimer's disease. Radboud University, Nijmegen, the Netherlands.

43. Oude Nijhuis, L.B. (2010). *Modulation of human balance reactions.* Radboud University, Nijmegen, the Netherlands.
44. Qin, S. (2010). *Adaptive memory: Imaging medial temporal and prefrontal memory systems.* Radboud University, Nijmegen, the Netherlands.
45. Timmer, N.M. (2011). *The interaction of heparan sulfate proteoglycans with the amyloid protein.* Radboud University, Nijmegen, the Netherlands.
46. Crajé, C. (2011). *(A)typical motor planning and motor imagery.* Radboud University, Nijmegen, the Netherlands.
47. Van Grootel, T.J. (2011). *On the role of eye and head position in spatial localisation behaviour.* Radboud University, Nijmegen, the Netherlands.
48. Lamers, M.J.M. (2011). *Levels of selective attention in action planning.* Radboud University, Nijmegen, the Netherlands.
49. Van der Werf, J. (2011). *Cortical oscillatory activity in human visuomotor integration.* Radboud University, Nijmegen, the Netherlands.
50. Scheeringa, R. (2011). *On the relation between oscillatory EEG activity and the BOLD signal.* Radboud University, Nijmegen, the Netherlands.
51. Bögels, S. (2011). *The role of prosody in language comprehension: When prosodic breaks and pitch accents come into play.* Radboud University, Nijmegen, the Netherlands.
52. Ossewaarde, L. (2011). *The mood cycle: Hormonal influences on the female brain.* Radboud University, Nijmegen, the Netherlands.
53. Kuribara, M. (2011). *Environment-induced activation and growth of pituitary melanotrope cells of Xenopus laevis.* Radboud University, Nijmegen, the Netherlands.
54. Helmich, R.C.G. (2011). *Cerebral reorganization in Parkinson's disease.* Radboud University, Nijmegen, the Netherlands.
55. Boelen, D. (2011). *Order out of chaos? Assessment and treatment of executive disorders in brain-injured patients.* Radboud University, Nijmegen, the Netherlands.
56. Koopmans, P.J. (2011). *fMRI of cortical layers.* Radboud University, Nijmegen, the Netherlands.
57. van der Linden, M.H. (2011). *Experience-based cortical plasticity in object category representation.* Radboud University, Nijmegen, the Netherlands.
58. Kleine, B.U. (2011). *Motor unit discharges - Physiological and diagnostic studies in ALS.* Radboud University Medical Centre, Nijmegen, the Netherlands.
59. Paulus, M. (2011). *Development of action perception: Neurocognitive mechanisms underlying children's processing of others' actions.* Radboud University, Nijmegen, the Netherlands.
60. Tieleman, A.A. (2011). *Myotonic dystrophy type 2. A newly diagnosed disease in the Netherlands.* Radboud University Medical Centre, Nijmegen, the Netherlands.
61. Van Leeuwen, T.M. (2011). *'How one can see what is not there': Neural mechanisms of grapheme-colour synaesthesia.* Radboud University, Nijmegen, the Netherlands.
62. Van Tilborg, I.A.D.A. (2011). *Procedural learning in cognitively impaired patients and its application in clinical practice.* Radboud University, Nijmegen, the Netherlands.
63. Bruinsma, I.B. (2011). *Amyloidogenic proteins in Alzheimer's disease and Parkinson's disease: Interaction with chaperones and inflammation.* Radboud University, Nijmegen, the Netherlands.
64. Voermans, N. (2011). *Neuromuscular features of Ehlers-Danlos syndrome and Marfan syndrome; expanding the phenotype of inherited connective tissue disorders and investigating the role of the extracellular matrix in muscle.* Radboud University Medical Centre, Nijmegen, the Netherlands.
65. Reelick, M. (2011). *One step at a time. Disentangling the complexity of preventing falls in frail older persons.* Radboud University Medical Centre, Nijmegen, the Netherlands.

66. Buur, P.F. (2011). *Imaging in motion. Applications of multi-echo fMRI.* Radboud University, Nijmegen, the Netherlands.
67. Schaefer, R.S. (2011). *Measuring the mind's ear: EEG of music imagery.* Radboud University, Nijmegen, the Netherlands.
68. Xu, L. (2011). *The non-preganglionic Edinger-Westphal nucleus: An integration center for energy balance and stress adaptation.* Radboud University, Nijmegen, the Netherlands.
69. Schellekens, A.F.A. (2011). *Gene-environment interaction and intermediate phenotypes in alcohol dependence.* Radboud University, Nijmegen, the Netherlands.
70. Van Marle, H.J.F. (2011). *The amygdala on alert: A neuroimaging investigation into amygdala function during acute stress and its aftermath.* Radboud University, Nijmegen, the Netherlands.
71. De Laat, K.F. (2011). *Motor performance in individuals with cerebral small vessel disease: An MRI study.* Radboud University Medical Centre, Nijmegen, the Netherlands.
72. Mädebach, A. (2011). *Lexical access in speaking: Studies on lexical selection and cascading activation.* Radboud University, Nijmegen, the Netherlands.
73. Poelmans, G.J.V. (2011). *Genes and protein networks for neurodevelopmental disorders.* Radboud University, Nijmegen, the Netherlands.
74. Van Norden, A.G.W. (2011). *Cognitive function in elderly individuals with cerebral small vessel disease. An MRI study.* Radboud University Medical Centre, Nijmegen, the Netherlands.
75. Jansen, E.J.R. (2011). *New insights into V-ATPase functioning: the role of its accessory subunit Ac45 and a novel brain-specific Ac45 paralog.* Radboud University, Nijmegen, the Netherlands.
76. Haaxma, C.A. (2011). *New perspectives on preclinical and early stage Parkinson's disease.* Radboud University Medical Centre, Nijmegen, the Netherlands.
77. Haegens, S. (2012). *On the functional role of oscillatory neuronal activity in the somatosensory system.* Radboud University, Nijmegen, the Netherlands.
78. van Barneveld, D.C.P.B.M. (2012). *Integration of exteroceptive and interoceptive cues in spatial localization.* Radboud University, Nijmegen, the Netherlands.
79. Spies, P.E. (2012). *The reflection of Alzheimer disease in CSF.* Radboud University Medical Centre, Nijmegen, the Netherlands.
80. Helle, M. (2012). *Artery-specific perfusion measurements in the cerebral vasculature by magnetic resonance imaging.* Radboud University, Nijmegen, the Netherlands.
81. Egetemeir, J. (2012). *Neural correlates of real-life joint action.* Radboud University, Nijmegen, the Netherlands.
82. Janssen, L. (2012). *Planning and execution of (bi)manual grasping.* Radboud University, Nijmegen, the Netherlands.
83. Vermeer, S. (2012). *Clinical and genetic characterisation of autosomal recessive cerebellar ataxias.* Radboud University Medical Centre, Nijmegen, the Netherlands.
84. Vrins, S. (2012). *Shaping object boundaries: Contextual effects in infants and adults.* Radboud University, Nijmegen, the Netherlands.
85. Weber, K.M. (2012). *The language learning brain: Evidence from second language and bilingual studies of syntactic processing.* Radboud University, Nijmegen, the Netherlands.
86. Verhagen, L. (2012). *How to grasp a ripe tomato.* Utrecht University, Utrecht, the Netherlands.
87. Nonkes, L.J.P. (2012). *Serotonin transporter gene variance causes individual differences in rat behaviour: For better and for worse.* Radboud University Medical Centre, Nijmegen, the Netherlands.
88. Joosten-Weyn Banningh, L.W.A. (2012). *Learning to live with Mild Cognitive Impairment: development and evaluation of a psychological intervention for patients with Mild Cognitive Impairment and their significant others.* Radboud University Medical Centre, Nijmegen, the Netherlands.
89. Xiang, HD. (2012). *The language networks of the brain.* Radboud University, Nijmegen, the Netherlands.

90. Snijders, A.H. (2012). *Tackling freezing of gait in Parkinson's disease.* Radboud University Medical Centre, Nijmegen, the Netherlands.

91. Rouwette, T.P.H. (2012). *Neuropathic pain and the brain - Differential involvement of corticotropin-releasing factor and urocortin 1 in acute and chronic pain processing.* Radboud University Medical Centre, Nijmegen, the Netherlands.

92. Van de Meerendonk, N. (2012). *States of indecision in the brain: Electrophysiological and hemodynamic reflections of monitoring in visual language perception.* Radboud University, Nijmegen, the Netherlands.

93. Sterrenburg, A. (2012). *The stress response of forebrain and midbrain regions: Neuropeptides, sex-specificity and epigenetics.* Radboud University, Nijmegen, The Netherlands.

94. Uithol, S. (2012). *Representing action and intention.* Radboud University, Nijmegen, The Netherlands.

95. Van Dam, W.O. (2012). *On the specificity and flexibility of embodied lexical-semantic representations.* Radboud University, Nijmegen, The Netherlands.

96. Slats, D. (2012). *CSF biomarkers of Alzheimer's disease: Serial sampling analysis and the study of circadian rhythmicity.* Radboud University Medical Centre, Nijmegen, the Netherlands.

97. Van Nuenen, B.F.L. (2012). *Cerebral reorganization in premotor parkinsonism.* Radboud University Medical Centre, Nijmegen, the Netherlands.

98. van Schouwenburg, M.R. (2012). *Frontostriatal mechanisms of attentional control.* Radboud University, Nijmegen, The Netherlands.

99. Azar, M.G. (2012). *On the theory of reinforcement learning: Methods, convergence analysis and sample complexity.* Radboud University, Nijmegen, The Netherlands.

100. Meeuwissen, E.B. (2012). *Cortical oscillatory activity during memory formation.* Radboud University, Nijmegen, The Netherlands.

101. Arnold, J.F. (2012). *When mood meets memory: Neural and behavioral perspectives on emotional memory in health and depression.* Radboud University, Nijmegen, The Netherlands.

102. Gons, R.A.R. (2012). *Vascular risk factors in cerebral small vessel disease: A diffusion tensor imaging study.* Radboud University Medical Centre, Nijmegen, the Netherlands.

103. Wingbermhle, E. (2012). *Cognition and emotion in adults with Noonan syndrome: A neuropsychological perspective.* Radboud University, Nijmegen, The Netherlands.

104. Walentowska, W. (2012). *Facing emotional faces. The nature of automaticity of facial emotion processing studied with ERPs.* Radboud University, Nijmegen, The Netherlands.

105. Hoogman, M. (2012). *Imaging the effects of ADHD risk genes.* Radboud University, Nijmegen, The Netherlands.

106. Tramper, J. J. (2012). *Feedforward and feedback mechanisms in sensory motor control.* Radboud University, Nijmegen, The Netherlands.

107. Van Eijndhoven, P. (2012). *State and trait characteristics of early course major depressive disorder.* Radboud University Medical Centre, Nijmegen, the Netherlands.

108. Visser, E. (2012). *Leaves and forests: Low level sound processing and methods for the large-scale analysis of white matter structure in autism.* Radboud University, Nijmegen, The Netherlands.

109. Van Tooren-Hoogenboom, N. (2012). *Neuronal communication in the synchronized brain. Investigating the functional role of visually-induced gamma band activity: Lessons from MEG.* Radboud University, Nijmegen, The Netherlands.

110. Henckens, M.J.A.G. (2012). *Imaging the stressed brain. Elucidating the time- and region-specific effects of stress hormones on brain function: A translational approach.* Radboud University, Nijmegen, The Netherlands.

111. Van Kesteren, M.T.R. (2012). *Schemas in the brain: Influences of prior knowledge on learn-*

ing, memory, and education. Radboud University, Nijmegen, The Netherlands.

112. Brenders, P. (2012). *Cross-language interactions in beginning second language learners.* Radboud University, Nijmegen, The Netherlands.

113. Ter Horst, A.C. (2012). *Modulating motor imagery. Contextual, spatial and kinaesthetic influences.* Radboud University, Nijmegen, The Netherlands.

114. Tesink, C.M.J.Y. (2013). *Neurobiological insights into language comprehension in autism: Context matters.* Radboud University, Nijmegen, The Netherlands.

115. Böckler, A. (2013). *Looking at the world together. How others' attentional relations to jointly attended scenes shape cognitive processing.* Radboud University, Nijmegen, The Netherlands.

116. Van Dongen, E.V. (2013). *Sleeping to Remember. On the neural and behavioral mechanisms of sleep-dependent memory consolidation.* Radboud University, Nijmegen, The Netherlands.

117. Volman, I. (2013). *The neural and endocrine regulation of emotional actions.* Radboud University, Nijmegen, The Netherlands.

118. Buchholz, V. (2013). *Oscillatory activity in tactile remapping.* Radboud University, Nijmegen, The Netherlands.

119. Van Deurzen, P.A.M. (2013). *Information processing and depressive symptoms in healthy adolescents.* Radboud University, Nijmegen, The Netherlands.

120. Whitmarsh, S. (2013). *Nonreactivity and metacognition in mindfulness.* Radboud University, Nijmegen, The Netherlands.

121. Vesper, C. (2013). *Acting together: Mechanisms of intentional coordination.* Radboud University, Nijmegen, The Netherlands.

122. Lagro, J. (2013). *Cardiovascular and cerebrovascular physiological measurements in clinical practice and prognostics in geriatric patients.* Radboud University Medical Centre, Nijmegen, the Netherlands.

123. Eskenazi, T.T. (2013). *You, us & them: From motor simulation to ascribed shared intentionality in social perception.* Radboud University, Nijmegen, The Netherlands.

124. Ondobaka, S. (2013). *On the conceptual and perceptual processing of own and others' behavior.* Radboud University, Nijmegen, The Netherlands.

125. Overvelde, J.A.A.M. (2013). *Which practice makes perfect? Experimental studies on the acquisition of movement sequences to identify the best learning condition in good and poor writers.* Radboud University, Nijmegen, The Netherlands.

126. Kalisvaart, J.P. (2013). *Visual ambiguity in perception and action.* Radboud University Medical Centre, Nijmegen, The Netherlands.

127. Kroes, M. (2013). *Altering memories for emotional experiences.* Radboud University, Nijmegen, The Netherlands.

128. Duijnhouwer, J. (2013). *Studies on the rotation problem in self-motion perception.* Radboud University, Nijmegen, The Netherlands.

129. Nijhuis, E.H.J (2013). *Macroscopic networks in the human brain: Mapping connectivity in healthy and damaged brains.* University of Twente, Enschede, The Netherlands.

130. Braakman, M. H. (2013). *Posttraumatic stress disorder with secondary psychotic features. A diagnostic validity study among refugees in the Netherlands.* Radboud University, Nijmegen, The Netherlands.

131. Zedlitz, A.M.E.E. (2013). *Brittle brain power. Post-stroke fatigue, explorations into assessment and treatment.* Radboud University, Nijmegen, The Netherlands.

132. Schoon, Y. (2013). *From a gait and falls clinic visit towards self-management of falls in frail elderly.* Radboud University Medical Centre, Nijmegen, The Netherlands.

133. Jansen, D. (2013). *The role of nutrition in Alzheimer's disease - A study in transgenic mouse models for Alzheimer's disease and vascular disorders.* Radboud University, Nijmegen, The Netherlands.

134. Kos, M. (2013). *On the waves of language - Electrophysiological reflections on semantic and syntactic processing.* Radboud University, Nijmegen, The Netherlands.
135. Severens, M. (2013). *Towards clinical BCI applications: Assistive technology and gait rehabilitation.* Radboud University, Nijmegen, Sint Maartenskliniek, Nijmegen, The Netherlands.
136. Bergmann, H. (2014). *Two is not always better than one: On the functional and neural (in)dependence of working memory and long-term memory.* Radboud University, Nijmegen, The Netherlands.
137. Wronka, E. (2013). *Searching for the biological basis of human mental abilitites. The relationship between attention and intelligence studied with P3.* Radboud University, Nijmegen, The Netherlands.
138. Lüttjohann, A.K. (2013). *The role of the cortico-thalamo-cortical system in absence epilepsy.* Radboud University, Nijmegen, The Netherlands.
139. Brazil, I.A. (2013). *Change doesn't come easy: Dynamics of adaptive behavior in psychopathy.* Radboud University, Nijmegen, The Netherlands.
140. Zerbi, V. (2013). *Impact of nutrition on brain structure and function. A magnetic resonance imaging approach in Alzheimer mouse models.* Radboud University, Nijmegen, The Netherlands.
141. Delnooz, C.C.S. (2014). *Unravelling primary focal dystonia. A treatment update and new pathophysiological insights.* Radboud University Medical Centre, Nijmegen, The Netherlands.
142. Bultena, S.S. (2013). *Bilingual processing of cognates and language switches in sentence context.* Radboud University, Nijmegen, The Netherlands.
143. Janssen, G. (2014). *Diagnostic assessment of psychiatric patients: A contextual perspective on executive functioning.* Radboud University, Nijmegen, The Netherlands.
144. Piai, V. Magalhães (2014). *Choosing our words: Lexical competition and the involvement of attention in spoken word production.* Radboud University, Nijmegen, The Netherlands.
145. Van Ede, F. (2014). *Preparing for perception. On the attentional modulation, perceptual relevance and physiology of oscillatory neural activity.* Radboud University, Nijmegen, The Netherlands.
146. Brandmeyer, A. (2014). *Auditory perceptual learning via decoded EEG neurofeedback: a novel paradigm.* Radboud University, Nijmegen, The Netherlands.
147. Radke, S. (2014). *Acting social: Neuroendocrine and clinical modulations of approach and decision behavior.* Radboud University, Nijmegen, The Netherlands.
148. Simanova, I. (2014). *In search of conceptual representations in the brain: towards mind-reading.* Radboud University, Nijmegen, The Netherlands.
149. Kok, P. (2014). *On the role of expectation in visual perception: A top-down view of early visual cortex.* Radboud University, Nijmegen, The Netherlands.
150. Van Geldorp, B. (2014). *The long and the short of memory: Neuropsychological studies on the interaction of working memory and long-term memory formation.* Radboud University, Nijmegen, The Netherlands.
151. Meyer, M. (2014). *The developing brain in action - Individual and joint action processing.* Radboud University, Nijmegen, The Netherlands.
152. Wester, A. (2014). *Assessment of everyday memory in patients with alcohol-related cognitive disorders using the Rivermead Behavioural Memory Test.* Radboud University, Nijmegen, The Netherlands.
153. Koenraadt, K. (2014). *Shedding light on cortical control of movement.* Radboud University, Nijmegen; Sint Maartenskliniek, Nijmegen, The Netherlands.
154. Rutten-Jacobs, L.C.A. (2014). *Long-term prognosis after stroke in young adults.* Radboud University Medical Centre, Nijmegen, The Netherlands.
155. Herbert, M.K. (2014). *Facing uncertain diagnosis: the use of CSF biomarkers for the*

differential diagnosis of neurodegenerative diseases. Radboud University Medical Centre, Nijmegen, The Netherlands.

156. Llera Arenas, A. (2014). *Adapting brain computer interfaces for non-stationary changes.* Radboud University, Nijmegen, The Netherlands.
157. Smulders, K. (2014). *Cognitive control of gait and balance in patients with chronic stroke and Parkinson's disease.* Radboud University Medical Centre, Nijmegen, The Netherlands.
158. Boyacioglu, R. (2014). *On the application of ultra-fast fMRI and high resolution multiband fMRI at high static field strengths.* Radboud University, Nijmegen, The Netherlands.
159. Kleinnijenhuis, M. (2014). *Imaging fibres in the brain.* Radboud University, Nijmegen, The Netherlands.
160. Geuze, J. (2014). *Brain Computer Interfaces for Communication: Moving beyond the visual speller.* Radboud University, Nijmegen, The Netherlands.
161. Platonov, A. (2014). *Mechanisms of binocular motion rivalry.* Radboud University, Nijmegen, The Netherlands.
162. Van der Schaaf, M.E. (2014). *Dopaminergic modulation of reward and punishment learning.* Radboud University Medical Centre, Nijmegen, The Netherlands.
163. Aerts, M.B. (2014). *Improving diagnostic accuracy in parkinsonism.* Radboud University Medical Centre, Nijmegen, The Netherlands.
164. Vlek, R. (2014). *From Beat to BCI: A musical paradigm for, and the ethical aspects of Brain-Computer Interfacing.* Radboud University, Nijmegen, The Netherlands.
165. Massoudi, R. (2014). *Interaction of task-related and acoustic signals in single neurons of monkey auditory cortex.* Radboud University, Nijmegen, The Netherlands
166. Stolk, A. (2014). *On the generation of shared symbols.* Radboud University, Nijmegen, The Netherlands.
167. Krause F. (2014). *Numbers and magnitude in the brain: A sensorimotor grounding of numerical cognition.* Radboud University, Nijmegen, The Netherlands.
168. Munneke, M.A.M. (2014). *Measuring and modulating the brain with non-invasive stimulation.* Radboud University Medical Centre, Nijmegen, The Netherlands.
169. Von Borries, K. (2014). *Carrots & Sticks - a neurobehavioral investigation of affective outcome processing in psychopathy.* Radboud University Medical Centre, Nijmegen, The Netherlands.
170. Meel-van den Abeelen, A.S.S. (2014). *In control. Methodological and clinical aspects of cerebral autoregulation and haemodynamics.* Radboud University Medical Centre, Nijmegen, The Netherlands.
171. Leoné, F.T.M. (2014). *Mapping sensorimotor space: Parieto-frontal contributions to goal-directed movements.* Radboud University, Nijmegen, The Netherlands.
172. Van Kessel, M. (2014). *Nothing left? How to keep on the right track - Spatial and non-spatial attention processes in neglect after stroke.* Radboud University, Nijmegen, The Netherlands.
173. Vulto-van Silfhout, A. T. (2014). *Detailed, standardized and systematic phenotyping for the interpretation of genetic variation.* Radboud University Medical Centre, Nijmegen, The Netherlands.
174. Arnoldussen, D. (2015). *Cortical topography of self-motion perception.* Radboud University, Nijmegen, The Netherlands.
175. Meyer, M.C. (2015). *Inbetween Modalities: Combined EEG - fMRI.* Radboud University, Nijmegen, The Netherlands.
176. Bralten, J. (2015). *Genetic factors and the brain in ADHD.* Radboud University Medical Center, Nijmegen, The Netherlands.
177. Spaak, E. (2015). *On the role of alpha oscillations in structuring neural information processing.* Radboud University, Nijmegen, The Netherlands.